Summer 2021

Towards Intelligent Structural Health Monitoring of Infrastructure Systems: An Interdisciplinary Study of Acoustic Emission Monitoring, Numerical Simulation, and Artificial Intelligence

Li Ai

Towards Intelligent Structural Health Monitoring of Infrastructure Systems: An Interdisciplinary Study of Acoustic Emission Monitoring, Numerical Simulation, and Artificial Intelligence

by

Li Ai

Bachelor of Engineering
Zhengzhou University, Zhengzhou, China, 2014

Master of Engineering
Stevens Institute of Technology, Hoboken, New Jersey, 2016

Submitted in Partial Fulfillment of the Requirements

For the Degree of Doctor of Philosophy in

Civil Engineering

College of Engineering and Computing

University of South Carolina

2021

Accepted by:

Paul Ziehl, Major Professor

Nathan Huynh, Committee Member

Sarah Gassman, Committee Member

Michel van Tooren, Committee Member

Benjamin Grisso, Committee Member

Tracey L. Weldon, Interim Vice Provost and Dean of the Graduate

Dedication

To my wife Ruixiao Sun, my father Chunhua Ai, my mother Ping Li.

献给我的妻子孙瑞霄，父亲艾春华，母亲李萍

To my dear motherland.

Acknowledgments

Perhaps many years from now, I will still remember the morning in 2014 when I first set foot in the United States and began my long journey of study. From 2014 to 2021, I spent seven years traveling from a city on the other side of the ocean in the heart of China to New Jersey, and then to South Carolina. I came here alone, and now I am surrounded by loved ones and friends. During the journey of my doctoral study, I imagined many times what it would be like when I finished my dissertation. Will I be so excited to share my happiness on WeChat Moments? Or would I be so tired and just want to have a good sleep? At this moment when the writing of the dissertation is nearing its end, South Carolina is experiencing its hottest summer. Looking outside of the window, the sunshine spread, the mood at this time is peace. As my many years of study are coming to an end, I would like to express my heartfelt thanks to the following persons and organizations:

My deepest gratitude is to my advisor, Dr. Paul Ziehl. He has created an extremely superior research environment for me and provided me with the best platform and resources so that I can devote myself to scientific research and academic exchanges. Researching and working with him has been one of my best working experiences. When I encountered problems and difficulties in my research, he was always able to discuss with me in time and helped me correctly grasp my research direction with his excellent knowledge. Also, I would like to thank the members of my dissertation committee, Dr.

Nathan Huynh, Dr. Sarah Gassman, Dr. Michel Van Tooren, and Dr. Benjamin Grisso. Their guidance and comments gave me great help in my research.

I am also grateful to all my colleagues in the research group at the University of South Carolina, especially Vafa Soltangharaei, Rafal Anay, and Lateef Assi. They gave me a lot of help with my research. I would also like to thank my friends at the University of South Carolina, (in no particular order) Feng Guo, Hetian Li, Huan Jiang, Hao Chen, Tingting Hu, Xiaoqun Yan, Xu Wu, Yuke Li, etc., and my friends Fanglong Chang, Tong Shi at Stevens Institute of Technology, Thanks to them for the happiness and joy they brought me in the past years.

I also want to pay tribute to Dr. Sophia Hassiotis and Dr. Marcus Rutner, my Master's advisors at Stevens Institute of Technology. They are the guides who first took me into scientific research. It is a pity that Dr. Sophia Hassiotis is no longer with us, but her rigorous and earnest spirit towards research will always guide me.

Thanks to the financial supports provided by the U.S Department of Energy-Nuclear Energy University Program (DE-NE0008544) and the Electric Power Research Institute (1-108781). The financial supports enabled me to complete my research with sufficient funds and participate in academic conferences. I benefited a lot from the communication with scholars and young students at the conferences.

My greatest thanks to my wife, my father, and my mother. Thank them for their love and support all the time. It was their love that accompanied me through the arduous journey of my doctoral study. Without them, I would have never been able to accomplish what I have.

Finally, I want to thank myself. Thanks for my perseverance when I am confused, thanks for the self-comfort when I am in the downturn. Thanks for walking through all the obstacles to the moment of writing this acknowledgment.

“行路难，行路难，多歧路，今安在。长风破浪会有时，直挂云帆济沧海。”

--An ancient Chinese poem to all Ph.D. candidates who have struggled and are struggling on the academic path.

Abstract

Some complex infrastructure systems, such as nuclear facilities and bridges, are subject to structural damage due to environmental erosion, material deterioration, and other factors after long periods of use. Stress corrosion cracking (SCC) and alkali-silica reaction (ASR) have been identified as the primary degradation mechanisms for steel and concrete structures in nuclear facilities and bridges. Ensuring the integrity and operational safety of structures during their lifetime is an important task. Nondestructive methods and structural health monitoring can be used to detect damage caused by SCC and ASR instead of conventional visual inspection. Among the nondestructive methods, acoustic emission (AE) is a suitable method because it is extremely sensitive to the initiation and propagation of the damage in materials. Detection and localization of damage in structures can be achieved by deploying a network of AE sensors. However, the complexity of real-world structures is a challenge for the application of AE. In some cases, the area available for sensor attachment is limited. It would be challenging to deploy sensor arrays. An approach using a single AE sensor may be beneficial for damage detection in complex infrastructure system.

The purpose of this dissertation is to investigate the intelligent damage detection and localization approach for infrastructure system such as spent nuclear fuel storage containers and concrete bridge components leveraging deep learning techniques and a single AE sensor. In addition, a novel transfer learning approach for damage localization without labelled historical signals for training is proposed. The finite element model is

developed to generate numerical AE signals for training the supervised learning model. Unsupervised domain adaptation technology is used to reduce the difference in distribution between the generated numerical AE signals and the realistic AE signals.

The results suggest that the intelligent approach using a single AE sensor and deep learning techniques has a good performance. The transfer learning approach is able to localize AE signals with high accuracy without using labelled training data, demonstrating that it could be a potential approach to localize ASR and SCC events on infrastructure systems. However, further research is needed to standardize the method for field application.

Table of Contents

List of Tables

List of Figures

Chapter 1

Introduction

1.1 Background

Ensuring the integrity and safety of infrastructural system throughout their service lives is an important task. Some complex infrastructural systems, such as nuclear facilities, bridges, and dams are subject to structural damage due to environmental erosion, material deterioration, fatigue damage, and other factors after long periods of use. For instance, nuclear power generation has been widely applied in the United States for decades. Currently, the cooling pools and dry cask storage systems (DCSS) have been used to store the spent fuel for over 20 years [1]. Spent fuels are placed in stainless-steel canisters, then water and air are removed and replaced by inert gas. After decades some of the older canisters are showing signs of degeneration. Stress corrosion cracking (SCC) has been identified as the primary degradation mechanism in the canisters due to the length of time they have been in use. The high salinity and humidity in the coastal region where those canisters are stored is another factor in their deterioration [2; 3]. Besides nuclear facilities, a large number of bridges in the United States have been in use over lengthy periods of time. In the United States, nearly 45,000 bridges are currently classified as structurally deficient [4]. This poses a significant threat to transportation safety. Alkali-silica reaction (ASR) is one of the main cracking sources in the concrete of bridges [5]. ASR is a chemical reaction between silica in reactive aggregate and alkaline ions in cement. The product of this reaction is a hygroscopic gel, which absorbs humidity and expands. The gel exerts pressure on the aggregate and cement matrix and causes cracking. The structural integrity of these infrastructures is a matter of national economics and a potential hazard to public safety. Therefore, inspecting the infrastructure and providing maintenance in a timely manner is crucial.

Many approaches have been utilized to inspect and monitor cracks in structures. Conventional approaches to inspection include regular visual inspections, coring, and petrographic analysis, demountable mechanical strain gauge (DEMEC gauge), relative humidity or moisture content measurement, and crack indexing. These approaches have several disadvantages. For example, visual inspection does not account for cracks below the surface of the structures. Moreover, visual inspection of large-scale structures is time-consuming and prone to human error [6]. Coring and petrographic analyses are destructive methods that are generally unsuitable for sensitive structures such as nuclear facilities. Furthermore, it is difficult to evaluate the condition of the entire structure with only a few cores or samples.

Utilizing nondestructive methods is a proposed solution. Several nondestructive methods such as radiographic inspection (RT), ultrasonic testing (UT), acoustic emission testing (AE), and thermal imaging/infrared testing (TIR) have been employed in the inspection and monitoring of infrastructural components [7-14]. AE is a method worth investigating among the non-destructive methods because of its extreme sensitivity to damage initiation and their propagation in materials [15-22]. Several researchers have explored AE for monitoring damage in infrastructural systems such as steel structures [23-26] and concrete structures [27-31]. Previous studies have proven that AE structural health monitoring is a reliable technique. However, traditional methods for analyzing AE signals are usually based on experience and can be very challenging, especially for complex structures. Therefore, intelligent algorithms are needed to assist in analyzing AE data.

1.2 Research significance

Steel and concrete are the essential construction materials of infrastructures. The infrastructural components are under threat of structural damage after long-term operation. SCC and ASR are the main damage causing mechanisms in steel and concrete structures. The monitoring and evaluation of SCC and ASR damages in structures are required to ensure the serviceability and integrity of infrastructures such as stainless-steel spent fuel storage canisters and concrete components in bridges. AE structural health monitoring could be used for monitoring SCC and ASR development. However, there are several challenges and scientific gaps in developing an AE monitoring approach for such use. Some of the gaps are addressed in this dissertation.

One of the gaps is the lack of investigation of the feasibility of AE monitoring for the detection of SCC damage in a large-scale stainless-steel spent fuel storage canister. This gap is addressed in Chapter 3. However, there is another problem when applying AE monitoring in spent fuel storage canisters. The canisters are huge and are stored in a concrete overpack. The area available for sensor attachment is limited. It is difficult to employ an AE sensor array around the cracking region to detect the location of a crack. Artificial intelligence techniques such as machine learning and deep learning are investigated in Chapter 4 as a method to solve the source localization problem.

In addition to the source localization of AE events, a gap exists in the damage evaluation of ASR in concrete components using AE. The selection of the appropriate AE features for analysis has generally been based on experience and is very challenging, especially for complex data sets. Therefore, an automatic approach is required to extract

features directly from raw AE data in order to find potential patterns in the complex data sets. This goal can be fulfilled by using deep learning methods explored in Chapter 5.

Chapters 3 through 5 show how promising machine learning and deep learning is in the analyzation of AE signals. However, another current challenge with this method is the difficulty of accessing the labeled AE signals in order to train the machine learning and deep learning model. In Chapter 6, a novel transfer learning approach for AE analysis, without labeled historical AE signals, is proposed to address the challenge.

1.3 Objectives

The primary object of this dissertation is to develop an intelligent acoustic emission (AE) monitoring approach for monitoring the structural health of infrastructures without historical AE signals to train the artificial intelligent models. Four different studies are included in this dissertation to accomplish the primary objective. Each study has its own specific set of objectives.

1.3.1 Structural Health Monitoring of Stainless-Steel Nuclear Fuel Storage Canister Using Acoustic Emission

The AE monitoring method may work as an early warning screening during the overall inspection of infrastructure systems. AE monitoring can alert us to the existence of cracks and provide the location of the cracks. Subsequent quantitative studies of the damage will be investigated by the inspection methods such as ultrasonic inspection. El Guerjouma et al. [32] utilized AE to provide information about the damage initiation and development in fiber reinforced polymer composites. Ultrasonic inspection was then employed to quantify the damage. Shiotani et al. [33] investigated the global monitoring of large concrete structures using AE and ultrasonic techniques. The evaluation of AE

activity leads to information about any specific part of the structure that requires attention. Consequently, more detailed ultrasonic examinations can be conducted once the target area is selected.

Understanding the capacity of AE monitoring and assessing the initiation and propagation of SCC in large-scale nuclear spent fuel storage canisters is one of the critical issues. In addition, selecting the appropriate type of AE sensor is also significant to crack monitoring. An experiment was conducted on a large-scale stainless-steel specimen made of similar length and thickness to what is typical of a nuclear spent fuel storage canister shell. The main objectives of this study are:

- Evaluate the efficacy of AE monitoring as a nondestructive method to provide structural monitoring and assessment of stress corrosion crack on a 304H stainless steel plate specimen of an identical scale to field-deployed nuclear-spent fuel storage canisters.
- Investigate the attenuation of AE signals along the length of the steel plate specimen and localize the AE source on the specimen.
- Develop finite element models to generate numerical AE signals for the purpose of AE sensor selection for the field application.

1.3.2 Source Localization on Large-Scale Canisters for Used Nuclear Fuel Storage Using Optimal Number of Acoustic Emission Sensors

Machine learning (a branch of Artificial Intelligence) has been applied in the field of acoustic emission monitoring, especially in cases where there are limitations in the number of sensors and sensor locations. By using machine learning algorithms, accurate source localization and damage identification can be conducted using only a single AE

sensor. This approach reduces the cost of the system and reduces cabling requirements. Machine learning techniques were employed to localize the simulated AE sources on the nuclear-spent fuel storage canister specimen. AE signals were collected by a single AE sensor attached to the bottom edge of the specimen. The primary objectives of this research are as follows:

- Study source localization approaches using artificial neural network (ANN), random forest (RF), and stacked autoencoders (SAE).
- Investigate the importance of the AE features utilized in machine learning techniques and study how these features affect the localization results.
- Evaluate and compare efficiency and accuracy in terms of localization approaches using ANN, RF, and SAE.

1.3.3 Evaluation of ASR in Concrete Using Acoustic Emission and Deep Learning

In addition to crack localization, assessing the damage stage and evaluating the health condition of infrastructure is another objective of using AE monitoring. In this study, the evaluation of ASR stages in concrete using AE and artificial intelligence technology is investigated. The primary objectives of this research are as follows:

- Divide the AE signals collected during the ASR process into different stages based on the cumulative signal strength and AE features.
- Evaluate the ASR stages of concrete by classifying the AE signals into the corresponding ASR stages using convolutional neural network (CNN) and stacked autoencoders (SAE).
- Compare the performance of ASR evaluation using CNN and SAE and discussing the efficiency in terms of computational time.

1.3.4 A Transfer Learning Approach for Acoustic Emission Localization Using Numerical Simulation and Unsupervised Domain Adaptation

The efficiency of applying artificial intelligent technologies in AE monitoring has been investigated and validated by three previous studies shown in this dissertation. However, one of the key problems in the field application is the lack of efficient historical AE signals for training. This study proposes a transfer learning framework to solve this problem by using unsupervised domain adaptation and the finite element model proposed in the first study. The primary objectives of this research are as follows:

- Generate experimental AE signals (target domain) in a steel specimen by conducting Hsu Nielsen excitation. Utilizing finite element models to generate numerical AE signals as the data in the source domain.
- Use geodesic flow kernel (GFK) to augment the data in the source domain
- Using unsupervised domain adaptation to align the data distribution in the target and source domain.
- Train a CNN model for AE source localization using the source domain after augmentation and unsupervised domain adaptation. Test the performance of the trained CNN model on the experimental AE signals in the target domain.

1.4 Layout of dissertation

Seven chapters are included in the dissertation. Chapter 2 is entitled “Literature review”. This chapter introduces background information from previously published literature and the methods utilized in the dissertation.

Chapters 3 through 6 were prepared in paper format, including published papers, submitted papers, and papers that are planned to be submitted. Therefore, some essential explanations may be repeated.

Chapter 3 is titled “Structural Health Monitor of Stainless-Steel Structures for Spent Nuclear Fuel Storage Using Acoustic Emission”, where the AE signals of corrosion cracking in the spent fuel storage canister specimen were collected and source localized. A finite element model was developed to generate numerical AE signals. The AE sensor with the correct operating frequency range can be selected for field application by studying the frequency component of numerical signals. The finite element model in this study is also used in Chapter 6.

Chapter 4 is titled “Source Localization on Large-Scale Canisters for Used Nuclear Fuel Storage Using Optimal Number of Acoustic Emission Sensors”. In this study, the AE signal localization of crack in the spent fuel storage canister using artificial intelligent technologies (ANN, RF, and SAE) was investigated.

Chapter 5 is titled “Evaluation of ASR in Concrete Using Acoustic Emission and Deep Learning”. In this study, AE was employed to monitor the ASR damage in concrete specimens. Two deep learning technologies: CNN and SAE were utilized to evaluate the ASR damage stages.

Chapter 6 is titled “A Transfer Learning Framework for Acoustic Emission Localization Using Numerical Simulation and Unsupervised Domain Adaptation”. In this study, the finite element model developed in chapter 3 was employed to generate numerical AE signals. Data augmentation and unsupervised domain adaptation were employed to expand the number of numerical signals and reduced the difference between

the numerical and the realistic signals. The processed numerical AE signals were utilized for training a transfer learning model for AE source localization.

Chapter 7 includes a dissertation summary, research conclusions, and recommendations for future research.

1.5 References

[1] J.W. Hill,2018. Acoustic Emission Detection In 304H Stainless Steel Due To Intergranular Stress Corrosion Cracking.

[2] H. Yeom, T. Dabney, N. Pocquette, K. Ross, F.E. Pfefferkorn, K. Sridharan,2020. Cold spray deposition of 304L stainless steel to mitigate chloride-induced stress corrosion cracking in canisters for used nuclear fuel storage, Journal of Nuclear Materials 152254.

[3] X. Wu,2020. On residual stress analysis and microstructural evolution for stainless steel type 304 spent nuclear fuel canisters weld joint: Numerical and experimental studies, Journal of Nuclear Materials 152131.

[4] ARTBA, National Bridge Inventory: South Carolina, Retrieved May 14, 2021, from https://artbabridgereport.org/state/profile/SC.

[5] V. Soltangharaei, R. Anay, N.W. Hayes, L. Assi, Y. Le Pape, Z.J. Ma, P. Ziehl,2018. Damage mechanism evaluation of large-scale concrete structures affected by alkali-silica reaction using acoustic emission, Applied Sciences 8 2148.

[6] F. Rajabipour, E. Giannini, C. Dunant, J.H. Ideker, M.D. Thomas,2015. Alkali–silica reaction: current understanding of the reaction mechanisms and the knowledge gaps, Cement and Concrete Research 76 130-146.

[7] R.R. Da Silva, M.H. Siqueira, L.P. Calôba, I.C. Da Silva, A. De Carvalho, J. Rebello,2002. Contribution To The Development Of A Radiographic Inspection Automated System, Journal of Nondestructive Testing 7 1-8.

[8] A.A.d. Carvalho, R.C.d.S.B. Suita, R.R.d. Silva, J.M.A. Rebello,2003. Evaluation of the relevant features of welding defects in radiographic inspection, Materials Research 6 427-432.

[9] H. Li, J. Li, X. Yun, X. Liu, A.S.-L. Fok,2011. Non-destructive examination of interfacial debonding using acoustic emission, Dental Materials 27 964-971.

[10] L. Pazdera, L. Topolar,2014. Application acoustic emission method during concrete frost resistance, Russian Journal of Nondestructive Testing 50 127-131.

[11] S. Gholizadeh,2016. A review of non-destructive testing methods of composite materials, Procedia Structural Integrity 1 50-57.

[12] S.K. Dwivedi, M. Vishwakarma, A. Soni,2018. Advances and researches on non destructive testing: A review, Materials Today: Proceedings 5 3690-3698.

[13] S. Zhang, W. Shen, D. Li, X. Zhang, B. Chen,2018. Nondestructive ultrasonic testing in rod structure with a novel numerical Laplace based wavelet finite element method, Latin American Journal of Solids and Structures 15.

[14] A. Hussain, H. Pu, D.-W. Sun,2018. Innovative nondestructive imaging techniques for ripening and maturity of fruits–a review of recent applications, Trends in Food Science & Technology 72 144-152.

[15] D. Li, K.S.C. Kuang, C.G. Koh,2017. Fatigue crack sizing in rail steel using crack closure-induced acoustic emission waves, Measurement Science and Technology 28 065601.

[16] R. Anay, V. Soltangharaei, L. Assi, T. DeVol, P. Ziehl,2018. Identification of damage mechanisms in cement paste based on acoustic emission, Construction and Building Materials 164 286-296.

[17] L. Assi, V. Soltangharaei, R. Anay, P. Ziehl, F. Matta,2018. Unsupervised and supervised pattern recognition of acoustic emission signals during early hydration of Portland cement paste, Cement and Concrete Research 103 216-225.

[18] V. Soltangharaei, R. Anay, L. Ai, E.R. Giannini, J. Zhu, P. Ziehl,2020. Temporal Evaluation of ASR Cracking in Concrete Specimens Using Acoustic Emission, Journal of Materials in Civil Engineering 32 04020285.

[19] R. Anay, A. Lane, D.V. Jáuregui, B.D. Weldon, V. Soltangharaei, P. Ziehl,2020. On-Site Acoustic-Emission Monitoring for a Prestressed Concrete BT-54 AASHTO Girder Bridge, Journal of Performance of Constructed Facilities 34 04020034.

[20] L. Ai, V. Soltangharaei, P. Ziehl,2021. Evaluation of ASR in Concrete Using Acoustic Emission and Deep Learning, Nuclear Engineering and Design.

[21] E.D. Dzaye, G. De Schutter, D.G. Aggelis,2020. Monitoring early-age acoustic emission of cement paste and fly ash paste, Cement and Concrete Research 129 105964.

[22] D. Li, K.S.C. Kuang, C.G. Koh,2018. Rail crack monitoring based on Tsallis synchrosqueezed wavelet entropy of acoustic emission signals: A field study, Structural Health Monitoring 17 1410-1424.

[23] J. Yu, P. Ziehl, B. Zárate, J. Caicedo,2011. Prediction of fatigue crack growth in steel bridge components using acoustic emission, Journal of Constructional Steel Research 67 1254-1260.

[24] M. Hossain, J. Yu, P. Ziehl, J. Caicedo, F. Matta, S. Guo, M. Sutton, Acoustic emission source mechanisms for steel bridge material, American Institute of Physics, 2013, 1378-1384.

[25] M.G. Droubi, N.H. Faisal, F. Orr, J.A. Steel, M. El-Shaib,2017. Acoustic emission method for defect detection and identification in carbon steel welded joints, Journal of constructional steel research 134 28-37.

[26] S. Cao, C. Chen, Q. Liu, Damage Factor Analysis of Q235A Steel Based on Acoustic Emission Test, IOP Publishing, 2020, 012124.

[27] M. Abdelrahman, M.K. ElBatanouny, P. Ziehl, J. Fasl, C.J. Larosche, J. Fraczek,2015. Classification of alkali–silica reaction damage using acoustic emission: A proof-of-concept study, Construction and Building Materials 95 406-413.

[28] Y. Farnam, M.R. Geiker, D. Bentz, J. Weiss,2015. Acoustic emission waveform characterization of crack origin and mode in fractured and ASR damaged concrete, Cement and Concrete Composites 60 135-145.

[29] T. Lokajíček, R. Přikryl, Š. Šachlová, A. Kuchařová,2017. Acoustic emission monitoring of crack formation during alkali silica reactivity accelerated mortar bar test, Engineering Geology 220 175-182.

[30] F. Weise, K. Voland, S. Pirskawetz, D. Meinel, Innovative measurement techniques for characterising internal damage processes in concrete due to ASR, 2012, 20-25.

[31] L. Ai, V. Soltangharaei, M. Bayat, B. Greer, P. Ziehl,2021. Source localization on large-scale canisters for used nuclear fuel storage using optimal number of acoustic emission sensors, Nuclear Engineering and Design 375 111097.

[32] R. El Guerjouma, J.-C. Baboux, D. Ducret, N. Godin, P. Guy, S. Huguet, Y. Jayet, T. Monnier,2001. Non-destructive evaluation of damage and failure of fibre reinforced polymer composites using ultrasonic waves and acoustic emission, Advanced engineering materials 3 601–608.

[33] T. Shiotani, D.G. Aggelis, O. Makishima,2009. Global monitoring of large concrete structures using acoustic emission and ultrasonic techniques: case study, Journal of Bridge Engineering 14 188-192.

Chapter 2

Literature Review

2.1 Introduction

Acoustic emission (AE) is a physical phenomenon, which is related to the stress wave generated by the rapid release of elastic energy that occurs when cracks or damages form in materials [1]. AE signals can be detected and collected by deploying AE sensors on the surface of an object. The method of recording and processing AE signals to monitor and diagnose the health status of an object is referred to as AE monitoring. This method is nondestructive, sensitive, and has continuous monitoring capabilities [2-7]. It has been widely used to monitor and detect damage in steel structures such as stress corrosion cracking (SCC) [8-11]. Li et al. [8] used AE to monitor the SCC of the steel wires used in bridge cables. The authors developed a particle swarm optimization cluster method to classify AE signals into different clusters in order to identify their relationship with SCC mechanisms. The results pointed out that the AE sources of SCC in bridge cables can be classified into four types: passive film breakdown, detachment of the corrosion product, crack initiation, and crack extension. Li et al. [9] investigated the SCC in prestressed strands using AE. The ant colony optimization algorithm was utilized to do the unsupervised pattern recognition of AE signals. Four clusters of AE signals were identified as being related to the four failure stages of SCC. The clustering was employed as the labels of a self-organizing feature mapping neural network. The results indicated that the AE characteristic parameter distribution of different SCC failure stages can be realized. Zhang et al. [10] studied the AE monitoring of 304 stainless steel in high-temperature water. A random forest model was used to separate the AE signals of different SCC modes. They extracted several AE features as the input of random forest and observed that the rise time is the most useful feature to distinguish the AE signals.

Recently, AE has been applied to the detection of SCC on DCSS canisters. Soltangharaei et al. [11] investigated the AE monitoring of SCC on a small-scale 304 stainless steel plate instead of testing on the real-scale DCSS canister. The b-value and linear regression methods were employed for damage identification using AE data. The authors indicated the global b-values and the R^2-values calculated by conducting linear regression could identify the difference of SCC damage in the steel plate.

AE can also be utilized for the temporal evaluation of Alkali-silica reaction (ASR) damage in concrete structures used in bridges and nuclear facilities [12-17]. Farnam et al. [13] utilized peak frequency and frequency centroid to characterize signal signatures that emanate from cracks in aggregates and cement paste. High-frequency signals were observed in the earlier stage of ASR, while the low-frequency signals appeared later in the ASR process. X-ray images helped the authors to verify their hypothesis. Lokajíček et al. [14] utilized ultrasonic pulse velocity and AE to monitor the damage caused by ASR. Four specimens with different aggregate reactivities were used. The selection of the appropriate features was generally based on experience and were very challenging, especially for complex data sets. Therefore, an automatic approach became necessary to extract features directly from raw data and find potential patterns in the complex data sets. This goal can be fulfilled by using deep learning methods.

Results from previous studies indicated that AE monitoring has a good capability for the detection and identification of cracks in steel and concrete specimens. However, there is a problem when applying AE monitoring in realistic complex infrastructures. In some cases, the area available for sensor attachment is limited, it would be challenging to deploy sensor arrays to localize the damages. An intelligent and automatic localization

approach using only a single AE sensor can be beneficial in the detection and localization of damages in complex metallic infrastructures.

Adopting artificial intelligence techniques such as machine learning and deep learning algorithm is a potential approach. Machine learning is a supervised intelligent data processing technique [18]. By learning the features extracted from the data, machine learning can understand the data pattern and make a decision [19]. Machine learning models such as artificial neural network, support vector machine (SVM), K-nearest neighbor (KNN), and random forest has been widely utilized for signal processing [6; 20-24]. Deep learning methods are improved intelligent techniques which are based on machine learning. It can automatically learn features from complex data sets without feature extractions [25]. In recent years, machine learning and deep learning have been applied to AE localization using a single AE sensor [26; 27]. Ebrahimkhanlou et al. [26] proposed a deep learning framework based on a stacked autoencoder network to locate AE events on the metallic structures. Ai et al. [27] developed a passive health monitoring system to locate impacts on an aircraft component using one AE sensor, random forest, and stacked autoencoder network.

Previous studies have proven that using deep learning to analyze AE signals is promising. However, a current challenge associated with the use of the supervised learning algorithms on AE source localization is difficulty in accessing the labeled AE signals for existing structures. Transfer learning (TL) is a strategy which assists the supervised learning task when the available training data is limited [28]. TL has been utilized in the application of acoustic emission [3; 29]. However, those studies focused on the scenarios when the training AE signals are limited but still available. No research has

been conducted by using deep learning algorithms to analyze the AE signals with no labeled training AE signals available.

This dissertation aims to propose the damage detection and localization approach for infrastructure components like nuclear spent fuel storage canisters and concrete bridge components leveraging artificial intelligence techniques and AE monitoring. Furthermore, this dissertation investigates a novel TL approach for AE localization without labeled historical AE signals. A finite element model is developed to generate numerical AE signals for the training of artificial intelligence algorithms. Unsupervised domain adaptation technology is utilized to decrease the difference between the generated numerical AE signals with realistic AE signals. The methods utilized in this dissertation are introduced in the following sections.

2.2 AE signal processing methods

In the dissertation, signal processing methods, such as fast Fourier transform, continuous wavelets transform, and energy-frequency analysis have been employed to process and study the AE signals.

2.2.1 Fast Fourier transform (FFT)

Fourier transform is a common method for transferring a signal from time domain to frequency domain. The discrete version of Fourier transform is utilized for digital waveforms, which is referred to as Discrete Fourier Transform (DFT), and is presented in the following Eq. (2.1):

$$X_k = \sum_{n=0}^{N-1} X_n e^{-\frac{j2\pi kn}{N}} \tag{2.1}$$

Where, N is the number of samples. X_n is a signal in a time domain, and X_k is Fourier transform coefficients for K^{th} frequency.

2.2.2 Continuous wavelets transform (CWT)

CWT is a joint time-frequency analysis method that captures the time-frequency characteristics in non-stationary signals such as AE signals [30]. CWT has a good performance in signal processing in terms of both time and frequency [4]. The continuous wavelet coefficients can be expressed by a scalogram image. The 2D scalogram images are the input for CNN models. In this dissertation, the Morse wavelet is selected as the mother wavelet function to conduct CWT. The Fourier transform of Morse wavelet is presented in Eq (2.2):

$$\Psi_{p,\gamma}(x) = U(x)\alpha_{p,\gamma}x^{\frac{p^2}{\gamma}}e^{-x^{\gamma}} \tag{2.2}$$

where $U(x)$ refers to the unit step, $\alpha_{p,\gamma}$ refers to the normalizing constant, p^2 refers to the time-bandwidth product. γ is the parameter that characterizes the symmetry of the Morse wavelet [31].

2.2.3 Energy-frequency analysis

The energy-frequency features can be obtained by conducting an energy-frequency analysis. The energy-frequency features refer to the energies in the frequency bands of the signals. The AE time domain waveforms were converted to the frequency domain spectrum by conducting a fast Fourier transform (FFT). The frequency range of the AE signals can be divided into several bands with a width of a certain frequency. The area under the FFT spectrum in each frequency band is the energy enclosed by that frequency band [5]. Therefore, energy-frequency features could be derived from each AE signal.

2.3 AI technologies for AE source localization and ASR evaluation

2.3.1 Artificial neural network (ANN)

An artificial neural network was utilized for source localization of AE events in research topic 2. Artificial neural networks (ANNs) are information processing systems that mimic how the human brain processes information [24; 32]. The neural network adopted in this section is the back-propagation (BP) network, which consists of an input layer, hidden layers, and an output layer. Each layer has many processing elements, called neurons, and all neurons are connected to one another. The number of neurons in the input layer and the output layer corresponds to the number of variables and outputs. Figure 2.1 shows a simple three-layer artificial neural network consisting of layer j, i, and k. The number of neurons is m for layer j, n for layer i and l for layer k. $W_{(ij)}$ and $W_{(kj)}$ are weights between layers. The values of m and l are related to the problem for solving, and n is determined by the network designer.

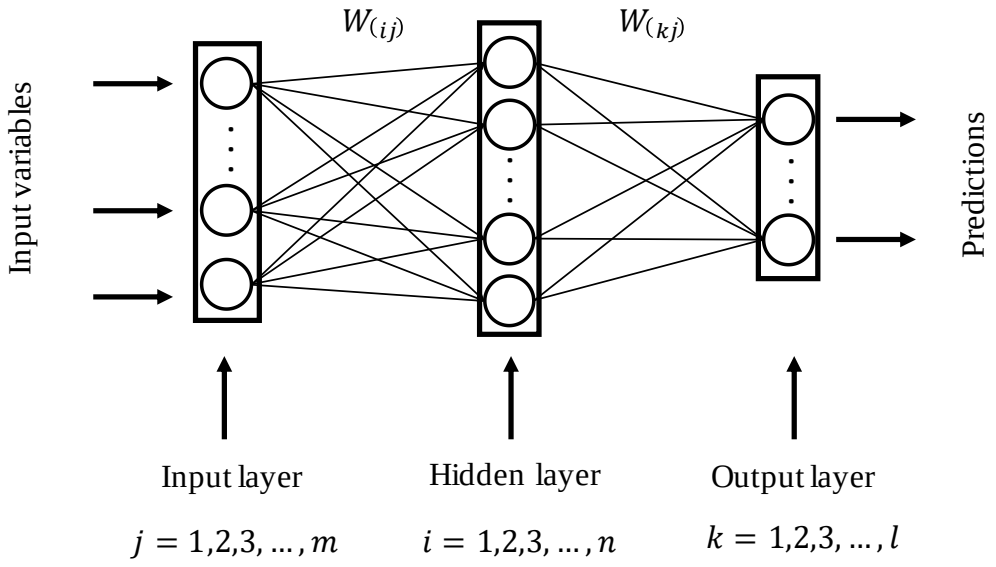

Figure 2.1 Three-layer artificial neural network

2.3.2 Random forest (RF)

Random forest was utilized for source localization of AE events in research topic 2. Random forest is an ensemble learning algorithm, which is a type of bagging algorithm [23; 33]. By combining multiple weak learning models (decision trees), the results of the weak learning models are voted or averaged to obtain the overall model results.

The decision tree makes classification decisions based on multiple features. At each node of the tree, the leaf node of the next layer is branched through a criterion according to the performance of the features. With layer-by-layer branching the sample categories included in the leaf nodes will gradually become consistent and the terminal leaf node is the classification result of the decision trees. In this paper, the Gini impurity of the node is used as the branching criterion when generating the decision tree. The Gini impurity of a node refers to the probability that a sample randomly selected from a node is misclassified when the sample is classified according to the distribution of the samples in the node. Therefore, the purity of the samples is negatively correlated with the Gini impurity.

Assuming that the sample set N contains K categories, then the Gini impurity of node t is obtained by Eq. (2.3):

$$Gini(S) = 1 - \sum_{i=1}^{K} P(^{i}/_{t}) \tag{2.3}$$

where $P(^{i}/_{t})$ is the probability of category i at node t. When $Gini(S) = 0$, or less than a predetermined threshold, it means that the samples belong to the same category. Otherwise, the sample is divided into two parts $N1$ and $N2$, according to feature F, and is then allocated to the two sub-nodes. As shown in Eq. (2.4):

$$Gini(N, F) = \frac{N1}{N} Gini(N1) + \frac{N2}{N} Gini(N2) \tag{2.4}$$

According to this layer-by-layer branching, until the number of samples in the node is less than the predetermined threshold, or the Gini impurity of the sample set is less than the predetermined threshold, or there are no more features, the system stops growing and forms a decision tree to accomplish classification and prediction.

Bagging is a parallel ensemble learning method [34]. A fixed number of samples are collected from the training set with replacements based on the bootstrapping method. Thereby, a sample set for each basic learning model is formed. Some samples may be repeated because of the replacement sampling, while some samples may not be drawn. The final result is voted or averaged from the result of all the basic models. The random forest algorithm is a combination of a decision tree and bagging. The decision tree is utilized as the basic learning model. Bagging improves the generalization error by reducing the variance of the basic learning model. The performance of bagging depends on the stability of the basic model. When the basic model is unstable, bagging helps to reduce the error caused by the random fluctuation of the training set. If the basic model is stable, bagging does not improve the model's performance and may even reduce the model's performance. The decision tree plus the bagging effectively decreases the variance of a single decision tree, thereby obtaining a complete random forest.

The random forest model can calculate and evaluate the importance of features through the feature division process while predicting or classifying. The calculation requires the help of the Gini impurity when the leaf node is branching; the method is shown as Eq. (2.5) and Eq. (2.6).

$$I_t(F) = Gini(N) - Gini(N, F) \tag{2.5}$$

$$S(F) = \sum_t I_t(F) \tag{2.6}$$

Where, $I_t(F)$ refers to the decrease of the Gini impurity before and after node t is split into two sub-nodes according to feature F. The absolute importance of feature $S(F)$ can be defined as the sum of $I_t(F)$ at all nodes split by feature F. The importance score of each feature can be obtained by normalizing the absolute importance of all features.

2.3.3 Stacked autoencoder (SAE)

Stacked autoencoders were utilized for source localization of AE events in research topic 2. An autoencoder is a three-layer neural network model with an input layer, a hidden layer, and an output layer [35]. The network structure is shown in Figure 2.2. The input and output layers have the same dimensions, while the hidden layer has a smaller dimension.

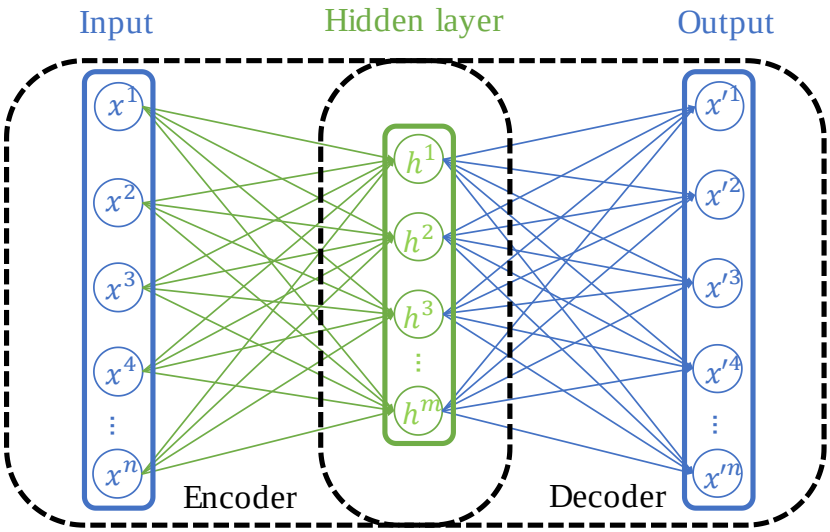

Figure 2.2. Autoencoder

Assuming the input data is an n dimensional vector $\{x^1, x^2, x^3 \ldots x^n\}$, the process of mapping the input data to the m ($m < n$) dimensional vector $\{h^1, h^2, h^3 \ldots h^m\}$ in the hidden layer through the nonlinear encoding function E is named as the encoder stage. The process of mapping the m dimension vector in the hidden layer to the n dimension

vector $\{x'^1, x'^2, x'^3 \ldots x'^n\}$ in the output layer through the decoding function D is referred to as the decoder stage. The encoding function E and the decoding function D are presented in Eq. (2.7) and Eq. (2.8).

$$h = E(x) = S_\theta(wx + b) \tag{2.7}$$

$$x' = D(h) = S_{\theta'}(\mathrm{w}'h + b') \tag{2.8}$$

Where, $\{\theta,\ \theta'\} = \{w,\ \mathrm{w}',\ b,\ b'\}$ is the mapping parameter set in the autoencoder. w and w' are the weights of encoding and decoding stages. Both are $m \times n$ dimensional matrix. b and b' are the n dimensional bias vectors of encoding and decoding stages. S is the activation function. The activation function for the autoencoder in this paper is a sigmoid function (Eq. (2.9)).

$$f(x) = \frac{1}{1+e^{-x}} \tag{2.9}$$

The process of transferring the input vector $\{x^1, x^2, x^3 \ldots x^n\}$ to the output vector $\{x'^1, x'^2, x'^3 \ldots x'^n\}$ is called reconstruction. The training object of the autoencoder is to minimize the error in data reconstruction by constantly adjusting the mapping parameters set $\{\theta,\ \theta'\} = \{w,\ \mathrm{w}',\ b,\ b'\}$. A training process of N iterations can be expressed By Eq. (2.10).

$$\theta,\ \theta' = \operatorname{argmin} \frac{1}{N}\sum_{i=1}^{N} L\left(x^i, x'^i\right) = \operatorname{argmin} \frac{1}{N}\sum_{i=1}^{N} \left\|x^i - x'^i\right\|^2 \tag{2.10}$$

Where, x^i and x'^i refer to the ith element in the input and output vector. L is the mean squared error between x^i and x'^i.

By minimizing reconstruction errors, the vector in the hidden layer preserves the information contained in the input vector. In the meantime, the dimension is significantly reduced [24]. Therefore, the vector $\{h^1, h^2, h^3 \ldots h^m\}$ in the hidden layer can be seen as the feature set extracted from the input vector.

The classification stacked autoencoder consists of multiple autoencoders and a softmax layer. The first autoencoder extracts the feature set of the input data and takes the obtained feature set as the input data of the next autoencoder for further feature extraction. All the training processes in autoencoders are unsupervised training, no labels are needed in this stage. The feature set from the last autoencoder is used as the input of the softmax classifier for supervised training. The corresponding classes of input data are required to be known by their labels. Assume the inputs contain k classes. The final output of a stacked autoencoder is a k dimensional vector, where each element represents the probability that the input belongs to this class. The class with the highest probability can be considered as the classification result.

2.3.4 Convolutional neural network (CNN)

CNN is a class of commonly used deep neural networks that are applied for image processing [36]. CNN is composed of three main parts: the input layer, the feature extraction layers, and the fully connected (FC) layer. The input layer is used to input the test and training data. Feature extraction layers are the core of the convolutional neural network, mainly including convolutional layers and pooling layers, which cooperate to derive the features from images and learn potential patterns in the data set. The architecture of a typical CNN with two convolutional layers and two pooling layers is shown in Figure 2.3.

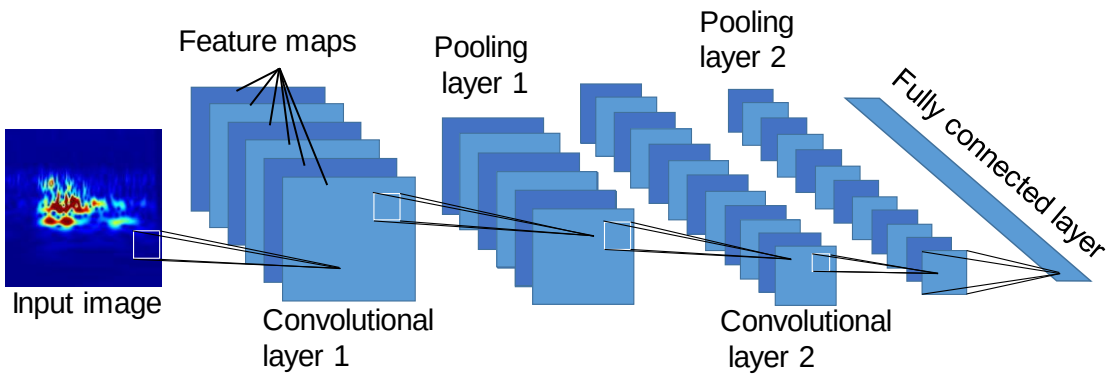

Figure 2.3 Architecture of a typical CNN

The convolutional layers are utilized to extract the features from images [37]. In the convolutional layer, multiple convolutional kernels are employed to filter the input and generate feature maps [37]. Generally, the output of the j^{th} feature maps of the n^{th} convolutional layer can be obtained by Eq. (2.11):

$$x_j^n = f\left(\sum_{i=1}^{M} x_i^{n-1} * k_{ij}^n + b_j^n\right) \tag{2.11}$$

where $f(\cdot)$ refers to the activation function, $*$ refers to the operation of convolutional kernels, k_{ij}^n is the kernel of the n^{th} filter, b_j^n is the corresponding bias matrix, x_i^{n-1} refers to the input feature map transferred from the $(n\text{-}1)^{th}$ convolutional layer.

The pooling layer is used to down-sampling feature maps obtained from the previous convolutional layer [38]. If the image feature maps are directly utilized for the classification without any processing, a great computational complexity will be generated, and the model will be prone to overfitting. Therefore, a further reduction in the dimensionality of feature maps is required, which is the reason for the pooling layer after each convolutional layer. The input feature image is divided into mutually exclusive regions, and the feature information of adjacent image regions is aggregated for analysis.

This type of down-sampling method is called pooling [39]. Pooling can be divided into maximum pooling and mean pooling according to different operation modes. The general expression of the pooling layer is provided by Eq. (2.12):

$$x_j^n = f\left(\beta_j^n s_{down}(x_j^{n-1}) + b_j^n\right) \tag{2.12}$$

where $f(\cdot)$ refers to the activation function, β_j^n and b_j^n refers to the multiplicative bias and the additive bias, S_{down} refers to the down-sampling function, x_j^{n-1} refers to the input feature maps, x_j^n refers to the output feature map after down-sampling.

2.4 Finite element modeling (FEM)

Physical problems are usually described by partial differential equations (PDE). For most of the problems in realistic scenarios, it may be challenging to find analytic solutions to these partial differential equations. However, approximate equations can be constructed according to different methods of discretization, and numerical model equations can be obtained, which are similar to these partial differential equations [40]. These model equations can be solved numerically. Thus, the solutions of these numerical model equations are approximate solutions of the natural solutions of the corresponding partial differential equations. The finite element method (FEM) is used to calculate these approximate solutions [40].

The numerical AE waveform can be obtained by solving the dynamic equation of motion through FEM [27]. The dynamic equation of motion is shown in Eq. (2.13):

$$[M]\{\ddot{V}\} + [C]\{\dot{V}\} + [K]\{V\} = \{P(t)\} \tag{2.13}$$

Where, $[M]$ is the mass matrix, $[C]$ is the damping matrix, $[K]$ is the stiffness matrix, $\{V\}$ is the displacement victor, $\{\dot{V}\}$ is the velocity victor, $\{\ddot{V}\}$ is the acceleration victor, $\{P(t)\}$ is the applied load vector.

2.5 Transfer learning and unsupervised domain adaptation

The basic principles of transfer learning (TL) and unsupervised domain adaptation are introduced in this section. Generally, a sufficient number of training data and the corresponding labels are required by a supervised learning model such as artificial neural network, and decision tree. However, in some cases, enough training data with labels are difficult to obtain. TL is a strategy to solve this problem. Assuming there are two datasets. The first dataset $\{X_s, Y_s\} = \{(x_{s1}, x_{s2}, \dots, x_{sm}), (y_{s1}, y_{s2}, \dots, y_{sm})\}$. Where$(\mathrm{y_{s1}}, \mathrm{y_{s2}}, \dots, \mathrm{y_{sm}})$ is the label of $(x_{s1}, x_{s2}, \dots, x_{sm})$, and it is known. The second dataset $\{X_t, Y_t\} = \{(x_{t1}, x_{t2}, \dots, x_{tn}), (y_{t1}, y_{t2}, \dots, y_{tn})\}$, while the labels $(y_{t1}, y_{t2}, \dots, y_{tn})$are unknown for this dataset. The concept of transfer learning is to execute the classification of $\{X_t, Y_t\}$ based on the acquired knowledge from the model with training on $\{X_s, Y_s\}$. The dataset $\{X_s, Y_s\}$ is named source domain (D_S) and the dataset $\{X_t, Y_t\}$ to be classified is called target domain (D_T). One of the issues of TL is, the performance of TL based on D_S and D_T is not good when the difference between the source domain and the target domain is significant. Unsupervised domain adaptation is a technique for learning the domain invariant features from the annotated source domain and the unannotated target domain and reducing the distribution difference [41].

2.5.1 Manifold embedded distribution alignment (MEDA)

As mentioned above, $D_S: \{X_s, Y_s\}$, and $D_T: \{X_t, Y_t\}$ has different data destruction which means they have different marginal probabilities $(P_s(x_s) \neq P_t(x_t))$. and different conditional probability $(Q_s(x_s|y_s) \neq Q_t(x_t|y_t))$. Manifold embedded distribution alignment (MEDA) is an unsupervised domain adaptation algorithm to reduce the distribution difference by utilizing manifold feature learning and dynamic distribution

alignment [42]. Manifold feature learning is utilized to reduce the data drift between the source domain and target domain. Dynamic distribution alignment is employed to alignment the marginal and conditional distribution. The MEDA aims to articulate a cross-domain classifier f to predict the unknown Y_t .

2.5.2 Manifold feature learning

Manifold feature learning is an unsupervised domain adaptation method [43]. Manifold refers to the space with local Euclidean spatial properties, including curves and surfaces of various dimensions. One characteristic of manifold space is that features in the manifold space usually have good geometric structures. The manifold learning leverage this characterize to avoid feature distortions by mapping high-dimensional data into a low-dimensional manifold space. In MEDA, the geodesic flow kernel (GFK) is employed to conduct the manifold feature transformation. More details about GFK can be found in [44]. The process of manifold feature learning in MEDA is presented in Figure 2.4.

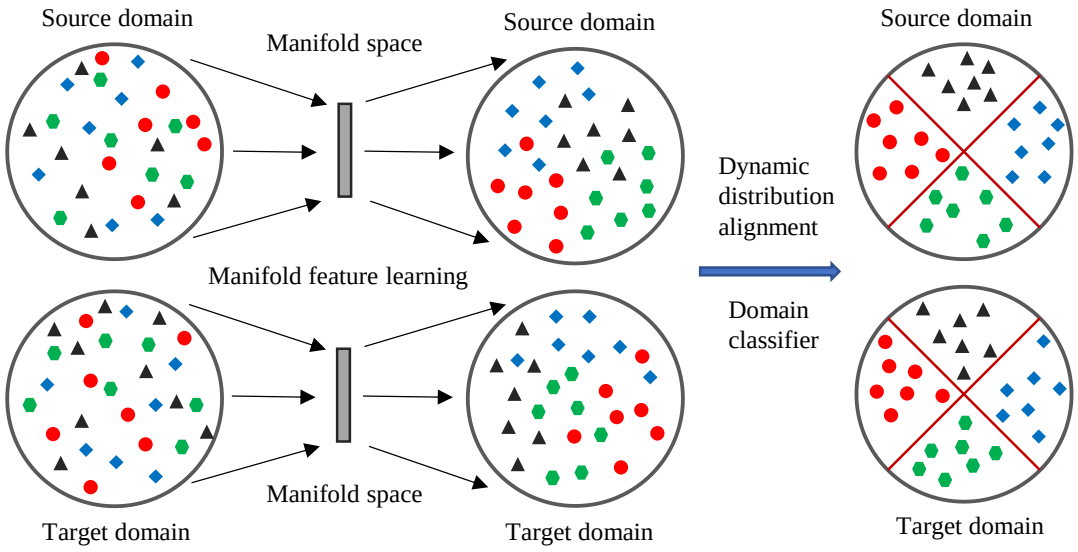

Figure 2.4 Procedures of MEDA

2.5.3 Dynamic distribution alignment

The importance of marginal distributions (P) and conditional distributions (Q) of the source domain and target domain tend to vary with the similarity of the two domains. For instance, marginal distribution is more significant when there are large differences between the source domain and target domain, while conditional distribution is more dominant when the two domains have high similarities. Therefore, the importance of P and Q needs to be quantitatively measured rather than simply counting them with the same weights. To accomplish this goal, the dynamic distribution alignment process is proposed in MEDA to dynamically evaluate the importance of these two distributions. The process of dynamic distribution alignment could be presented by Eq. (2.14):

$$\overline{D_f}(D_S, D_t) = (1-\omega)D_f(P_s, P_t) + \omega \sum_{t=1}^{T} D_f^{(t)}(Q_s, Q_t) \quad (2.14)$$

Where, $t \in \{1,2,3,\dots,T\}$ represents the classes of data, $\overline{D_f}(D_S, D_t)$ is the distribution after alignment. $D_f(P_s, P_t)$ refers to the marginal distribution alignment. $D_f^{(t)}(Q_s, Q_t)$ is the conditional distribution alignment for class t.

After the manifold feature learning and dynamic distribution alignment are completed. A domain classifier can be derived by Eq. (2.15). The procedure of dynamic distribution alignment and classification is illustrated in Figure 6.1.

$$f = \arg\min \sum_{i=1}^{t} (y_i - f(Z_i))^2 + \alpha \|f\|_K^2 + \beta \overline{D_f}(D_S, D_t) + \gamma R_f(D_S, D_t) \quad (2.15)$$

Where, $R_f(\cdot)$ is a Laplacian regularization to utilize the similar geometric properties of the nearest point in the manifold. α, β and γ are the regularization parameters.

2.6 References

[1] C.U. Grosse, M. Ohtsu, Acoustic emission testing, Springer Science & Business Media, 2008.

[2] K. Ono,2011. Application of acoustic emission for structure diagnosis, Diagnostyka 3-18.

[3] D. Li, Y. Wang, W.-J. Yan, W.-X. Ren,2020. Acoustic emission wave classification for rail crack monitoring based on synchrosqueezed wavelet transform and multi-branch convolutional neural network, Structural Health Monitoring 1475921720922797.

[4] D. Li, K.S.C. Kuang, C.G. Koh,2018. Rail crack monitoring based on Tsallis synchrosqueezed wavelet entropy of acoustic emission signals: A field study, Structural Health Monitoring 17 1410-1424.

[5] V. Soltangharaei, R. Anay, L. Ai, E.R. Giannini, J. Zhu, P. Ziehl,2020. Temporal Evaluation of ASR Cracking in Concrete Specimens Using Acoustic Emission, Journal of Materials in Civil Engineering 32 04020285.

[6] L. Ai, V. Soltangharaei, R. Anay, M.J. van Tooren, P. Ziehl, Data-Driven Source Localization of Impact on Aircraft Control Surfaces, IEEE, 2020, 1-10.

[7] V. Soltangharaei, L. Ai, R. Anay, M. Bayat, P. Ziehl,2021. Implementation of Information Entropy, b-Value, and Regression Analyses for Temporal Evaluation of Acoustic Emission Data Recorded during ASR Cracking, Practice Periodical on Structural Design and Construction 26 04020065.

[8] D. Li, W. Yang, W. Zhang,2017. Cluster analysis of stress corrosion mechanisms for steel wires used in bridge cables through acoustic emission particle swarm optimization, Ultrasonics 77 22-31.

[9] D. Li, M. Tan, S. Zhang, J. Ou,2018. Stress corrosion damage evolution analysis and mechanism identification for prestressed steel strands using acoustic emission technique, Structural Control and Health Monitoring 25 e2189.

[10] Z. Zhang, X. Wu, J. Tan,2019. In-situ monitoring of stress corrosion cracking of 304 stainless steel in high-temperature water by analyzing acoustic emission waveform, Corrosion Science 146 90-98.

[11] V. Soltangharaei, J. Hill, L. Ai, R. Anay, B. Greer, M. Bayat, P. Ziehl,2020. Acoustic emission technique to identify stress corrosion cracking damage, Structural Engineering and Mechanics 75 723-736.

[12] M. Abdelrahman, M.K. ElBatanouny, P. Ziehl, J. Fasl, C.J. Larosche, J. Fraczek,2015. Classification of alkali–silica reaction damage using acoustic emission: A proof-of-concept study, Construction and Building Materials 95 406-413.

[13] Y. Farnam, M.R. Geiker, D. Bentz, J. Weiss,2015. Acoustic emission waveform characterization of crack origin and mode in fractured and ASR damaged concrete, Cement and Concrete Composites 60 135-145.

[14] T. Lokajíček, R. Přikryl, Š. Šachlová, A. Kuchařová,2017. Acoustic emission monitoring of crack formation during alkali silica reactivity accelerated mortar bar test, Engineering Geology 220 175-182.

[15] F. Weise, K. Voland, S. Pirskawetz, D. Meinel, Innovative measurement techniques for characterising internal damage processes in concrete due to ASR, 2012, 20-25.

[16] V. Soltangharaei, R. Anay, N.W. Hayes, L. Assi, Y. Le Pape, Z.J. Ma, P. Ziehl,2018. Damage mechanism evaluation of large-scale concrete structures affected by alkali-silica reaction using acoustic emission, Applied Sciences 8 2148.

[17] L. Ai, V. Soltangharaei, M. Bayat, B. Greer, P. Ziehl,2021. Source localization on large-scale canisters for used nuclear fuel storage using optimal number of acoustic emission sensors, Nuclear Engineering and Design 375 111097.

[18] M.I. Jordan, T.M. Mitchell,2015. Machine learning: Trends, perspectives, and prospects, Science 349 255-260.

[19] I. Goodfellow, Y. Bengio, A. Courville,2016. Machine learning basics, Deep learning 1 98-164.

[20] V. Cherkassky, Y. Ma,2004. Practical selection of SVM parameters and noise estimation for SVM regression, Neural networks 17 113-126.

[21] I.W. Tsang, J.T. Kwok, P.-M. Cheung, N. Cristianini,2005. Core vector machines: Fast SVM training on very large data sets, Journal of Machine Learning Research 6.

[22] H. Zhang, A.C. Berg, M. Maire, J. Malik, SVM-KNN: Discriminative nearest neighbor classification for visual category recognition, IEEE, 2006, 2126-2136.

[23] M. Belgiu, L. Drăguţ,2016. Random forest in remote sensing: A review of applications and future directions, ISPRS journal of photogrammetry and remote sensing 114 24-31.

[24] R. Sun, Y. Chen, A. Dubey, P. Pugliese,2021. Hybrid electric buses fuel consumption prediction based on real-world driving data, Transportation Research Part D: Transport and Environment 91 102637.

[25] I. Goodfellow, Y. Bengio, A. Courville, Y. Bengio, Deep learning, MIT press Cambridge, 2016.

[26] A. Ebrahimkhanlou, B. Dubuc, S. Salamone,2019. A generalizable deep learning framework for localizing and characterizing acoustic emission sources in riveted metallic panels, Mechanical Systems and Signal Processing 130 248-272.

[27] L. Ai, V. Soltangharaei, M. Bayat, M. van Tooren, P. Ziehl,2021. Detection of impact on aircraft composite structure using machine learning techniques, Measurement Science and Technology.

[28] S.J. Pan, Q. Yang,2009. A survey on transfer learning, IEEE Transactions on knowledge and data engineering 22 1345-1359.

[29] S.-X. Chen, L. Zhou, Y.-Q. Ni, X.-Z. Liu,2020. An acoustic-homologous transfer learning approach for acoustic emission–based rail condition evaluation, Structural Health Monitoring 1475921720976941.

[30] L. Gou, H. Li, H. Zheng, H. Li, X. Pei,2020. Aeroengine Control System Sensor Fault Diagnosis Based on CWT and CNN, Mathematical Problems in Engineering 2020.

[31] J.M. Lilly, S.C. Olhede,2008. Higher-order properties of analytic wavelets, IEEE Transactions on Signal Processing 57 146-160.

[32] M.H. Hassoun, Fundamentals of artificial neural networks, MIT press, 1995.

[33] L. Breiman,2001. Random forests, Machine learning 45 5-32.

[34] N.C. Oza, S.J. Russell, Online bagging and boosting, PMLR, 2001, 229-236.

[35] Y. Bengio, P. Lamblin, D. Popovici, H. Larochelle, Greedy layer-wise training of deep networks, 2007, 153-160.

[36] A. Krizhevsky, I. Sutskever, G.E. Hinton, Imagenet classification with deep convolutional neural networks, 2012, 1097-1105.

[37] S. Albawi, T.A. Mohammed, S. Al-Zawi, Understanding of a convolutional neural network, Ieee, 2017, 1-6.

[38] M. Sun, Z. Song, X. Jiang, J. Pan, Y. Pang,2017. Learning pooling for convolutional neural network, Neurocomputing 224 96-104.

[39] B. Graham,2014. Fractional max-pooling, arXiv preprint arXiv:1412.6071.

[40] O.C. Zienkiewicz, R.L. Taylor, P. Nithiarasu, J. Zhu, The finite element method, McGraw-hill London, 1977.

[41] M. Long, H. Zhu, J. Wang, M.I. Jordan,2016. Unsupervised domain adaptation with residual transfer networks, arXiv preprint arXiv:1602.04433.

[42] J. Wang, W. Feng, Y. Chen, H. Yu, M. Huang, P.S. Yu, Visual domain adaptation with manifold embedded distribution alignment, 2018, 402-410.

[43] Z. Zhang, J. Wang, H. Zha,2011. Adaptive manifold learning, IEEE transactions on pattern analysis and machine intelligence 34 253-265.

[44] B. Gong, Y. Shi, F. Sha, K. Grauman, Geodesic flow kernel for unsupervised domain adaptation, IEEE, 2012, 2066-2073.

Chapter 3

Structural Health Monitor of Stainless-Steel Structures for Spent Nuclear Fuel Storage Using Acoustic Emission[1]

[1] Li Ai, Vafa Soltangharaei, Bruce Greer, and Paul Ziehl. Structural Health Monitor of Stainless-Steel Structures for Spent Nuclear Fuel Storage Using Acoustic Emission. To be submitted to a journal

3.1 Abstract

Nuclear power generation has been widely applied in the United States. The dry cask storage system (DCSS) canister has been utilized for the storage of highly radioactive spent fuel for decades. The structural health monitoring of the DCSS stainless-steel canister is urged to evaluate the structural integrity. Acoustic emission (AE) is a nondestructive structural monitoring technique that can offer real-time and long-term degradation detection. This paper investigated the application of long-distance AE monitoring of stress corrosion cracking (SCC) on the DCSS canister. The innovation of the paper lies in the testing on a full-scale 304H stainless-steel plate specimen which was made of similar length and thickness to a realistic SCSS canister. The condition to induce SCC was provided by applying tensile stress at the notch on the plate surface which was exposed to the Potassium Tetrathionate solution. The waveforms and the frequency content of the AE signals acquired in the test were studied. Furthermore, a finite element (FE) model was developed to generate numerical AE signals for the purpose of the AE sensor selection for the field application. The AE signals obtained from the test and the FE model were compared and discussed.

Keywords: Acoustic emission; dry cast storage system; finite element modelling; stainless-steel; stress corrosion cracking

3.2 Introduction

Nuclear power generation is currently one of the major sources of electrical energy in the United States and has been extensively used for decades [1]. The advantages of nuclear power generation are its characteristics of clean and sustainability, in contrast to fossil power generation, nuclear power plants use nuclear fission reactions

to release energy to generate electricity. The generation process does not produce harmful gases such as Sulphur dioxide and does not pollute the air [2]. It also helps to reduce the greenhouse effect and improve the climate by not producing Carbon dioxide [3; 4]. Meanwhile, Nuclear power generation consumes very little nuclear fuel. However, there are some disadvantages. One of the most harmful is that it produces highly radioactive spent fuel, which must be handled with high-level safety standards [5]. In the United States, spent fuel is currently stored in cooling ponds and dry cast storage systems (DCSS). Most DCSS has been in use for over four decades since the 1970s and are about to exceed the operation time that was originally licensed [1]. The new program for the storage of the spent fuel is using the new functional repository. While with the continued delays in the opening of the functional repository. The DCSS currently under operation needs to be inspected to extend the licensed operating time. Stress corrosion cracking (SCC) is one of the main mechanisms of damage to DCSS [6]. The main part of the DCSS is a stainless-steel canister, the top of which is sealed by welding. The whole canister is covered by the concrete overpack to prevent radiation leakage to the outside. The DCSS canister is particularly susceptible to SCC due to the residual stresses in the top welding zone and the high humidity and salinity condition of the coastal area where the DCSS is located [6; 7]. Therefore, the nondestructive inspection of the SCC on the DCSS canister is needed.

Acoustic emission (AE) is a nondestructive structural health monitoring technique. This method is sensitive and has continuous monitoring capabilities [8-13]. It has been widely used for the detection and evaluation of defects in steel structures [14-17]. Yu et al. [14] investigated the prediction of fatigue crack in steel bridge components using AE.

Several AE signal characteristics were studied to build a correlation with the crack behavior. The results indicated that AE absolute energy rate might be a suitable index for the prediction of fatigue life of steel components in the bridge. Hossain et al. [15] utilized AE to study the fatigue damage mechanisms of ASTM A572 grade 50 steel. AE signals were collected during the test and compared with the results provided by digital imaging correlation (DIC) and scanning electronic microscopy (SEM). The authors presented the conclusion that the AE events do not generate in the early stage of fatigue crack growth. Droubi et al. [16] used AE to detect the welding defect in welded joints structures. A Hsu-Nielsen pencil lead break test was conducted to simulate the welding defect on one side of the testing specimen, while the AE sensor was attached on the other side to collect AE signals. The results indicated that AE features such as energy, peak amplitude, and RMS value can be employed to identify the defect in carbon steel welds. Cao et al. [17] studied the damage of Q235A steel during axial tension using AE. The results showed that the cumulative ringing counts of AE can be utilized to represent the damage factor of Q235A steel during the tensile process.

AE also has been employed for the investigation of SCC on steel structures [18-21]. Dongsheng Li et al. [18] used AE to monitor the SCC of the steel wires that are used in bridge cables. The authors developed a particle swarm optimization cluster method to classify AE signals to different clusters and built their relationship with SCC mechanisms. The results pointed out that the AE sources of SCC in bridge cables can be classified into four types: passive film breakdown, detachment of the corrosion product, crack initiation, and crack extension. Dongsheng Li et al. [19] investigated the SCC in prestressed strands using AE. The ant colony optimization algorithm was utilized to do the unsupervised

pattern recognition of AE signals. Four clusters of AE signals can be identified and can be related to four failure stages of SCC. The clustering was employed as the labels of a self-organizing feature mapping neural network. The results indicated that the AE characteristic parameter distribution of different SCC failure stages can be realized. Zhang et al. [20] study the AE monitoring of 304 stainless steel in high-temperature water. A random forest model was used to separate the AE signals of different SCC modes. They extracted several AE features as the input of random forest and observed that the rise time is the most effective feature to distinguish the AE signals. Recently, applications of AE have been investigated to detect SCC on DCSS canisters. Soltangharaei et al. [21] investigated the AE monitoring of SCC on a small-scale 304 stainless steel plate instead of testing on the real-scale DCSS canister. The b-value and linear regression methods were employed for damage identification using AE data. The authors indicated the global b-values and the R^2-values calculated by conducting linear regression can identify the difference of SCC damage in the steel plate.

The results from the previous research indicated that AE monitoring has a good capability to detect and identify SCC events. However, most of these avenues of research were conducted on small-scale specimens and did not study the problems related to the AE monitoring of SCC on a full-scale specimen of DCSS canister. In this paper, the research was conducted based on the previous research of the authors [21]. A full-scale stainless-steel specimen of DCSS canister was fabricated and tested for the feasibility of applying AE monitoring of SCC when the source of SCC and the AE sensor has a long distance. Furthermore, a finite element (FE) model was developed to obtain the numerical AE signals for the AE sensor selection in the field application.

3.3 Materials and experimental setup

A corrosion experiment was conducted on a full-scale stainless-steel plate specimen to simulate a realistic experimental environmental condition for the SCC on a DCSS canister. The specimen is made of 304H stainless steel. According to the previous research [21], a heat treatment was necessary for the initiation and propagation of SCC on the steel specimen. Therefore, in this study, the full-scale steel specimen was vacuum heat-treated in a large vacuum oven. The vacuum heat treat recipe consisted of solution annealing at 1,100°C followed by sensitizing heat treatment at 700°C for two hours followed by 500°C at 24 hours. Samples of the material were cut from the specimen and ASTM A262, Practice A, was performed. The results could be an indicator to observe if the heat treatment was successful in sensitization of the material. Micrographs of the results are presented in Figure 3.1. The ditching around the grain indicated the sensitization was successful. These carbides were formed in the grain boundaries by the bonding of carbon and chromium in the specimen. The ditching around the grain reduced the concentration of chromium and makes the steel specimen more susceptible to intergranular SCC [21].

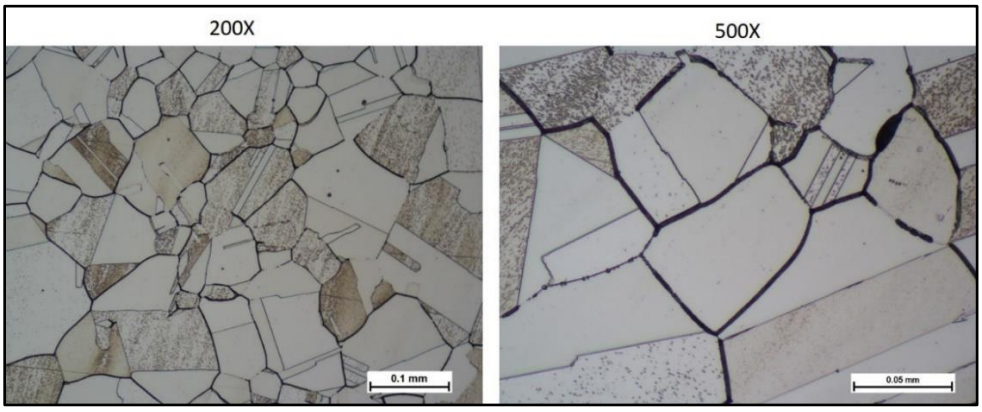

Figure 3.1 Micrographs of material after ASTM 262 Practice A testing at 200 x (left) and 500 x (right)

The primary objective of the experiments was to examine the capability of acoustic emission monitoring on a full-scale DCSS canister when there is a long distance between the AE sensors and the AE sources. The test specimen was made of similar length and thickness to what is typical of DCSS canister shells and of the greatest width that could be managed. This resulted in a specimen size of 198 x 60 x 0.63 in (5029 x 1524 x 16 mm). A 3D model of the specimen is shown in Figure 3.2. Four stress concentrating starter notch was produced on the top surface of the plate. Four sets of two perpendicular welded lugs were fabricated on the bottom side of the plate in the locations of notches. Each lug has a hole located 3 in. (76 mm) from the bottom face of the plate. These holes allow for a 0.75 in. (19 mm) diameter bolt and nut to be inserted through the tabs. Once tightened, the welded tabs are forced toward one another to create the loading on the plate. This action creates bending within the plate, providing the tension that can cause the SCC around the notch's area.

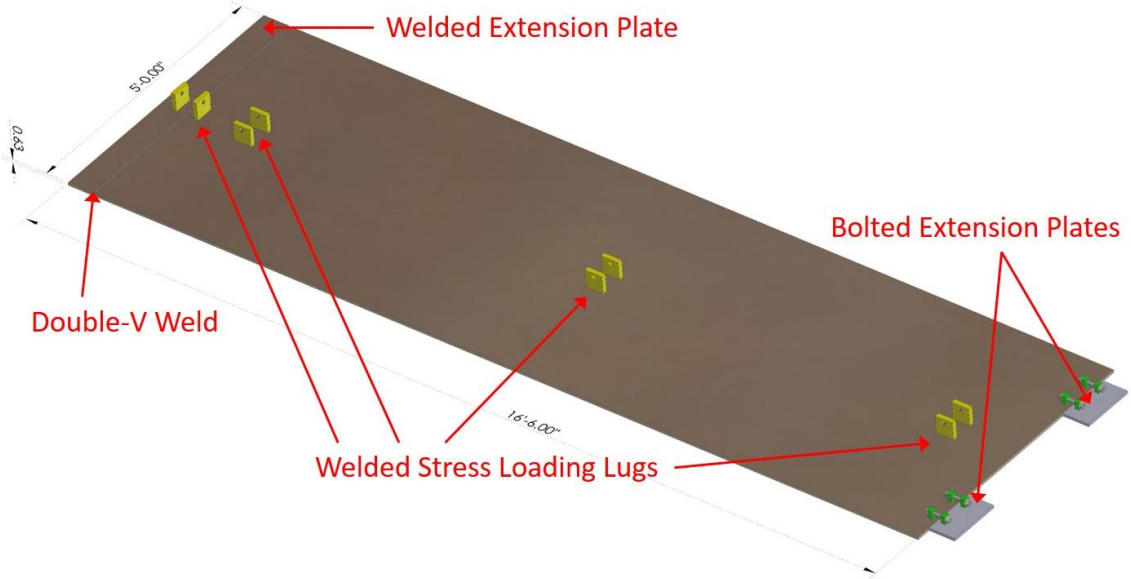

Figure 3.2 Three-dimensional model of the full-scale specimen

In order to achieve realistic stress waves created from the crack extension events, it was desired to apply appropriate stress that less than 90% of the yielding stress [1]. This approach would set a target strain of 0.001500 on the outer surface of the top of the specimen. However, the experiment difficulties with crack initiation were encountered. This situation might be caused by the weld residual stress. The weld zone and heat-affected zone (HAZ) would have the highest levels of tensile weld residual stress [22; 23]. The tension stresses that higher than the yielding stress are needed to counteract the weld residual stress. Therefore, the target strain on the outer surface was increased to 0.002500. This resulted in stress levels exceeding yield on the outer surface but still be within the weld residual stress levels from related research [22; 23]. In this paper, the tension was applied to notch 1 and notch 3 since the SCC of the DCSS canister usually occurred on the edge. Micro-measurement strain gauges were attached to the plate.

Two bolted extension plates were attached to the specimen to simulate the circumstance that the canister is placed on the bottom support. By using the weight of a typically loaded canister of 70,000 pounds and a diameter of 67 inches, and assuming that the contact loading of the base is uniform, the pressure on the bottom surface of a vertical canister is calculated to be 20 psi. For the size of the contact face of the attachment plates, the necessary force for one connection bolt is 37.5 lbs.

The torque applied to the bolt to achieve the stress is calculated using the following equation:

$$T = K * D * F \tag{3.1}$$

where, k represents the bolt torque friction factor, D refers to the diameter of the threaded bolt section, F refers to the desired force to apply.

The required torques for all the bolts are shown in Table 2.1. A 1/2" Drive Beam Torque Wrench (0-150 lb.-ft./0-204 N-m) was applied. To accomplish the target stress in the plate. Micro-measurement strain gauges were attached to ensure the correct loading. The information collected from the gauges was recorded by a P3 Strain Indicator and Recorder (Figure 3.3a).

Table 2.1 Plate loading and bolt torque

Locations	Load	Bolt Torque	Bolt Torque
Notch 1	7560 lb.	1020.6 lb.-in.	85.05 lb.-ft.
Notch 3	7350 lb.	992.3 lb.-in.	82.69 lb.-ft.
Connection	37.5 lb.	5.06 lb.-in.	0.42 lb.-ft.

A corrosive environment on the surface of the plate is necessary for crack initiation. A Potassium tetrathionate (K2S4O6) solution was used to induce SCC at the notch. The solution (1% W @ pH 3) was stored in a tube container (Figure 3.3b), which was attached with silicone on the surface of the plate around notch 1 and notch 3.

Figure 3.3 Micro Measurements P3 strain indicator and recorded

The layout of AE sensors is shown in Figure 3.4. The resonate sensor has a higher selectivity than the broadband sensor when there is a long distance from the source. Therefore, resonant sensors (type R3I-AST) with a frequency response range of 10-40

kHz were attached to the locations further away from the crack event location. Broadband sensors (WDI-AST) with a frequency response range of 100-900 kHz were attached around the crack event location to obtain data for analysis in the frequency domain. The coordinates of the sensors are provided in Table 2.2.

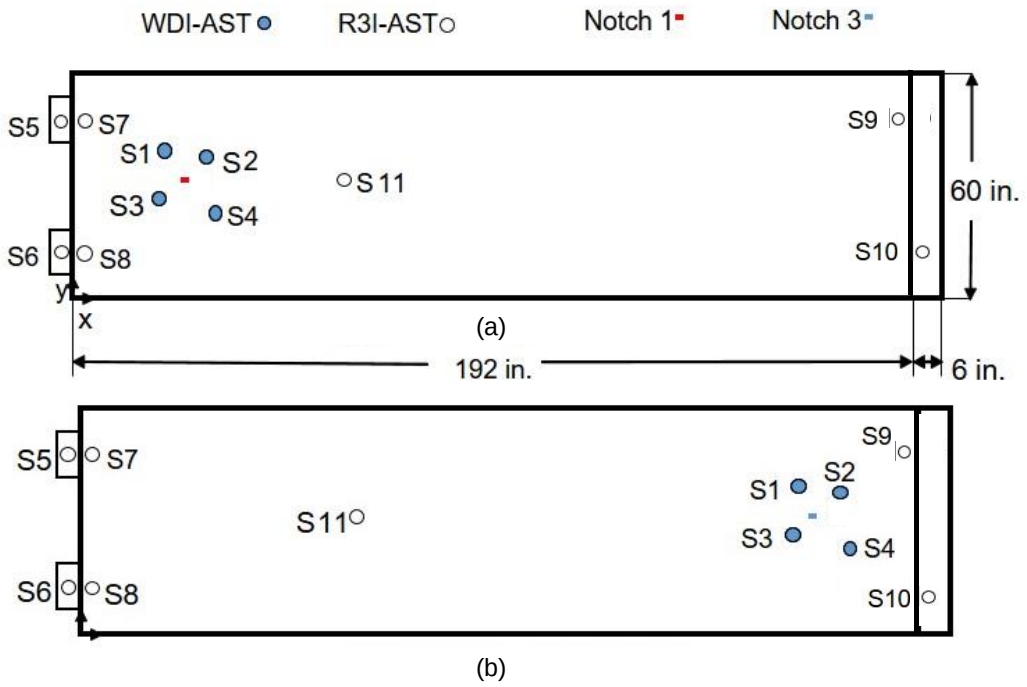

Figure 3.4 sensors layout

Table 2.2 Sensor coordinates

Sensors	Detecting Notch 1 (x, y)	Detecting Notch 3 (x, y)
Sensors 1	(9.75 in., 34.00 in.)	(173.00 in., 34.00 in.)
Sensors 2	(16.75 in., 33.00 in.)	(180.00 in., 33.00 in.)
Sensors 3	(10.75 in., 27.00 in.)	(174.00 in., 27.00 in.)
Sensors 4	(17.75 in., 26.00 in.)	(181.00 in., 26.00 in.)
Sensors 5	(-3.00 in., 50.00 in.)	(-3.00 in., 50.00 in.)
Sensors 6	(-3.00 in., 10.00 in.)	(-3.00 in., 10.00 in.)
Sensors 7	(2.00 in., 50.00 in.)	(2.00 in., 50.00 in.)
Sensors 8	(2.00 in., 10.00 in.)	(2.00 in., 10.00 in.)
Sensors 9	(194.00 in., 50.00 in.)	(194.00 in., 50.00 in.)
Sensors 10	(192.00 in., 50.00 in.)	(192.00 in., 50.00 in.)
Sensors 11	(56.00 in., 30.00 in.)	(56.00 in., 30.00 in.)

Data collected from the sensors were obtained using a 16-channel PCI DISP system (manufactured by MISTRAS Group, Inc. of Princeton Junction, New Jersey). The pre-trigger time, a setting in the software which recovers acoustic waveforms prior to crossing the threshold was set to 256 μs. The sampling rate was set to 1MHz (1,000,000 samples per second). The time from threshold crossing to peak amplitude, peak definition time, was set to 200 μs. The hit definition time, which determines when to stop recording a hit and is typical twice the peak definition time, was set to 400 μs. The hit lockout time, which minimizes recording of late-arriving signals and reflected hits, was set to 200 μs [24]. The calibration of the sensitivity of all the sensors and channels was conducted by applying Hsu-Nielsen sources before starting the test [25].

3.4 Results and analyzing

3.4.1 Visual inspection

The steel specimen was visually inspected after several days. Visible cracks occurred on the plate. The microscopic photos of the corroded area around notches 1 and 3 are provided in Figure 3.5. The cracks around notch 1 were scattered over a large area while around notch 3, two cracks appeared at both sides of the notch.

(a) Notch 1

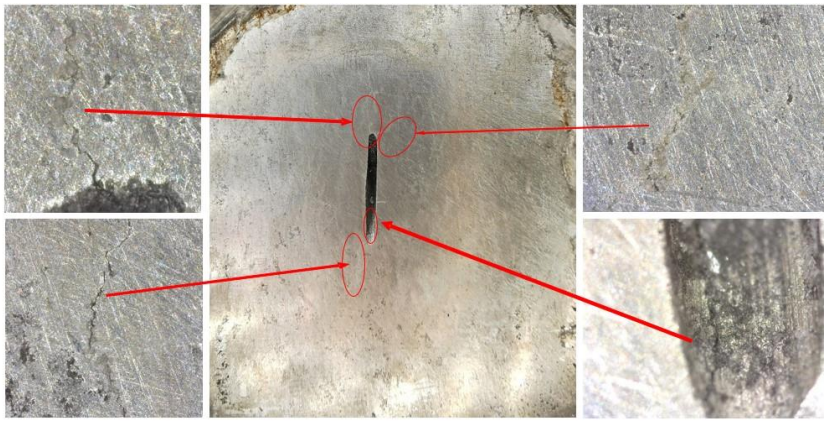

(b) Notch 3

Figure 3.5 Microscopic pictures of the notch

3.4.2 AE data analysis

The suspicious and non-genuine signals were mixed in the AE data during the recording. Therefore, the filtering of the AE data is necessary before analysis can be performed. The AE event that was captured by at least four AE sensors within a specific wave travel time were kept while the AE event that was captured by three or fewer AE sensors were deleted. After the above filtering is completed, the waveforms of the rest data were further visually inspected and any non-genuine data that may remain was deleted.

The filtered AE data captured by the WDI sensors for notch 1 and its cumulative signal strength (CSS) are shown in Figure 3.6a. The jumps in the CSS curve are representative of a new crack initiation event or a crack extension along an existing crack [26]. The initial jump in CSS can be observed around day three, another three major jumps in CSS occur later in the plot. The first major event near day four, a second event around day seven, and a third event occurred around day eight. The filtered AE data captured by the R3I sensors for notch 1 and the corresponding CSS curve are shown in Figure 3.6b. The entire filtered data from all sensor types due to crack extension at notch 1 is shown in Figure 3.6c. The two major jumps of CSS can be observed to occur around days three and four. This indicates that the initiation and propagation of SCC might occur around days three and four.

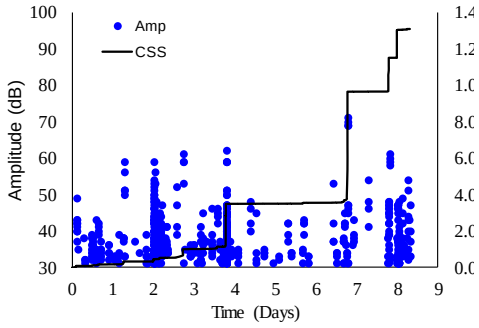

(a) WDI sensors

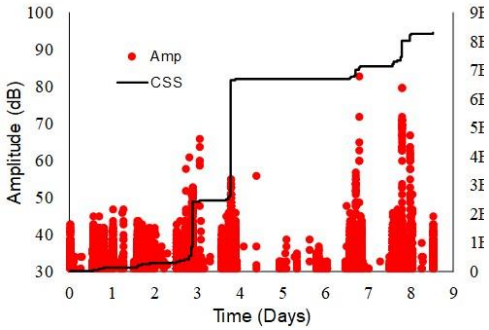

(b) R3I sensors

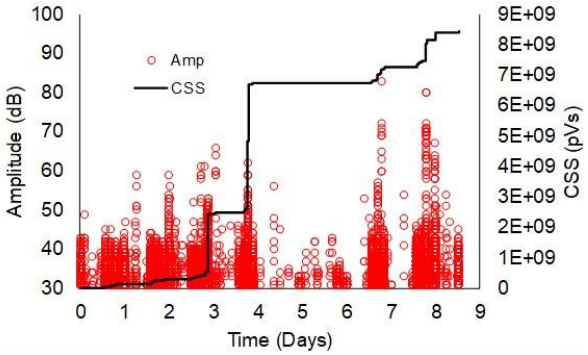

(c) All sensors

Figure 3.6 Filtered AE data showing hit amplitude versus time and cumulative signal strength for notch 1

The filtered WDI sensor data for notch 3 and the CSS curve are shown in Figure 3.7a. The first major jump in CSS occurs around day one. The other three major jumps occur around days two, five, and eight. The filtered R3I sensor data for notch 3 and associated CSS curves are shown in Figure 3.7b. The collective processed data from all sensors for crack extension from notch 3 is shown in Figure 3.7c. The major jumps of CSS happened around days one and five which might be the sign of the initiation and propagation of SCC.

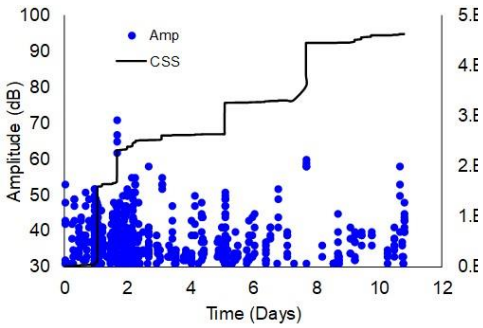

(a) WDI sensors

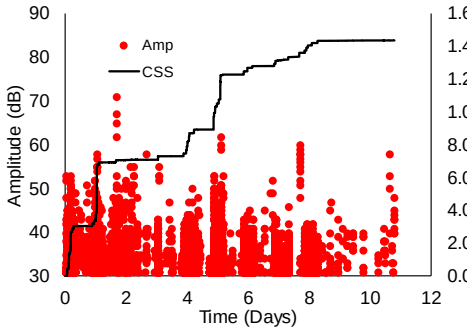

(b) R3I sensors

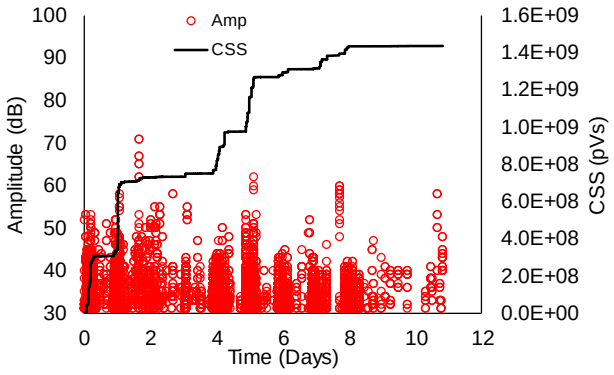

(c) All sensors

Figure 3.7 Filtered AE data showing hit amplitude versus time and cumulative signal strength for notch 3

3.4.3 AE source localization and AE waveforms

A modified time of arrival (TOA) algorithm was utilized to conduct the AE source localization. Akaike Information Criterion (AIC) was employed for a better estimation of motion initiations [27]. More details about the algorithm can be found in the previous research of the authors [21]. The AE data captured by sensors 1-4 were utilized for the source localization. The Crack extension events were located, the location of these events (shown as red dots) and their respective time of occurrence during testing is shown in Figure 3.8a for notch 1, and Figure 3.8b for notch 3.

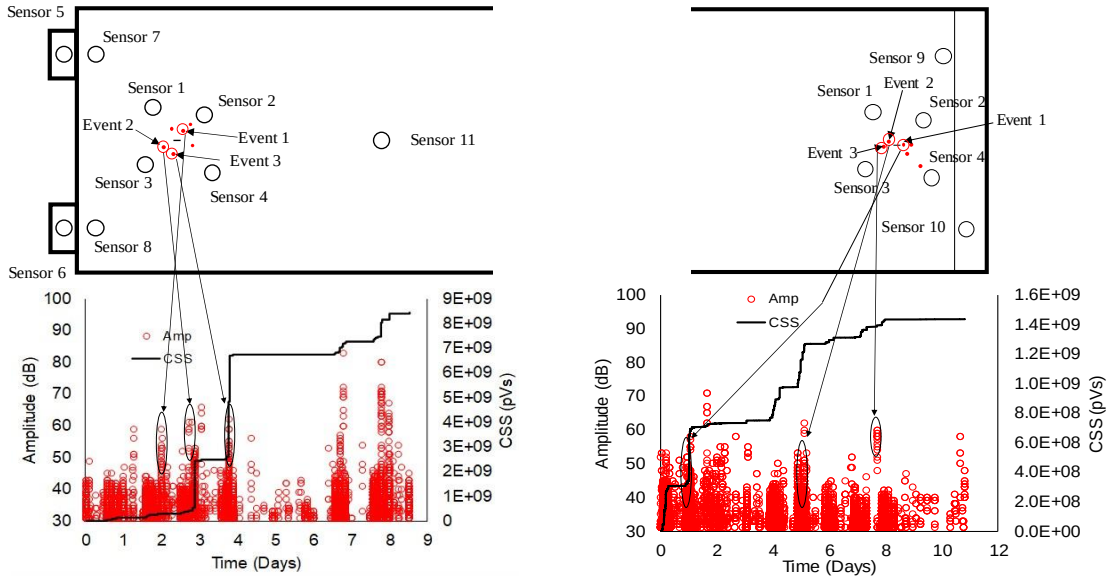

(a) Notch 1 (b) Notch 3

Figure 3.8 Source localization results

The waveforms for all acquired data are recorded through the data acquisition system which can be viewed or extracted for further evaluation. Fast Fourier Transform (FFT) was performed to analyze data in the frequency domain. The waveforms and the FFT magnitude for event 2 in around notch 3 for all the WDI sensors (sensor 1-4), and R3I sensors that far away from notch 3 (sensor 5-8) are shown in Figure 3.9, and Figure 3.10. The waveforms of sensors 5-8 indicated that the resonant sensors have the capability to detect the AE signals from such a long distance, which means the resonate attached on the bottom edge that far away from the top are able to capture the events. A frequency range of the cracking events captured close to the notch (sensor 1-4.) showed that genuine hits fell within a range of 100-300 kHz, three distinct major peaks of FFT magnitude are observed around 145 kHz, 200 kHz, and 270 kHz for the signals of WDI sensors. whereas cracking events captured away from the crack extension events (sensor 5-8) showed that genuine hits fell within a range of 30-100 kHz Two distinct major peaks

are observed around 30 kHz, and 80 kHz for the signals of R3I sensors. the peaks in response are affected by the sensitivity of the sensors selected. This information is valuable for the selection of resonant AE sensors for field applications. A FE model was developed and discussed in Section.4. The model is aimed to generate numerical AE signals. The frequency spectrum of the numerical signals can guide sensor selection.

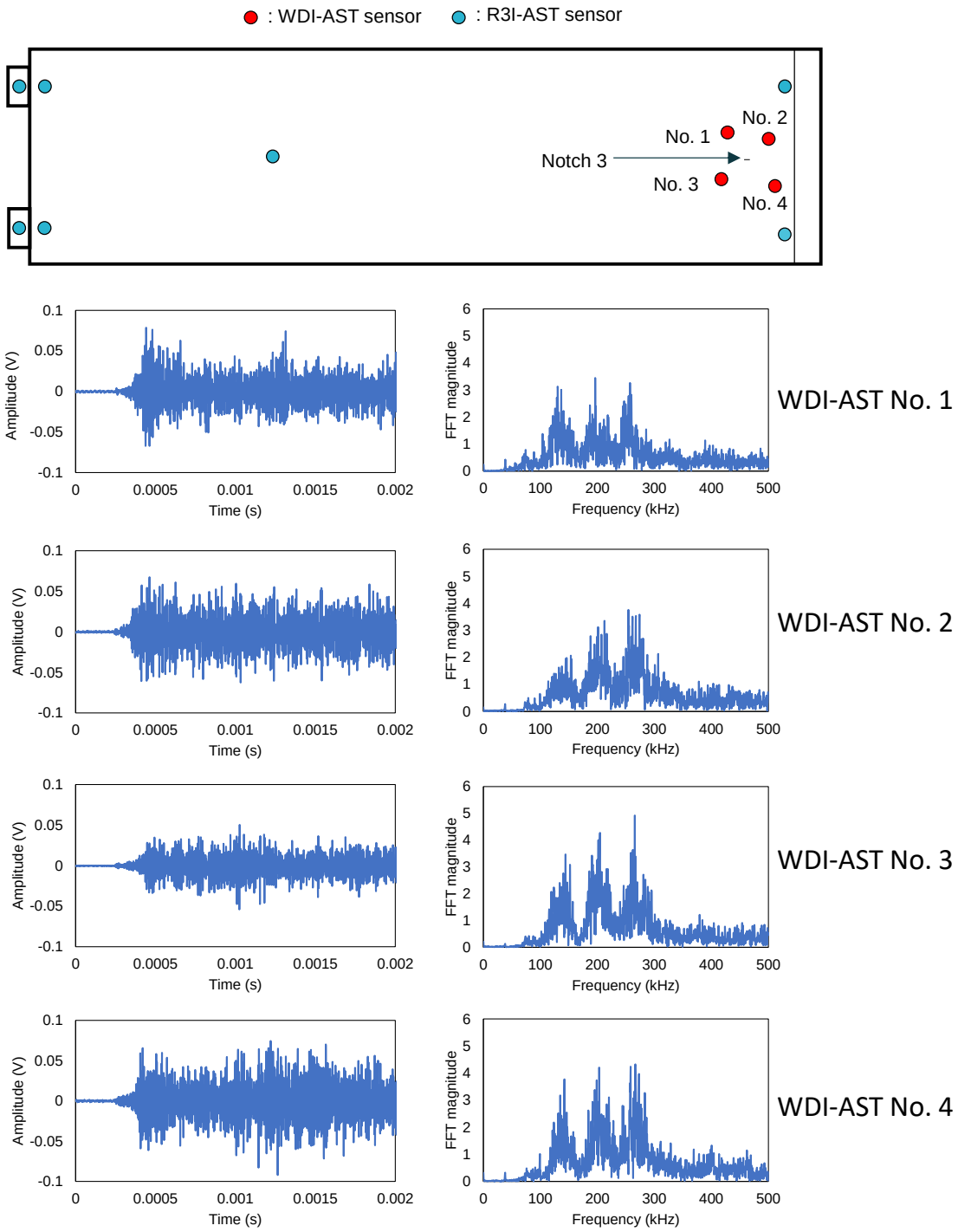

Figure 3.9 Event 2 related to Notch 3 captured by WDI sensor: (left) time domain waveform; (right) FFT spectrum

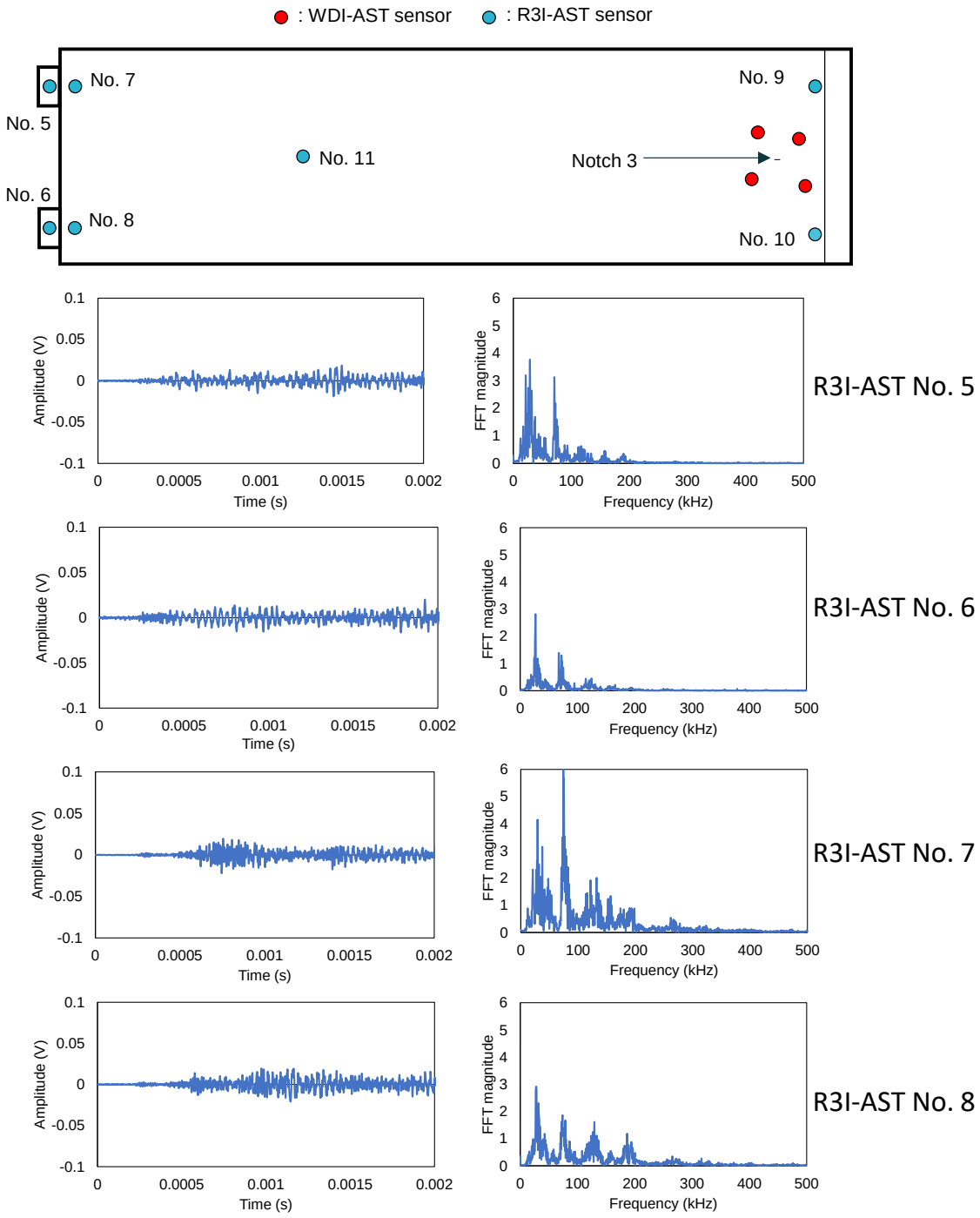

Figure 3.10 Event 2 related to Notch 3 captured by R3I sensor: (left) time domain waveform; (right) FFT spectrum

In the field application, sensors usually are attached to the bottom support structures. It is significant to investigate the attenuation of amplitude and the influence of

the frequency content when the waves travel across the connection. As introduced in Section 2, two bolted small plates were fabricated to simulate the support structures on the bottom. Sensors 7 and 8 were attached near the edge of the large plate. Sensors 5 and 6 were attached to the bolted small plates next to sensors 7 and 8. It can be observed in Figure 3.10, for the AE crack event around notch 3. the amplitude decreased from 0.02 V to 0.018 V when the wave crossed through the bolted gap from sensor 7 to sensor 5. The amplitude decreased from 0.02 V to 0.019 V when the wave crossed through the bolted gap from sensor 8 to sensor 6. Two peaks in the FFT can still be observed in 30 kHz, and 75 kHz. While the magnitude of the peak at 75 kHz decreased, which means the high-frequency content of the signal receive more influence than the low-frequency content when the wave travels across the gap. For the AE crack event on notch 1, the maximum amplitude decreased from 0.042 V to 0.035 V when the wave crossed through the bolted gap from sensor 7 to sensor 5. The maximum amplitude decreased from 0.037 V to 0.031 V when the wave crossed through the bolted gap from sensor 8 to sensor 6 The waveforms of Sensor 5 through 8 for location 1 are shown in Figure 3.11.

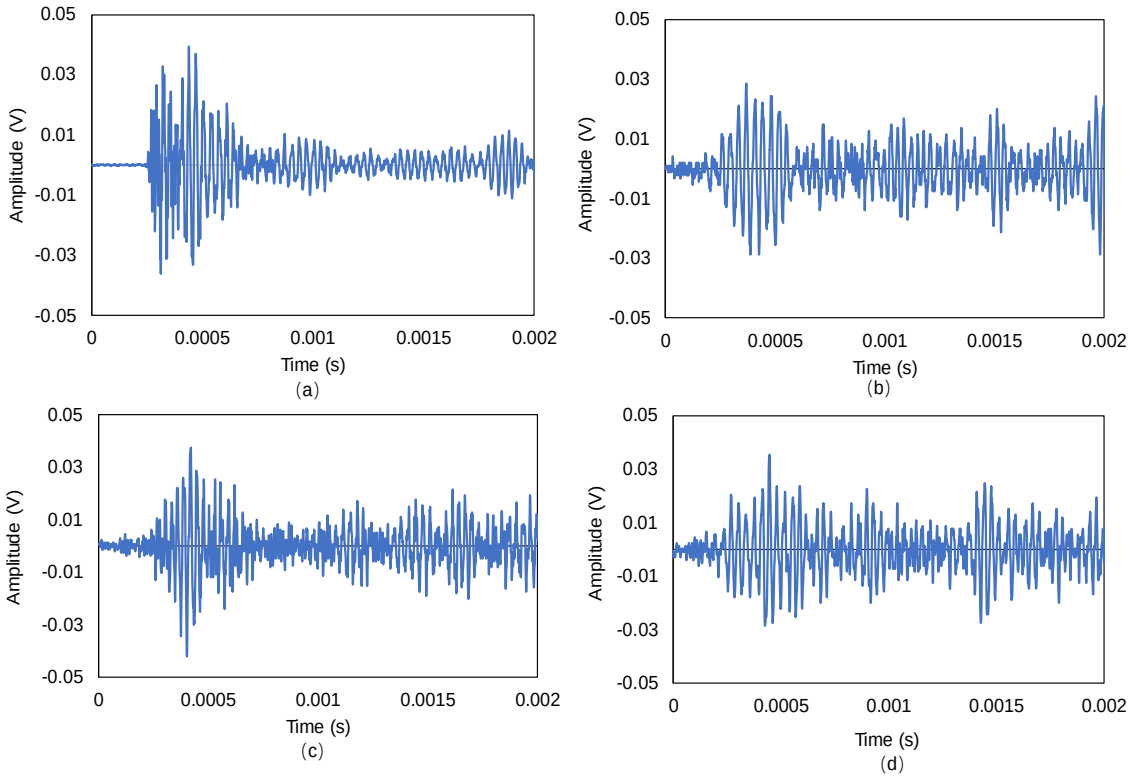

Figure 3.11 Waveforms of signals - Notch 1: (a) Sensor 8; (b) Sensor 6; (c) Sensor 7; (d) Sensor 5

The reduction in amplitude was 16.7% for notch 1 and 10% for notch 3. The decrease in amplitude is acceptable, and the AE acquisition system was able to capture the crack events from notch 3 with sensors 5 and 6 which are attached to the bolted plates and have a long distance from the source. The favorable attenuation characteristics of the signals are primarily attributable to the geometry of the large-scale specimen and this favorable geometry is shared with the field deployed DSS canister.

3.5 FE modeling

3.5.1 Model description

An FE model was developed to obtain the numerical AE signals on the steel plate. The frequency content of the numerical signals can provide guidance for AE sensor selection in the field. The 3-dimensional FE model has the same geometric size as the

experimental steel specimens. The model was developed on the commercial FE platform ABAQUS, the solver is Explicit. By controlling the size of the mesh, the high-frequency dynamic response can be obtained [28-32]. The appropriate mesh size can be calculated by the following equations [33]:

$$v = \sqrt{\frac{E}{\rho} \times \left(\frac{1-\mu}{(1-2\mu)(1+\mu)}\right)} \tag{3.2}$$

$$\lambda = 2v * dt \tag{3.3}$$

$$mesh\ size = \frac{\lambda}{20} \tag{3.4}$$

Where, v refers to the theoretical elastic propagation speed of the P-wave, E refers to the young's modulus of the steel specimen, ρ is referring to the density, μ is the Poisson's ratio. λ represents the length of the wave, dt is the time period of the input source.

Given the property of the steel specimen and the input function that applied in this model, the model was meshed using an element size of 0.002 m, with 8-noded linear brick elements with reduced integration (C3D8R). The output time interval was set to 1×10^{-6} seconds to match the sampling rate of the AE acquisition system. A Gaussian distribution function was utilized as the input source to simulate the SCC on the steel plate. The source was input at the point of event 2 (shown as 'event 2' in Figure 3.12). Observation areas (labeled as 'S1 - S11' in Figure 3.12) were included to capture the modeling results, which are functions of surface displacement versus time.

Figure 3.12 Finite element model representation for steel specimen

3.5.2 Source function

The crack source applied in this study is a Gaussian distribution function [34; 35] as shown in Figure 3.13.

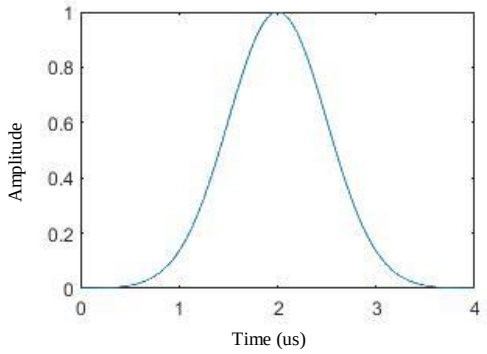

Figure 3.13 Input source function

Eq. (5) shows the source function, where parameter a adjusts the period of the Gaussian distribution function, which influences the frequency content of modeling output. Parameter C adjusts the peak value of the Gaussian distribution function, which influences the amplitude of the modeling output.

$$\delta(t) = \frac{C}{a\sqrt{\pi}} e^{-(t-1/2a)^2} \tag{3.5}$$

Where, C was set to 1.25 to adjust the function peak to unity. The value of a was determined based on several trials to calibrate the model in terms of frequency. Based on comparisons with experimental data, the value of a was set to 0.5. This value resulted in waveforms with a prominent frequency range of 100 to 300 kHz, which is similar to the frequency range of the experimental data.

3.5.3 Output setting

The output of the modeling is the out-of-plan nodal displacement versus time. In reality, the bottom surface of an AE sensor will be excited by the wave and convert the response to electric signals. However, in FE modeling, a node has an infinity small geometry that cannot represent the whole bottom surface of the sensor. Therefore, a combination of multiple nodes would be a strategy to mimic the AE bottom surface. In this paper, the single line output was employed [36]. Only the out-of-plane displacements of nodes in a single straight line away from the input source are recorded. A weight is assigned to each node to account for the fact that the sensor has a circular bottom area. Assume the single line output is a combination of n nodes. The combination can be calculated based on the following equations:

$$w_i = \frac{dy \cdot dx_i}{\sum_{i=1}^{n} dy \cdot dx_i} = \frac{dy \cdot \sqrt{\left(\frac{D}{2}\right)^2 - Cy_i{}^2}}{\sum_{i=1}^{n} dy \cdot \sqrt{\left(\frac{D}{2}\right)^2 - Cy_i{}^2}} \tag{3.6}$$

$$U_{sensor} = \sum_{i=1}^{n} w_i \cdot U_i \tag{3.7}$$

Where, w_i is referring to the weight that assigns to the $i\ th$ node from the left side in the x-direction. dy refers to the distance between two nodes. D is the diameter of the AE bottom area, Cy_i refers to the distance from the $i\ th$ node to the center of the circle. U_{sensor} is the single line output of the sensor, U_i is nodal out of plane displacement of the $i\ th$

node. All the parameters in Eq are shown in the schematic top view of the sensor (Figure 3.14a).

The single line outputs of sensor 1 (WDI sensor) and sensor 7 (R3I sensor) when detecting notch 3 are selected and shown in this paper. Figure 3.14b shows the geometric dimensions of two sensor types and their nodal output definitions in the FE model. The diameter of the bottom surface of both WDI and R3I sensors is 1.125 in (28.6 mm) [37; 38]. The 9 nodes (shown as the red dot) in the straight line away from the source are set up to record the out-of-plane displacement.

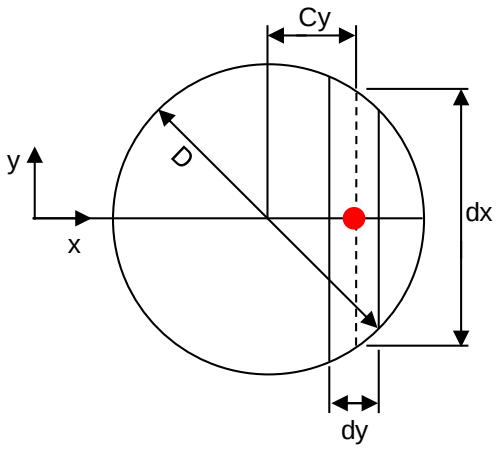

(a) Single line output

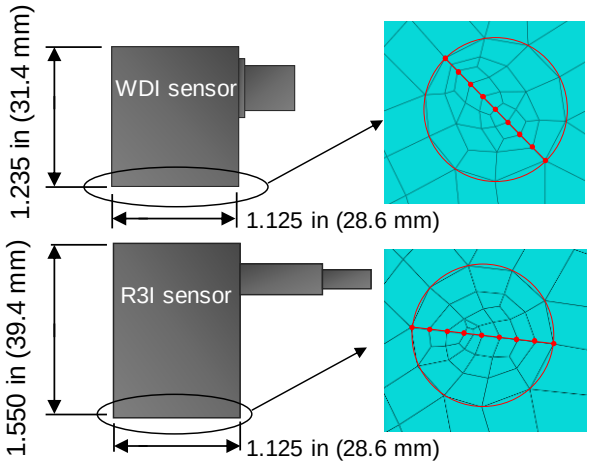

(b) Geometric dimension of AE sensors and the nodal output definition in FE model

Figure 3.14 Output setting

3.5.4 The simulation of AE sensor response

The AE sensors convert the excitation on the bottom piezoelectric materials to electric signals. The signals captured by different types of AE sensors are varying due to the sensors' piezoelectric properties. The stable sensitive frequency range of the WDI sensor is from 100 to 900 kHz. The R3I sensor has a stable sensitive frequency range

around 20-60 kHz. To simulate the frequency response of AE sensors, the bandpass Butterworth filters with the frequency of 100-500 kHz, and 20-100 were developed in MATLAB and used to be consistent with the sensitivity of the WDI, and R3I sensors in terms of frequency. The frequency response curves of WDI and R3I sensors are provided as the red curve in Figure 3.15. The final results of the modeling can be obtained by applying the bandpass filter to the single line output which is introduced in Section 4.3 Output setting.

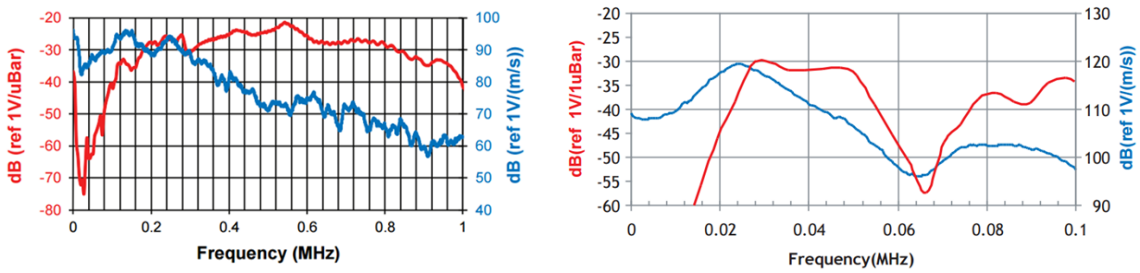

(a) WDI sensor

(b) R3I sensor

Figure 3.15 Frequency response of sensors [37; 38]

3.5.5 Results of FE model

The results of the FE modeling are shown in Figure 3.16. This Figure represents expected wave propagation, in terms of nodal displacement, from the point where the input source was applied. Figure 3.16a shows the wave initiated from the input source at 2×10^{-6} seconds. Figure 3.16b shows that the wave is propagating to the other side of the plate at 8×10^{-6} seconds. It can be observed that the displacement near the location of the input source is much larger than the others. This is due to the low-frequency vibration of the steel plate. The low-frequency vibration noise can be removed by applying the bandpass filter.

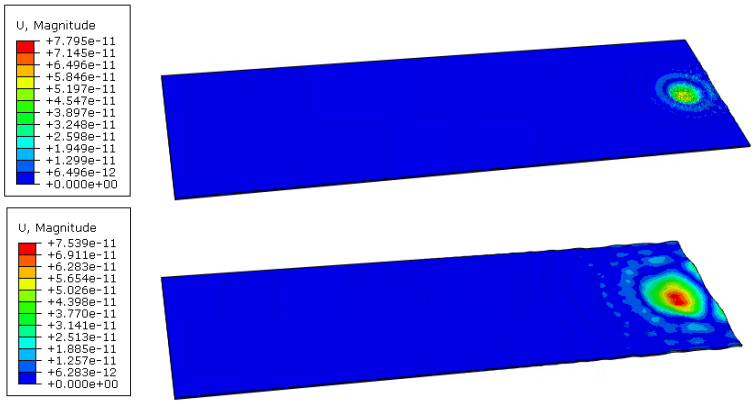

Figure 3.16 Wave propagation results

The numerical signals captured by sensors 1, and 7 were employed to compare with the experimental AE signals. The raw nodal out of plane displacement of the 9 selected nodes (Figure 3.14b) for sensors 1, and 7 are presented in Figure 3.17. Sensor 1 receives a lot of vibration noise. While sensor 7 which is far from the input source was not affected too much by the vibration. The single line combination of the displacement output of the 9 nodes was conducted based on Eq. (5), and (6).

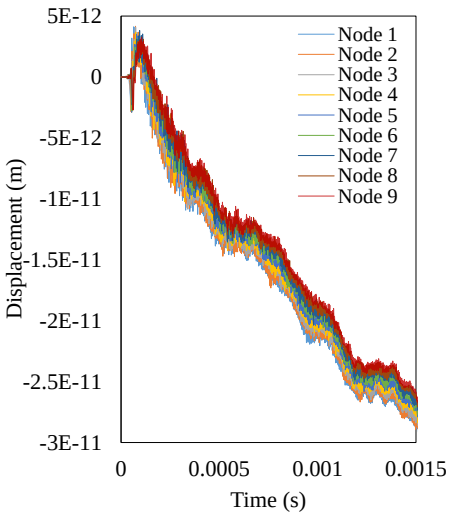

(a) Sensor 1

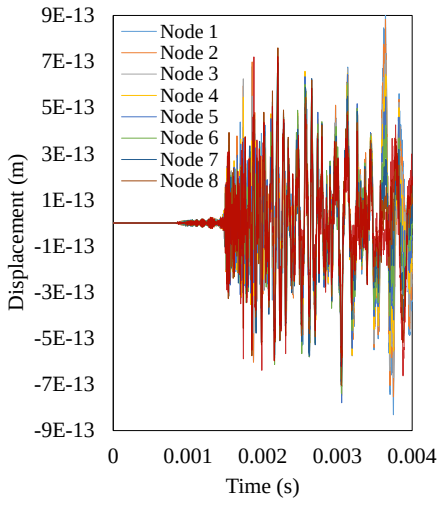

(b) Sensor 7

Figure 3.17 Nodal displacement of all the 9 nodes

The bandpass Butterworth filters were implemented to the single line combination output. Amplitudes of the waveforms after filtering are normalized to the peak amplitude. FFT analysis was conducted, and the experimental signals and FFT versus numerical signals and FFT are presented in Figure 3.18. For results of sensor 1 (Figure 3.18a-18d), It can be observed in Figure 3.18b that most of the low-frequency vibration noise in the numerical signals of sensor 1 was removed after filtering. By observing Figure 3.18c, it can be noticed that the primary frequency of experimental signals of sensor 1 is in the range of 100-300 kHz, three distinct peaks are observed around 145 kHz, 200 kHz, and 270 kHz. In the numerical FFT magnitude (Figure 3.18d), the primary frequency lies in 100-300 kHz which has in agreement with the experimental. While two distinct peaks are observed in similar frequencies with experimental around 130 kHz and 260 kHz, while the peak around 200 kHz is not obvious. These results indicate that the numerical signal of WDI (sensor 1) can simulate the experimental signal in some context, and the primary frequency range is aligned with the experimental signal.

For results of sensor 7 (Figure 3.18e-18h), the numerical waveform (Figure 3.18e) showed a high similarity with the experimental waveform (Figure 3.18f). The primary frequency range of the experimental signal is 30-100 kHz (Figure 3.18g). The peak frequency is around 70 kHz, and the second-largest magnitude can be found at around 30 kHz. In the numerical FFT magnitude (Figure 3.18h), the same primary frequency of 30-100 kHz can be observed, while only one peak around 30 kHz can be observed, the peak around 80 kHz is not obvious. This may be related to the frequency sensitivity of the R3I sensor. As shown in the sensitive curve in Figure 3.15b, the R3I has relatively stable frequency sensitivity in the ranges of 25-50 kHz and 75-100 kHz, but relatively low

sensitivity in the range of 60-70 kHz. This might cause a gap of magnitude around 60-70 kHz, and two peaks around 30, and 80 kHz in the experimental FFT magnitude. However, the simulation of R3I sensor response (introduced in Section 4.4 The simulation of AE sensor response) only has the sensitive range of 30-100 kHz, the gap of sensitivity in 65-70 is not included. The comparison of experimental signal versus numerical signal of the R3I sensor (sensor 7) indicates the FE model can simulate the AE signals that captured by the R3I sensor attached far away from the source. The primary frequency range of numerical signals is aligned with the experimental signal. However, the slight difference in the peak frequency also suggests a more realistic simulation of R3I sensor response is needed in future research.

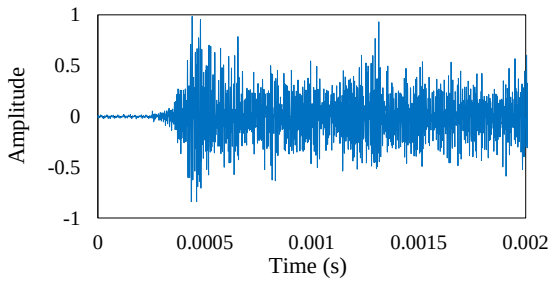

(a) Experimental waveform-sensor 1

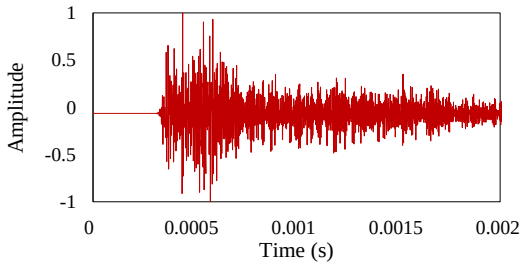

(b) Numerical waveform-sensor 1

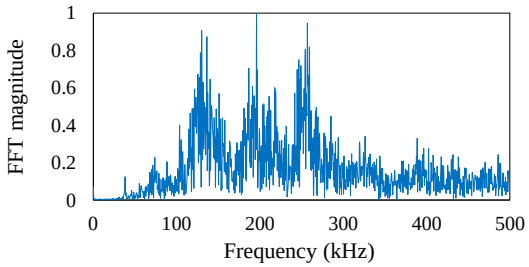

(c) Experimental FFT-sensor 1

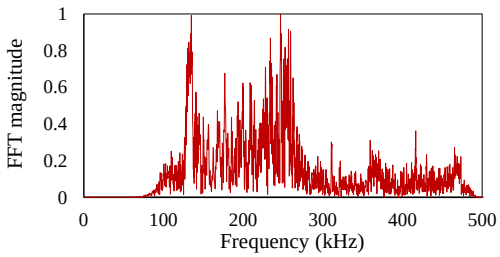

(d) Numerical FFT-sensor 1

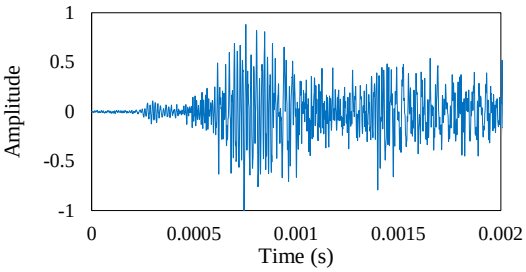

(e) Experimental waveform-sensor 7

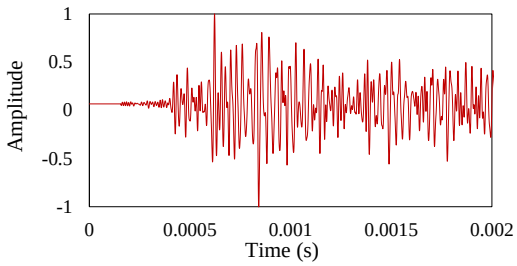

(f) Numerical waveform-sensor 7

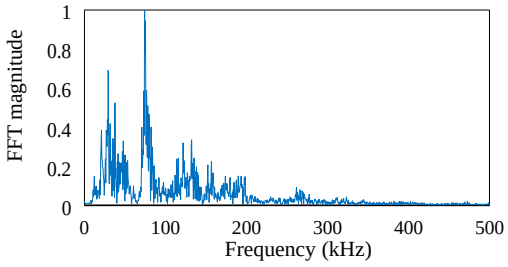

(g) Experimental FFT-sensor 7

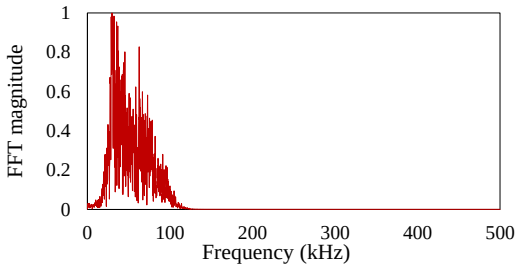

(h) Numerical FFT-sensor 7

Figure 3.18 Experimental signals versus numerical signals

3.6 Conclusions

In this paper, the full-scale steel plate which simulates the real-sized DCSS canister was studied for the AE monitoring of stress corrosion cracking (SCC). Four WDI sensors were attached near the cracks and seven R3I sensors were attached with varying distances from the cracks. The frequency analysis and source localization of SCC events was conducted. Furthermore, a FE model was developed to acquire numerical AE signals. The FE model was compared to the experimental signals.

Pertinent conclusions and observations are as follows:

The R3I sensors attached on the bolted plates away from the crack extension events were able to capture the events, and the decrease in amplitude across the contact surface was minimal. This indicates that attaching resonant AE sensors on the bottom support structures of the DCSS canister for the monitoring of SCC is feasible.

A frequency range of the cracking events captured close to the notch showed that genuine hits fell within a range of 100-300 kHz, whereas cracking events captured away from the crack extension events showed that genuine hits fell within a range of 30-100 kHz. This information is valuable for the selection of resonant AE sensors for field applications.

The frequency content of waves generated by the FE model is similar to the values attributed to the experimental AE data both from the WDI and R3I sensors. The model may be useful for the selection of sensor types located far from crack extension events.

The research will continue to develop a surface output that is more realistic than the single line output, and the advanced filter that simulates the whole sensitivity of the R3I sensor is also the subject of future research.

3.7 Acknowledgments

This research was partially supported by Electric Power Research Institute (EPRI) under project number 1-108781.

3.8 Reference

[1] J.W. Hill,2018. Acoustic Emission Detection In 304H Stainless Steel Due To Intergranular Stress Corrosion Cracking.

[2] N.K. Trehan, R. Saran, Nuclear power revival, IEEE, 2003, 3630-3633.

[3] A. Markandya, P. Wilkinson,2007. Electricity generation and health, The lancet 370 979-990.

[4] S. Rashad, F. Hammad,2000. Nuclear power and the environment: comparative assessment of environmental and health impacts of electricity-generating systems, Applied Energy 65 211-229.

[5] R.C. Ewing,2015. Long-term storage of spent nuclear fuel, Nature Materials 14 252-257.

[6] X. Wu,2020. On residual stress analysis and microstructural evolution for stainless steel type 304 spent nuclear fuel canisters weld joint: Numerical and experimental studies, Journal of Nuclear Materials 152131.

[7] H. Yeom, T. Dabney, N. Pocquette, K. Ross, F.E. Pfefferkorn, K. Sridharan,2020. Cold spray deposition of 304L stainless steel to mitigate chloride-induced stress

corrosion cracking in canisters for used nuclear fuel storage, Journal of Nuclear Materials 152254.

[8] K. Ono,2011. Application of acoustic emission for structure diagnosis, Diagnostyka 3-18.

[9] D. Li, Y. Wang, W.-J. Yan, W.-X. Ren,2020. Acoustic emission wave classification for rail crack monitoring based on synchrosqueezed wavelet transform and multi-branch convolutional neural network, Structural Health Monitoring 1475921720922797.

[10] D. Li, K.S.C. Kuang, C.G. Koh,2018. Rail crack monitoring based on Tsallis synchrosqueezed wavelet entropy of acoustic emission signals: A field study, Structural Health Monitoring 17 1410-1424.

[11] V. Soltangharaei, R. Anay, L. Ai, E.R. Giannini, J. Zhu, P. Ziehl,2020. Temporal Evaluation of ASR Cracking in Concrete Specimens Using Acoustic Emission, Journal of Materials in Civil Engineering 32 04020285.

[12] L. Ai, V. Soltangharaei, R. Anay, M.J. van Tooren, P. Ziehl, Data-Driven Source Localization of Impact on Aircraft Control Surfaces, IEEE, 2020, 1-10.

[13] V. Soltangharaei, L. Ai, R. Anay, M. Bayat, P. Ziehl,2021. Implementation of Information Entropy, b-Value, and Regression Analyses for Temporal Evaluation of Acoustic Emission Data Recorded during ASR Cracking, Practice Periodical on Structural Design and Construction 26 04020065.

[14] J. Yu, P. Ziehl, B. Zárate, J. Caicedo,2011. Prediction of fatigue crack growth in steel bridge components using acoustic emission, Journal of Constructional Steel Research 67 1254-1260.

[15] M. Hossain, J. Yu, P. Ziehl, J. Caicedo, F. Matta, S. Guo, M. Sutton, Acoustic emission source mechanisms for steel bridge material, American Institute of Physics, 2013, 1378-1384.

[16] M.G. Droubi, N.H. Faisal, F. Orr, J.A. Steel, M. El-Shaib,2017. Acoustic emission method for defect detection and identification in carbon steel welded joints, Journal of constructional steel research 134 28-37.

[17] S. Cao, C. Chen, Q. Liu, Damage Factor Analysis of Q235A Steel Based on Acoustic Emission Test, IOP Publishing, 2020, 012124.

[18] D. Li, W. Yang, W. Zhang,2017. Cluster analysis of stress corrosion mechanisms for steel wires used in bridge cables through acoustic emission particle swarm optimization, Ultrasonics 77 22-31.

[19] D. Li, M. Tan, S. Zhang, J. Ou,2018. Stress corrosion damage evolution analysis and mechanism identification for prestressed steel strands using acoustic emission technique, Structural Control and Health Monitoring 25 e2189.

[20] Z. Zhang, X. Wu, J. Tan,2019. In-situ monitoring of stress corrosion cracking of 304 stainless steel in high-temperature water by analyzing acoustic emission waveform, Corrosion Science 146 90-98.

[21] V. Soltangharaei, J. Hill, L. Ai, R. Anay, B. Greer, M. Bayat, P. Ziehl,2020. Acoustic emission technique to identify stress corrosion cracking damage, Structural Engineering and Mechanics 75 723-736.

[22] J. Kusnick, M. Benson, S. Lyons,2013. Finite element analysis of weld residual stresses in austenitic stainless steel dry cask storage system canisters, Technical Letter Report, ML13330A512.

[23] D. Enos, C. Bryan,2016. Final Report: Characterization of Canister Mockup Weld Residual Stresses, US DOE.

[24] A. Laksimi, S. Benmedakhene, L. Bounouas, Monitoring acoustic emission during tensile loading of thermoplastic composites materials, 1999.

[25] N. Hsu, B. FR,1981. Characterization and calibration of acoustic emission sensors.

[26] R. Anay, V. Soltangharaei, L. Assi, T. DeVol, P. Ziehl,2018. Identification of damage mechanisms in cement paste based on acoustic emission, Construction and Building Materials 164 286-296.

[27] H. Akaike, in, Selected papers of hirotugu akaike, Springer, 1998, pp. 199-213.

[28] B. Hosten, M. Castaings,2005. Finite elements methods for modeling the guided waves propagation in structures with weak interfaces, The Journal of the Acoustical Society of America 117 1108-1113.

[29] E.H. Saenger, N. Gold, S.A. Shapiro,2000. Modeling the propagation of elastic waves using a modified finite-difference grid, Wave motion 31 77-92.

[30] M.G. Sause, S. Richler,2015. Finite element modelling of cracks as acoustic emission sources, Journal of nondestructive evaluation 34 4.

[31] M.G. Sause, M.A. Hamstad, S. Horn,2012. Finite element modeling of conical acoustic emission sensors and corresponding experiments, Sensors and Actuators A: Physical 184 64-71.

[32] L. Ai, B. Greer, J. Hill, V. Soltangharaei, R.A.P. Ziehl, Finite element modeling of acoustic emission in dry cask storage systems generated by cosine bell sources, AIP Publishing LLC, 2019, 130001.

[33] S. Yin, H. Xiao, Z. Cui, T. Kundu,2020. Rapid localization of acoustic source using sensor clusters in 3D homogeneous and heterogeneous structures, Structural Health Monitoring 1475921720945195.

[34] J.A. Cuadra, P. Vanniamparambil, D. Servansky, I. Bartoli, A. Kontsos,2015. Acoustic emission source modeling using a data-driven approach, Journal of Sound and Vibration 341 222-236.

[35] J.A. Cuadra, A Computational Modeling Approach of Fracture-Induced Acoustic Emission, Drexel University, 2015.

[36] N. van Rijn,2017. Investigating the Behaviour of Acoustic Emission Waves Near Cracks: Using the Finite Element Method.

[37] MISTRASGroup, Product data sheet for WDI-AST Sensor, Retrieved January, 2021, from http://www.physicalacoustics.com/content/literature/sensors/Model_WDI-AST.pdf.

[38] MISTRASGroup, Product data sheet for R3I-AST Sensor. , Retrieved January, 2021, from http://www.physicalacoustics.com/content/literature/sensors/Model_R3I-AST.pdf.

Chapter 4

Source Localization on Large-Scale Canisters for Used Nuclear Fuel Storage Using Optimal Number of Acoustic Emission Sensors[1]

[1] Li Ai, Vafa Soltangharaei, Mahmoud Bayat, Bruce Greer, and Paul Ziehl. (2021), Source Localization on Large-Scale Canisters for Used Nuclear Fuel Storage Using Optimal Number of Acoustic Emission Sensors. *Nuclear Engineering and Design*, 375, 111097.

4.1 Abstract

The dry cask storage system (DCSS) canisters have been used for the storage of high-level nuclear for decades. The inspections are needed to ensure that structural integrity is maintained. One mechanism of degradation on DCSS canisters that is of interest is stress corrosion cracking (SCC). Acoustic emission (AE) is a non-destructive technique that can be employed as an inspection approach since it can offer real-time degradation detection. This paper presents the approaches that can localize SCC sources by minimal acoustic emission (AE) sensor. To achieve this goal, three machine learning techniques (artificial neural network, random forest, stacked autoencoders) were adopted to improve the conventional source localization approach. In this paper, source localization is treated as a classification problem. The testing specimen was divided into multiple zones and located the AE signals to their corresponding zones. The AE signals were processed to create two datasets: a dataset consisting of AE parametric features and a dataset consisting of AE waveforms. Source localization approaches using artificial neural networks, random forest, and stacked autoencoders were trained and tested based on the datasets. The results show all three machine learning techniques can learn to map AE signals to their sources. Among them, stacked autoencoders have the best performance (97.8% accuracy of stacked autoencoders versus 91.5% of random forest, and 80.0% of ANN), demonstrating that it could be a potential approach to localize SCC events on DCSS canister.

Keywords: Dry cast storage systems; Acoustic emission; Source localization; Machine learning

4.2 Introduction

Nuclear power generation has been widely applied in the United States for decades [1]. Currently, spent fuel is stored in cooling pools and dry cast storage systems (DCSS). DCSS use was initiated in the 1970s. Spent fuels are placed in stainless-steel canisters, then water and air are removed and replaced by an inert gas. These dry storage systems were originally licensed for an operation period of 20 years. With the continued delays in the opening of a functional repository for the storage of these materials, the systems that are currently in operation now will be required to be operational for a significantly longer time. To extend the operation license, the inspections of the DCSS canister are needed to ensure structural operability. Stress corrosion cracking (SCC) has been identified as the main degradation mechanism of concern on DCSS canisters because of the high salinity and humidity in the coastal region where those DCSS canisters are placed [2-4]. Therefore, the in-situ examination for the detection of SCC defects is desirable.

Acoustic emission (AE) is a non-destructive structural health monitoring technique [5-14]. It has been widely used to detect cracks in the infrastructures such as bridges [14], dams [15], and nuclear facilities [16-18]. Recently, applications of AE have been investigated to detect stress corrosion cracking. Soltangharaei et al. [19] utilized AE and pattern recognition to identify the AE signal signatures caused by the propagation of SCC in DCSS. A small-scale 304 stainless steel plate was employed instead of testing on the real-scale DCSS canister. The results indicated that AE monitoring has a good capability to detect and identify SCC events.

However, there is a problem when applying AE monitoring in the realistic DCSS canister. The canisters are very large and are stored in a concrete overpack. Figure 4.1 shows a cutaway mockup of a DCSS canister.

Figure 4.1 Cutaway mockup of simulated dry storage cask system

The available area for sensor attachment is limited. In a recent study about the AE monitoring of DCSS canister, sensors were placed on the bottom support structure of the canister. However, SCC crack would usually occur on the canister far away from the bottom. It is difficult to employ an array of four or more AE sensors around the cracking region to detect the location of a crack using the time of arrival approach. Machine learning techniques could be alternative methods to solve the source localization problem in this situation.

Artificial neural network (ANN) is a field of interest in machine learning [20]. Soltangharaei et al. [21] utilized a back-propagation neural network to localize the impact on aircraft components. Acoustic emission events are collected by a single AE sensor during the impact experiment. AE features such as energy, amplitude, and signal strength were adopted as the neural network's input. The outputs were zonal source localization

results. The results showed that source localization of AE events using a back-propagation neural network has the capability to acquire accurate localization results. However, the problems of locally optimal solutions and explosion gradient [22] have become the main bottlenecks of ANN. Moreover, a good dimension reduction or feature selection is usually needed. Therefore, when applying ANN to the analysis of AE data, appropriate parametric AE features are supposed to be extracted from the original AE signals.

Random forest is one of the present state-of-the-art classifiers based on ensemble learning strategy [23]. It has a fast-training speed, and it is robust to the number of training samples. Moreover, it can provide the ranking of features importance, which means a good feature selection can be obtained instead of manual selection. The random forest has a wide application in fault diagnose. Cerrada et al. [24] built a robust system for the multi-class fault diagnosis in spur gears using genetic algorithms and random forest. An acceptable diagnose accuracy was obtained based on the real vibration signals. Patel et al. [25] presented a random forest classifier as an approach for the classification of bearing fault and feature selection. The most important features of vibration signals were selected and assigned to the random forest model. Results indicated the random forest is turn out to be a suitable approach for fault diagnosis of any rotating machine.

Stacked autoencoders is a deep learning algorithm composed of multi-layer autoencoders. [26]. The concept of deep learning stems from the study of artificial neural networks. The most attractive advantage of deep learning is that no feature selection or dimension reduction is needed [27]. Raw data can be utilized as input. Deep learning combines low-level features to form more abstract high-level features to discover the

distributed feature representations of data. A stacked autoencoder has been utilized for AE source localization. Karvelis et al. [28] studied the structural health monitoring of ship hulls using the acoustic emission method. A stacked autoencoder neural network was employed to obtain the locations of AE events induced by SCC on ship hulls. The source localization approach was validated, and the results indicate that the method can be very effective and efficient.

The goal of this paper is to propose machine learning-based source localization approaches for large-scaled steel structures like DCSS canisters. The Source localization approaches based on ANN, random forest, and stacked autoencoder are proposed and results compared.

4.3 Test Setup and Experimental Procedure

The primary objective of the experiments was to examine the capability of the proposed source localization techniques on the DCSS canister when a single AE sensor is employed on the bottom edge. To simulate a realistic experimental environmental situation for the test setup, a test specimen was made of similar length and thickness to what is typical of DCSS canister shells and of the greatest width that could be managed. This resulted in a specimen size of 5029 x 1524 x 16 mm. The plan view of the specimen is provided in Figure 4.2. The specimen is fabricated from 304/304H stainless steel.

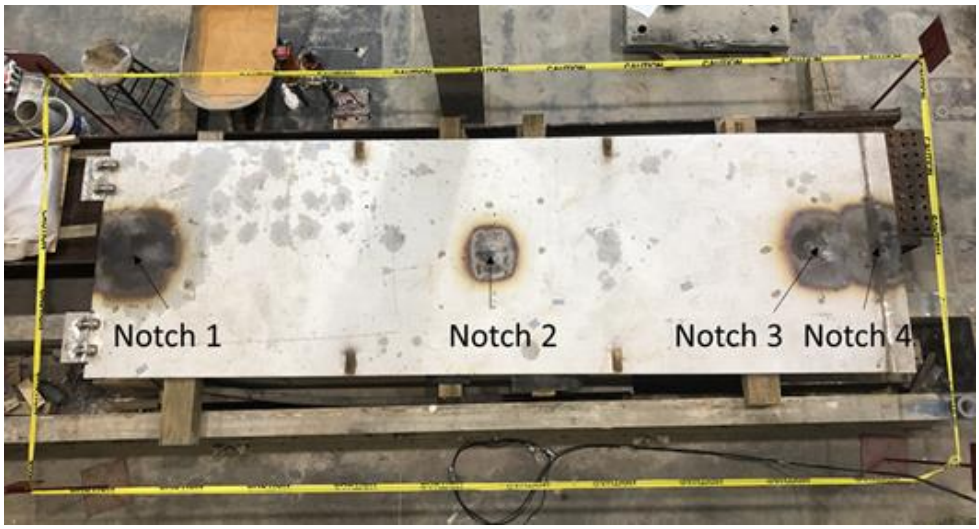

Figure 4.2 Plan view of the specimen

AE is a physical phenomenon related to stress waves generated by the rapid release of elastic energy when cracks or damage are formed in materials [29; 30]. By attaching AE sensors to the surface of an object, AE signals can be detected and recorded. The technique of collecting and analyzing AE signals to diagnose the status of an object is referred to as AE monitoring [31]. The Hsu-Nielsen pencil lead break [32] is one of the widely used artificial sources to generate AE signals by conducting pencil lead break on the object to which the AE sensor is attached. In this paper, A Hsu-Nielsen pencil lead break test was conducted to simulate the cracks that usually initiate on the canister. 135 points were set up on the specimen (marked as red dots in Figure 4.3). The Hsu-Nielsen pencil lead break was repeated 30 times on each of these points. The AE sensor was attached to the upper left corner of the specimen to simulate the circumstance that the sensor is placed on the bottom support of a DCSS canister. 4050 AE events were collected during the experiment.

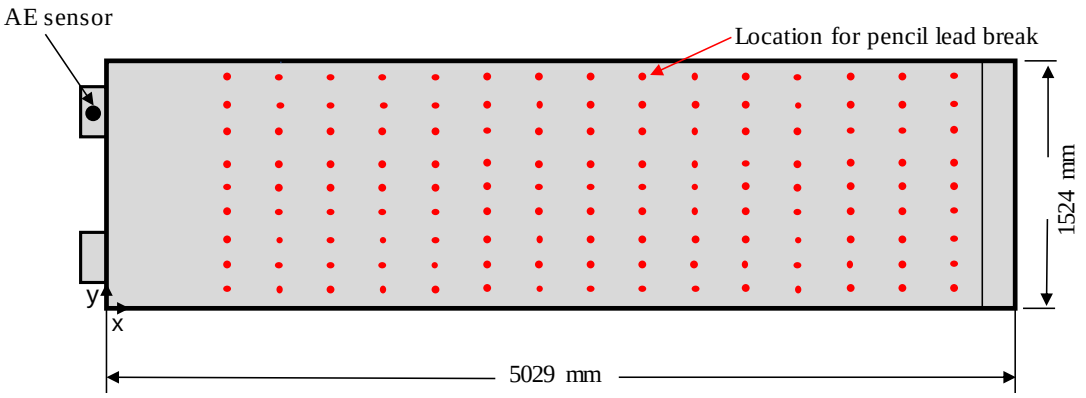

Figure 4.3 Locations of AE sensor and pencil lead breaks

To determine the appropriate AE sensor applied in the study. An attenuation test has been conducted on a resonant sensor (type R3I-AST) with a frequency response range of 10-40 kHz, a resonant sensor (type R6I-AST) with a frequency response range of 40-100 kHz, and a broadband sensor (type WDI-AST) with a frequency response range of 100-900 kHz. Pencil lead breaks were conducted on the specimen with a distance to the sensor from 0 - 5000 mm. The results are provided in Figure 4.4.

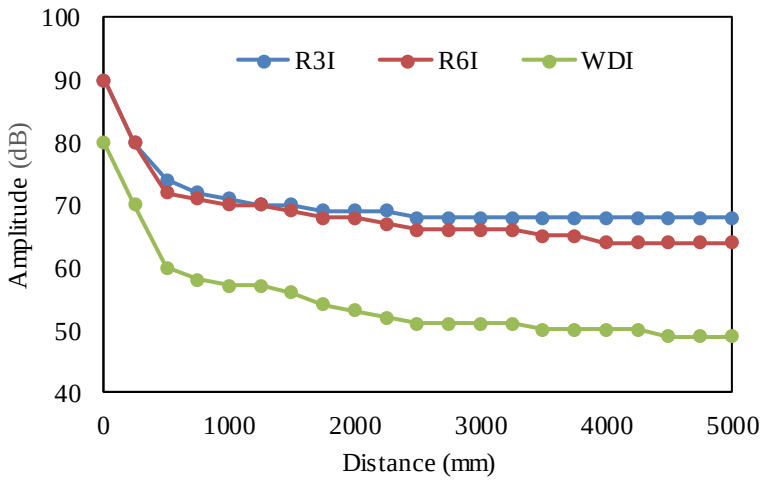

Figure 4.4 Attenuation curves

It can be observed, R3I-AST sensor has the highest sensitivity in long distances. Therefore R3I-AST sensor was employed in this study to ensure the events far away from

the sensor can be detected. The calibration of the AE sensor was conducted by applying the Hsu-Nielsen pencil lead break beside the AE sensor when it was attached to the steel plate. The standard of a reliable and sensitive AE sensor is that the acquired amplitude of the waveform is close to 80 dB for the broadband sensor, and 90 dB for the resonating sensor. It can also be observed in Figure 4.4, when the distance is close to 0 mm, the amplitude of the resonate sensors and the broadband sensor reached 90 dB, and 80 dB. The Data collected from the sensor was obtained using a 16-channel PCI digital signal processing (DSP) system (manufactured by Mistras Group, Inc. of Princeton Junction, New Jersey). The pre-trigger time, a setting in the software, which recovers acoustic waveforms prior to crossing the threshold, was set to 256 μs. The sampling rate was set to 1MHz (or 1,000,000 samples per second). The time from threshold crossing to peak amplitude, peak definition time, was set to 200 μs. The hit definition time, which determines when to stop recording a hit, was set to 400 μs. Its value typically twice the peak definition time. The hit lockout time, which minimized the recording of late arrival signals and reflected hits, was set to 200 μs [33].

4.4 Data Collection

4.4.1 Zone code

The source localization approaches proposed in the paper belong to the family of the paper are the zonal localization method, and AE events will be localized to their corresponding zones. In this paper, the AE events collected in the experiment were divided into five zones. Figure 4.5 shows the zonal divisions. From left to right, the AE events on the specimen are divided into zones 1, zones 2, zones 3, zones 4, and zones 5. There are 810 AE events in each of the zones.

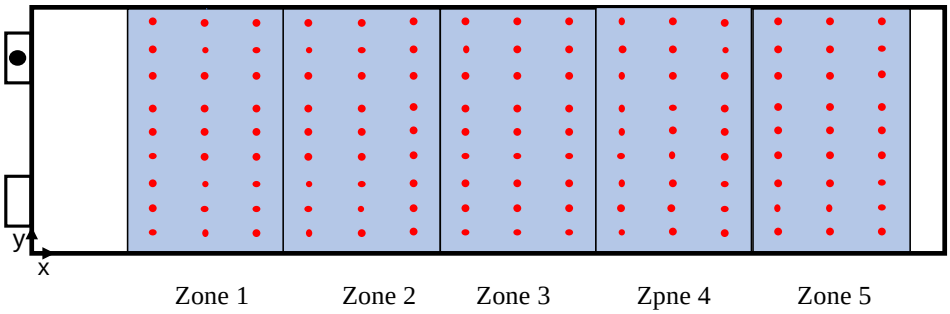

Figure 4.5. Zone codes

4.4.2 Feature-based data

AE features are used to reduce the amount of information carried by the AE signal to a specific value [34]. Those features can represent the characteristics of AE signals in several aspects. For example. “Amplitude” refers to the maximum amplitude at the peak, “Counts” indicates the number of threshold crossings, “Rise time” represents the time interval between the first threshold crossing and maximum amplitude. Fifteen features were extracted from the AE events collected in the experiment. The names and descriptions of the features are provided in Table 4.1. The AE data after feature extraction forms the feature-based dataset, which contains 4,050 data, and each data has 15 sample points. The feature-based data was utilized as the input for source localization approaches using ANN and random forest, which are introduced in Section 4.1 and Section 4.2. The zone codes introduced in Section 3.1 were utilized as labels during training and testing processes.

Table 4.1 Descriptions of the input features for random forest

Features	Descriptions
Amplitude (dB)	The maximum amplitude at the peak
Count	The number of threshold crossings
Rise time (μs)	Time interval between first threshold crossing and maximum amplitude
Duration (μs)	Time between first and last threshold crossing of signal
Average frequency (kHz)	Counts/Duration
Root mean square (RMS) (V)	The effective voltage with a characteristic time T_{RMS} for average ranging from 10 to 1000 ms
Average signal level (ASL) (V)	The effective voltage with a characteristic time T_{ASL} for average ranging from 10 to 1000 ms
Energy	The measure of the electrical energy measured for an AE signal
Absolute energy	The absolute measure of the electrical energy measured for an AE signal
Peak frequency (kHz)	Frequency of maximum signal contribution
Reverberation frequency (kHz)	Frequency after the peak
Initial frequency (kHz)	Frequency before the peak
Signal strength	A parameter to evaluate the AE source strength
Frequency centroid (kHz)	A parameter to characterize the overall frequency content of an AE signal
Counts to peak (PCNTS)	The number of threshold crossings from the first threshold crossing to the peak

4.4.3 Waveform-based data

During AE data acquisition, the sampling rate was set to 1 MHz, and the duration was set to 2,000 μs. An AE waveform collected during the impact test, therefore, has 2,000 sample points. A dataset consisting of original AE waveforms was constructed based on AE events from the experiment. In the waveform-based dataset, there are 4,050 AE waveforms, and each one is a one-dimensional series with 2,000 sample points. This dataset was utilized as the input for the source localization approach using stacked autoencoders. The zone codes introduced in Section 3.1 were utilized as labels during training and testing processes. In each of the five zones, 810 AE signals of pencil lead

break were collected. A single signal was randomly selected from the 810 AE signals of each zone and shown in Figure 4.6. It can be observed that the AE waveforms in different zones have different data distribution patterns. The stacked autoencoders can learn the patterns of waveforms and classify them into the corresponding zones.

All waveforms in the waveform-based dataset were normalized by amplitude to a range of -1 to 1. The specimen is large, and the amplitude of the waveforms, therefore, varies greatly in different zones due to attenuation. If a dataset without normalization is used, the network will focus on the amplitude while other important characteristics may be ignored, significantly impacting the results. To minimize dimensional influences between waveforms, normalization processing is therefore needed [35]. After the original waveforms are normalized, all characteristics are in the same order of magnitude for comprehensive comparative evaluation.

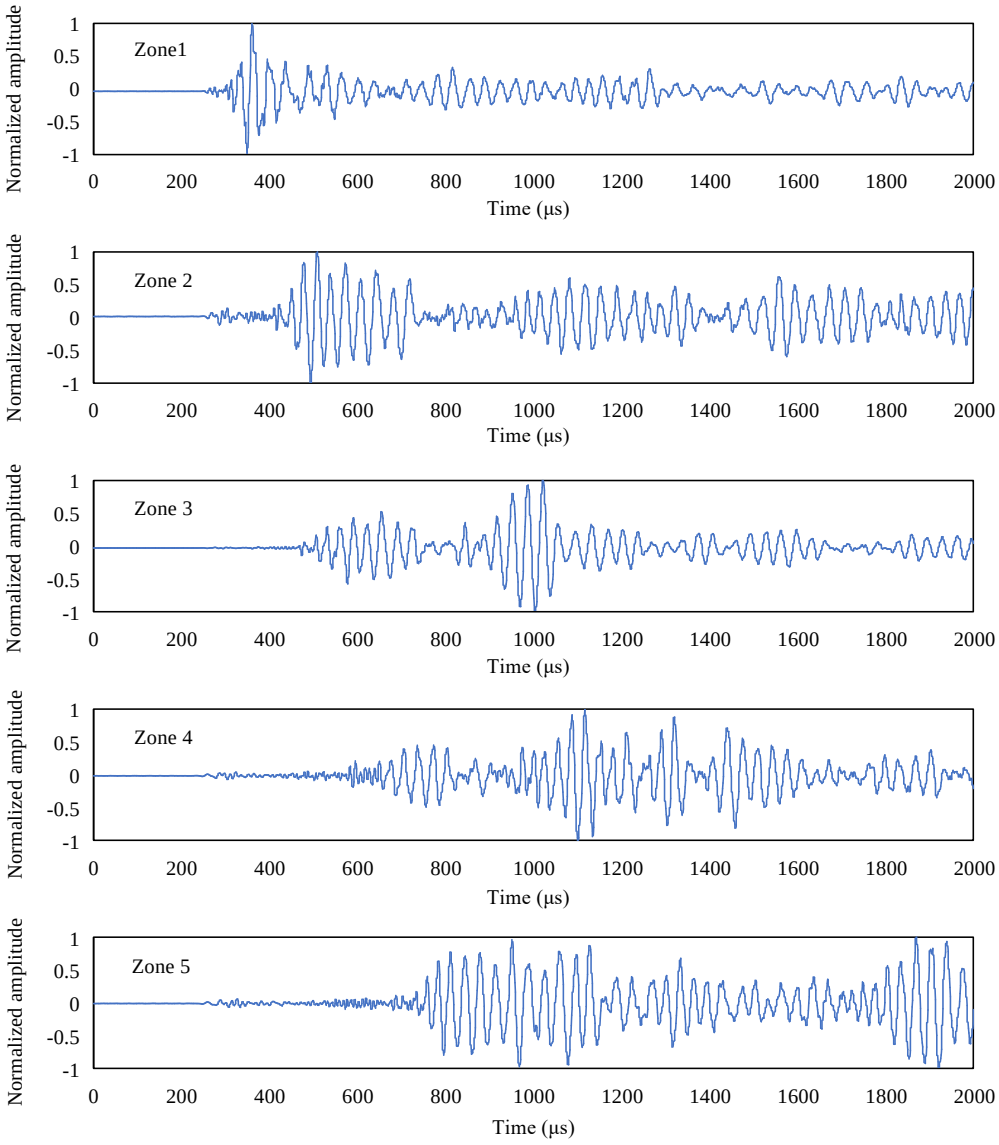

Figure 4.6 The waveform in each zone

4.5 Methods

4.5.1 Back-Propagation Neural Network

Artificial neural networks (ANNs) are information processing systems that mimic how the human brain processes information [36]. The neural network adopted in this section is a back-propagation (BP) network; it consists of an input layer, hidden layers, and an output layer, each layer has many processing elements, called neurons, and each

neuron is connected to each other. The number of neurons in the input layer and the output layer corresponds to the number of variables and the number of outputs. Figure 4.7 shows a simple three-layer artificial neural network consisting of layers j, i, and k. The number of neurons is m for layer j, n for layer i, and l for layer k. $W_{(ij)}$ and $W_{(kj)}$ are weights between layers. The values of m and l are related to the problem for solving, and n is determined by the network designer.

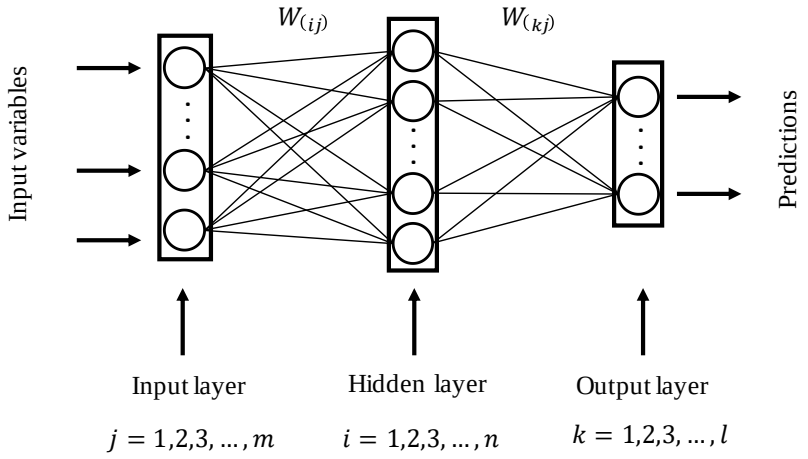

Figure 4.7 Three-layer artificial neural network

The performance of an ANN model depends on the configuration of the network, including the number of neurons in hidden layers and activation functions for each layer. The number of neurons in hidden layers is determined using a trial-and-error method [37]. But some guidelines have been developed to decide the upper limit without losing fidelity in approximating. One commonly used method in determining cap for neurons in hidden layers is:

$$N_{hidden} \leq 2N_{input} + 1 \tag{4.1}$$

where N_{hidden} is the number of neurons in the hidden layers and N_{input} is the number of input variables. However, to avoid overfitting the training data, the number of

neurons should also be determined with consideration of the training sample size. Rogers et al. [38] commend the following relationship:

$$N_{hidden} \leq \frac{S_{train}}{N_{input} + 1} \tag{4.2}$$

where S_{train} is the sample size of training data. Here, we determine the upper limit for the number of hidden layer neurons as the smallest of the values for N_{hidden} calculated by Eq. (1) and (2).

A trial-and-error test was conducted for the selection of ANN model configuration. The process is shown in Table 4.2. The input data of the network is the feature-based AE data introduced in Section 3.2. The zone codes are presented in Section 3.1 were utilized as the labels of the input. It is noticed that the highest accuracy is 80.1%, whose corresponding configuration is two hidden layers with 20 neurons for each of the hidden layers while the lowest (76.6%) accuracy was observed when the corresponding configuration was one hidden layer with 10 neurons. There is some evidence of lower accuracy when neuron numbers reach the upper limit, and generally, networks with 2 hidden layers have better performance than counterparts in one hidden layer model. In this study, two hidden layers with 20 neurons for each of the hidden layers were selected as the configuration of the ANN in AE source localization.

Table 4.2 Artificial neural networks configuration selection process.

Hidden layers	Neurons		Accuracy (%)
	1st hidden	2nd hidden	
1	10	N/A	76.6
	20	N/A	78.9
	31	N/A	77.7
2	10	10	76.9
	20	20	80.1
	31	31	79.1

4.5.2 Random Forest

Random forest (RF) is an ensemble learning method containing multiple decision trees [39]. Decision tree models are trained to be independently, and the results produced by these models are put together, with the final prediction receiving the most votes. At present, the mainstream decision tree algorithm includes C4.5 and classification and regression trees (CART). C4.5 is a decision tree algorithm proposed by Quinlan et al. [40]. C4.5 builds decision trees from a set of training data using the concept of information entropy. In a C4.5 tree, each node can be branched into multiple sub-nodes, the combination of features is not supported in the nodes. C4.5 can only be used for classification problems [41]. For the CART decision tree, each node is branched into only two sub-nodes, supporting a combination of features, and can be used for classification and regression problems [42]. In the random forest, the CART decision tree is a commonly used approach. In this paper, Gini impurity was adopted as the criterion for the branching CART decision tree.

The steps to create a random forest are as follow:

(1) Sample randomization: Assume there is an original dataset named T, which has N samples. By using the bootstrapping method, N samples are taken from the original dataset T with replacement and form a new subset. These N samples in the new subset may contain a sample that has been taken many times or a sample that has never been taken. The probability that a sample has never been taken can be obtained by Eq. (4.3). The limit of the probability can be calculated by Eq. (4.4):

$$h(N) = (1 - \frac{1}{N})^N \tag{4.3}$$

$$\lim_{N\to\infty}\left(1-\frac{1}{N}\right)^{N}=0.368 \tag{4.4}$$

According to Eq. (4), nearly 36.8% of the data in the original data set may not appear in the new subset. This unselected data is called out-of-bag (OOB) data, which can be used to test the decision tree's generalization performance.

(2) Feature randomization: Assume each sample in the new subset has n features. t features ($t \le n$) are randomly selected and transfer to the decision tree. By calculating the information contained in each feature, a feature with the most classification ability is selected for node branching. Genuer et al. [43] recommend the following relationship between n and t:

$$t \approx \sqrt{n} \tag{5}$$

(3) Create a decision tree: By repeating steps (1) and (2) for m times, m subsets that contain t features in each sample can be obtained. Each subset is transferred to an individual decision tree. In other words, m decision trees are created.

(4) Form the random forest: the m trees are formed into a random forest. The decision trees inside the random forest generate their own classification results. The final results are determined according to the number of votes.

An advantage of the random forest is the ability to assess the importance of features [44]. The calculation requires the help of the Gini impurity. By adding noise to one of the features. The new Gini impurity is obtained and compare with the value of the old Gini impurity before adding the noise. The difference between the Gini impurities is utilized as a measure of the importance of this feature.

In this paper, a random forest classification model contains 800 decision trees was adopted for AE data source localization. The feature-based AE dataset, which was

introduced in Section 3.2, was utilized for training and to test this approach. By using the Bootstrapping method, 800 subsets were drawn from the original AE dataset. Each sample in the new subsets has 4 features that were randomly selected from the original 15 features. The number of features in the new subset was determined by Eq (6). The subsets were assigned the decision trees. These decision trees inside the random forest work independently and generate their own localization results. The final result is given by voting. Figure 4.8 shows the random forest used in this paper. The output of the random forest model is the zoning code of the corresponding AE event.

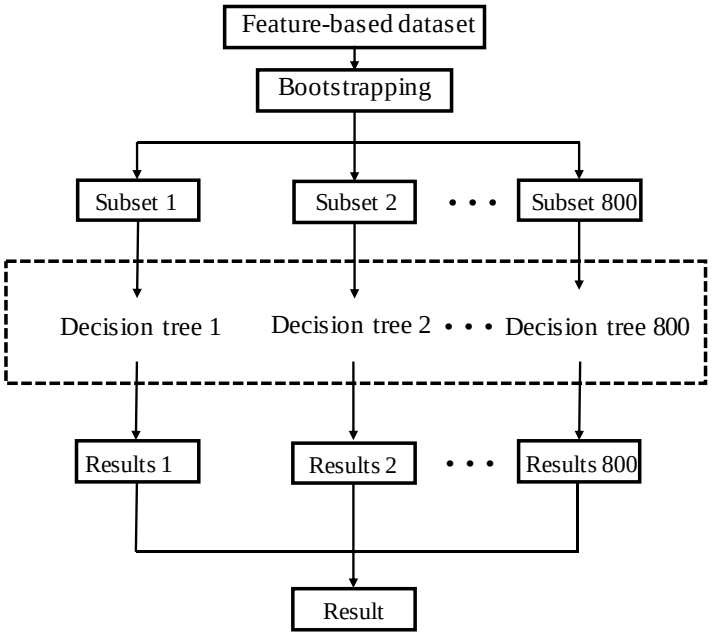

Figure 4.8 The architecture of the random forest

Generally, the error of random forest will decrease with the increase of the number of decision trees. Once the number of decision trees increased to a certain number, the error of the model will converge to a certain value. Continue to increase the number of decision trees will not reduce the error but increase the computational cost of the entire random forest. Therefore, an appropriate number of decision trees is critical to

the optimization of the random forest. To determine the number, the random forest model was tested with tree numbers varying from 200 to 2000, with an interval of 200. The zoning code introduced in Section 3.1 was utilized as the labels of the input feature-based AE data. The determination process of the number of trees is shown in Table 4.3. The classification mistake rate keeps decreasing before the number of trees reaches 800, while no significant change of classification error can be observed when the number of trees continually increased to 2000. However, a small fluctuation can still be observed, and this is because, in a random forest, each decision tree randomly selects training samples in a given training dataset based on bootstrapping. The decision trees within two random forests (e.g., random forests with 800 trees and 1000 trees) are different, which results in a small fluctuation when the tree number increase from 800 to 2000. While the general trend is towards a plateau. Comprehensively considering all the above, the number of decision trees is defined as 800 in this paper.

Table 4.3 Description of the selection process of trees number

Trees number	Error (%)
200	14.7
400	11.8
600	10.1
800	9.5
1000	9.8
1200	9.9
1400	9.6
1600	9.5
1800	10.1
2000	9.9

4.5.3 Stacked Autoencoder

Autoencoder is a three-layer neural network model with an input layer, hidden layer, and output layer [45]. The network structure is shown in Figure 4.9. The input

layer and the output layer have the same dimension, while the hidden layer has a smaller dimension.

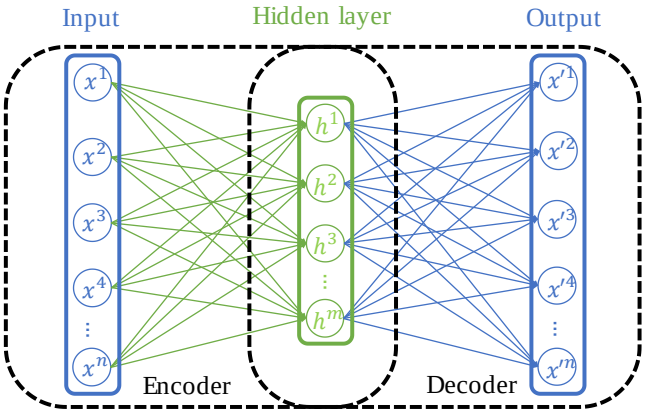

Figure 4.9 Scheme of autoencoder

Assuming the input data is a n dimensional vector $\{x^1, x^2, x^3 \dots x^n\}$, the process of mapping the input data to the m ($m < n$) dimensional vector $\{h^1, h^2, h^3 \dots h^m\}$ in the hidden layer through the nonlinear encoding function E is named as encoder stage. The process of mapping the m dimension vector in the hidden layer to the n dimension vector $\{x'^1, x'^2, x'^3 \dots x'^n\}$ in the output layer through the decoding function D is named as decoder stage. The encoding function E and the decoding function D are presented in Eq. (4.6) and Eq. (4.7):

$$h = E(x) = S_\theta(wx + b) \tag{4.6}$$

$$x' = D(h) = S_{\theta'}(\mathrm{w}'h + b') \tag{4.7}$$

Where, $\{\theta,\ \theta'\} = \{w,\ \mathrm{w}',\ b,\ b'\}$ is the mapping parameter set in the autoencoder. w and w' are the weights of encoding and decoding stages; both are $m \times n$ dimensional matrix. b and b' are the n dimensional bias vectors of encoding and decoding stages. S is the activation function. The activation function for the autoencoder in this paper is a sigmoid function (Eq. (4.8)):

$$f(x) = \frac{1}{1 + e^{-x}} \tag{4.8}$$

The process of transferring the input vector $\{x^1, x^2, x^3 \ldots x^n\}$ to the output vector $\{x'^1, x'^2, x'^3 \ldots x'^n\}$ is called reconstruction. The training object of the autoencoder is to minimize the error in data reconstruction by constantly adjusting the mapping parameters set $\{\theta,\ \theta'\} = \{w,\ \mathrm{w}',\ b,\ b'\}$. A training process of N iterations can be expressed By Eq. (4.9):

$$\theta,\ \theta' = \mathrm{argmin}\frac{1}{N}\sum_{i=1}^{N} L\left(x^i, x'^i\right) = \mathrm{argmin}\frac{1}{N}\sum_{i=1}^{N} \left\|x^i - x'^i\right\|^2 \tag{4.9}$$

Where, x^i and x'^i refer to the ith element in the input and output vector. L is the mean squared error between x^i and x'^i.

By minimizing reconstruction errors, the vector in the hidden layer well preserves the information contained in the input vector; in the meantime, the dimension is significantly reduced [40]. Therefore, the vector $\{h^1, h^2, h^3 \ldots h^m\}$ in the hidden layer can be seen as the feature set extracted from the input vector.

The classification stacked autoencoder consists of multiple autoencoders and a softmax layer [46]. The first autoencoder extracts the feature set of the input data and takes the obtained feature set as the input data of the next autoencoder for further feature extraction. All the training processes in autoencoders are unsupervised training, and no labels are needed in this stage. The feature set from the last autoencoder is used as the input of the softmax classifier for supervised training. The corresponding classes of each input data are required to be known as the labels. Assume the inputs contain k classed. The final output of a stacked autoencoder is a k dimensional vector; each element

represents the probability that the input belongs to this class. The class with the highest probability can be considered as the classification result.

The stacked autoencoder network utilized in this paper has two autoencoders. The first autoencoder has a hidden size of 100, and the second autoencoder has a hidden size of 50. Different from ANN and random forest, the input data of the network is the waveform-based AE data introduced in Section 3.3. The corresponding zone code of the AE data is utilized as the labels in the training of the softmax layer. A source localization result is obtained as the output of this stacked autoencoder neural network. Figure 4.10 shows the structure of the stacked autoencoder applied in this paper.

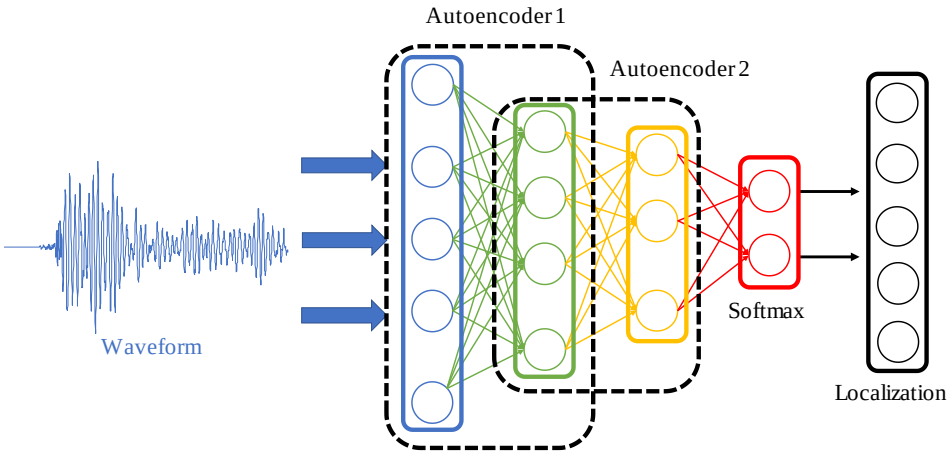

Figure 4.10 Stacked Autoencoder network with two autoencoders

4.6 Results and Discussion

4.6.1 Source localization using BP-ANN

The feature-based AE dataset was adopted in the scenario of source localization using ANN. In the 4050 data collected during the experiment, 2025 AE data were randomly selected for training, 675 AE data were randomly selected for validation. The remaining 1350 data were utilized to test the performance of the trained ANN. The

source localization results are shown in Figure 4.11a as a confusion matrix. The numbers of AE data that are correctly localized in their corresponding zones are shown in the main diagonal of the confusion matrix. There were 1080 AE events correctly located in the corresponding zone, accounting for 80% of the total AE data. In other words, the overall accuracy was 80%. In addition to accuracy, precision, and recall for each class are usually implemented to evaluate the performance of classification in each class [47]. The value of precision is obtained by Eq. (4.10):

$$Precision = \frac{TP}{TP + FP} \tag{4.10}$$

Where TP refers to true positives, which means the number of samples that correctly classify into the corresponding class, FP refers to false positives, which is the number of samples that do not belong to the class but are classified into the class by error. Precisions of the five class are respectively 86.9%, 76.6%, 76.7%, 75.5%, 87.4% from zone 1 to 5.

The value of recall can be obtained by Eq. (4.11):

$$Recall = \frac{TP}{TP + FN} \tag{4.11}$$

Where FN refers to false negatives, the number of samples that belong to the class but are classified into the other classes by error. Recalls of the five classes are respectively 84.6%, 79.0%, 77.5%, 75.5%, 83.2% from zone 1 to 5.

Precision and recall influence each other. A class with high precision usually has a low recall and vice versa [48]. To comprehensively evaluate the efficiency of the classifier in each class, the F1-score can be employed.

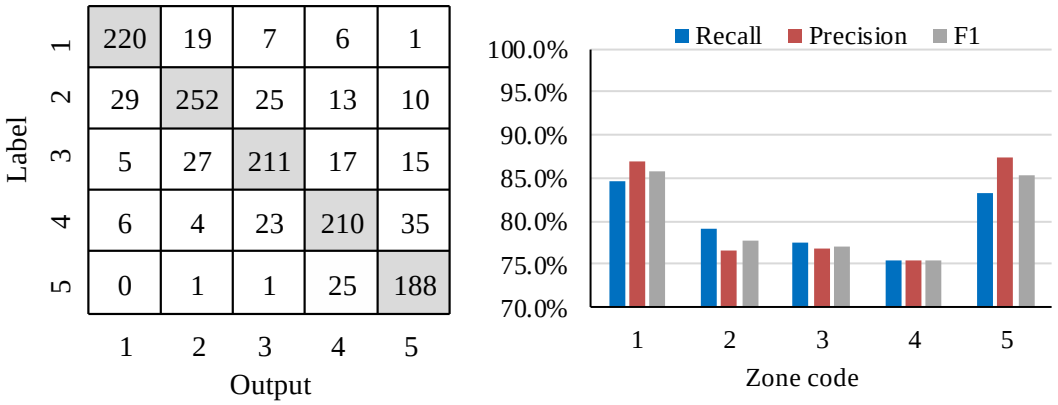

(a) (b)

Figure 4.11 Performance of each classification using ANN: (a) confusion matrix; (b) evaluation of each zone

F1-score, also referred to as the balanced F score, is defined as the harmonic mean of precision and recall [49]. It can be provided by Eq. (4.12):

$$F1 = \frac{2\times Precision\times Recall}{Precision+Recall} = \frac{2TP}{2TP+FP+FN} \quad (4.12)$$

F1 of the five classes are respectively 85.7%, 77.8%, 77.1%, 75.5%, 85.2% from zone 1 to 5. The values of precision, recall and F1 for each class are compared and shown in Figure 4.11b. Zones on the edge (zone 1 and 5) performed better than the inner areas (zones 2, 3, and 4). This situation occurs because when localizing the events in the inner zone, the misclassification events were almost localized in the nearby zones. While the zones near the edge have one nearby zone, misclassification occurred primarily in that zone only.

The computing time for the training process on an intel i-7 four-core CPU was 7.96 seconds. The computing time required for the testing data running on a trained ANN was 0.02 seconds.

4.6.2 Source localization using random forest

The data used for the training of this network were 2,700 feature-based AE signals randomly selected from all 4,050 data. The remaining 1,350 signals were utilized

for testing. Figure 4.12a shows the confusion matrix of the random forest source localization result. Overall, the accuracy on the test set was 90.5%. 1,222 AE signals were correctly localized, while 128 were in error. The number of AE signals correctly localized in their corresponding zone is shown in the main diagonal of the confusion matrix (Figure 4.12a). Figure 4.12b shows the precision and recall for each zone. From zone 1 to 5. Precision of the five classes is respectively 94.8%, 90.1%, 92.6%, 86.6%, 88.8%. Recall of the five classes are respectively 94.8%, 92.0%, 91.2%, 85.7%, 88.8%. F1 of the five classes are respectively 94.8%, 91.0%, 91.9%, 86.1%, 88.8%. Zone 1 performed the best rather than the other zones (zones 2, 3, 4, and 5). This might be caused by the attenuation of signals during the transmission. Zone 1 has the smallest distance from the AE sensor, which results in the signal from zone 1, retaining the complete information.

The computing time for the training process within an intel i-7 four-core CPU was 4.03 seconds. The computing time for testing was 0.02s.

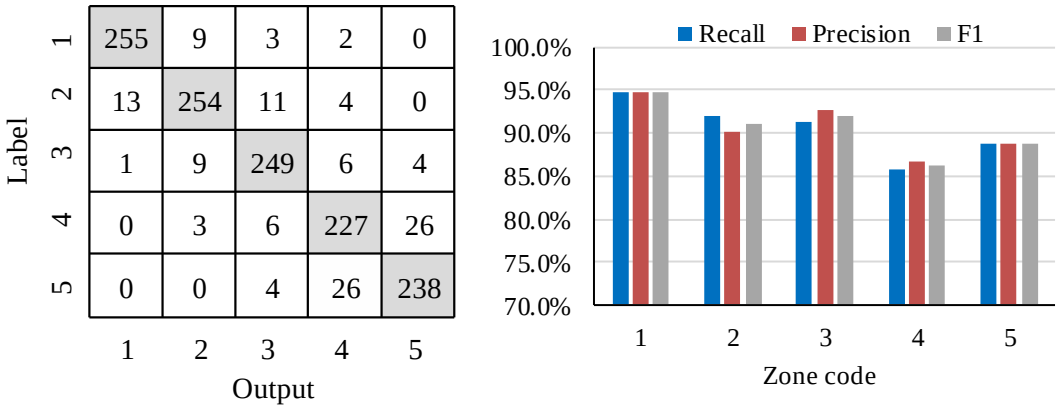

Figure 4.12 Performance of each classification using random forest: (a) confusion matrix; (b) evaluation of each zone

The importance percentage of AE features can be provided by the random forest model. The names of all 15 features and their corresponding percentages of importance are shown in Figure 4.13a. Their ranking descends from left to right. By observing Figure 4.13a, it can be noticed that the importance of the features "peak frequency" and "rise time" are significantly higher than the rest. Those two features have a major impact on the source localization results. Features "average frequency", "ASL" and "reverberation frequency hold the lowest importance, meaning their impact on the results is limited. Deleting them will not have a significant influence on localization performance.

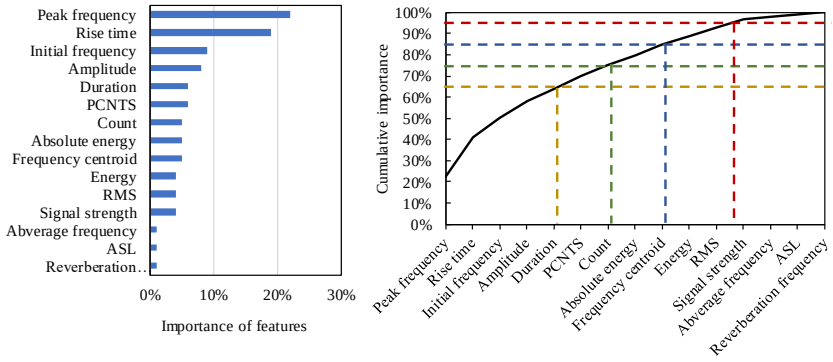

(a) (b)

Figure 4.13 Importance of features: (a) the ranking; (b) cumulative importance

The appropriate features can be selected from the feature set by the guidance of the ranking of feature importance when the input has a large dimension. Deleting the features with low importance can reduce the computing time and may increase the classification accuracy. In this paper, features were selected based on the cumulative importance of features. The cumulative importance can be obtained by the calculation of one-by-one accumulation by the sequencing of importance, which can be observed in Figure 4.13a. The features that have 65%, 75%, 85%, and 95% cumulative importance were respectively selected. The cumulative importance of features was calculated and

shown in Figure 4.13b. Four subsets were extracted from the feature-based dataset based on the cumulative importance of features: Subset 1 consists of "peak frequency", "rise time", "initial frequency", "amplitude" and "duration". The sum of the important percentage of the features in this subset is 65%. Subset 2 which in consist of "peak frequency", "rise time", "initial frequency", "amplitude", "duration", "PCNTS" and "counts". The sum of the importance percentage is 75%. Subset 3 which in consist of "peak frequency", "rise time", "initial frequency", "amplitude", "duration", "PCNTS", "counts", "absolute energy" and "frequency centroid". The sum of the importance percentage is 85%. Subset 4 which in consist of "peak frequency", "rise time", "initial frequency", "amplitude", "duration", "PCNTS", "counts", "absolute energy", "frequency centroid", "energy" and "RMS". The sum of the important percentage of the features in this subset is 95%. The accuracies and computing times of the random forest models attained by inputting the four subsets are plotted in Figure 4.14. The accuracy increased as low importance features were deleted. The total time required for training and testing reduces with the deletion of these features. The maximum accuracy (91.5%) was observed when the subset with 75% of the cumulative importance was utilized as the input; meanwhile, the total computing time was 2.98 seconds, in which the training required 2.97 seconds and the testing required 0.01 seconds. Comparing with the case using the original feature-based dataset, the accuracy increased from 90.5% to 91.5%, training time was reduced from 4.03 seconds to 2.97 seconds, and testing time was reduced from 0.02 seconds to 0.01seconds. This indicates the accuracy and computing time can be optimized by using the subset with 75% of cumulative importance. Therefore, the random forest model which utilized the subset consisting of "peak frequency", "rise

time", "initial frequency", "amplitude", "duration", "PCNTS" and "counts" is preferred and compared with ANN and stacked autoencoders in Section 5.4.

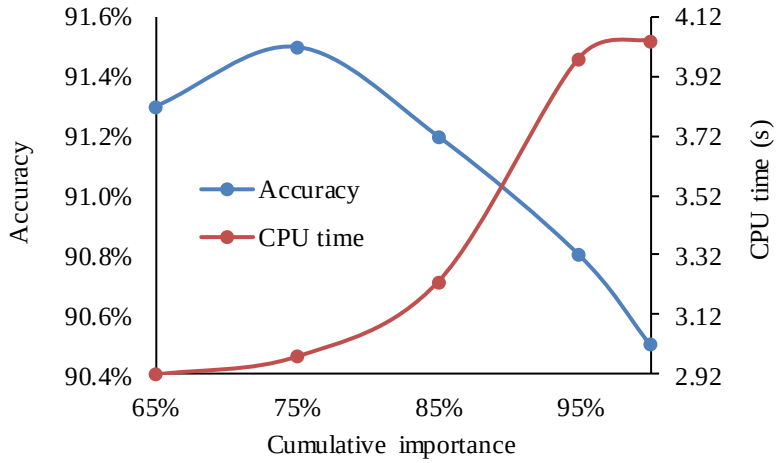

Figure 4.14 Accuracies and computing times of random forest using inputs with different cumulative importance

4.6.3 Source localization using SAE

The waveform-based AE dataset was utilized for training and testing the performance of the source localization approach using the stacked autoencoder. In this paper, the data acquisition system was set to record 2 million AE samples per second. The recording duration of an AE event was 1 microsecond. Therefore, every wave-based signal in the dataset contains 2,000 sample points. The stacked autoencoder in this paper is composed of two autoencoders. The first autoencoder will extract features from the 2,000 input sample points, compress them into the first feature set of 100 sample points, and then reconstruct the 2,000 input points. The second autoencoder takes the first feature set as an input and compresses it into the second feature set of 50 sample points, and then the autoencoder reconstructs the 100 input points. By comparing the data before and after reconstruction, the feature extraction effect of the autoencoder can be evaluated. Figures 15 show the input data and their reconstructions of randomly selected data from the

waveform-based AE dataset. Figure 4.15a shows the input data with 2,000 sample points entering the first autoencoder and the reconstructed data. Figure 4.15b shows input data with 100 sample points and data reconstructed by the second autoencoder. It can be observed from the figure that the reconstructed data is very similar to their input. They have similar data distribution patterns. This indicates that the two autoencoders can successfully reconstruct their input. Figure 4.16 shows the original input data, and the feature sets extracted by the first and the second autoencoders. In the end, the input waveform-based AE data with 2,000 sample points was compressed to the feature set with 50 sample points, and most of the effective information was saved in the feature set. The condensed feature set was employed by a softmax layer for classification.

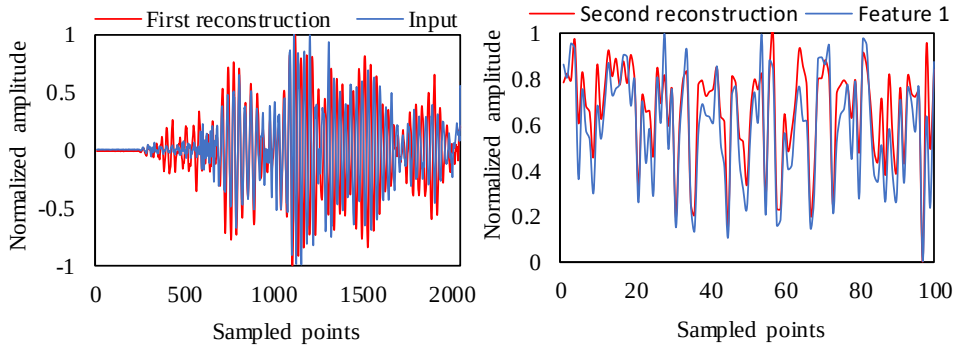

(a) (b)

Figure 4.15 The input and reconstruction patterns of autoencoders: (a) the first autoencoder; (b) the second autoencoder

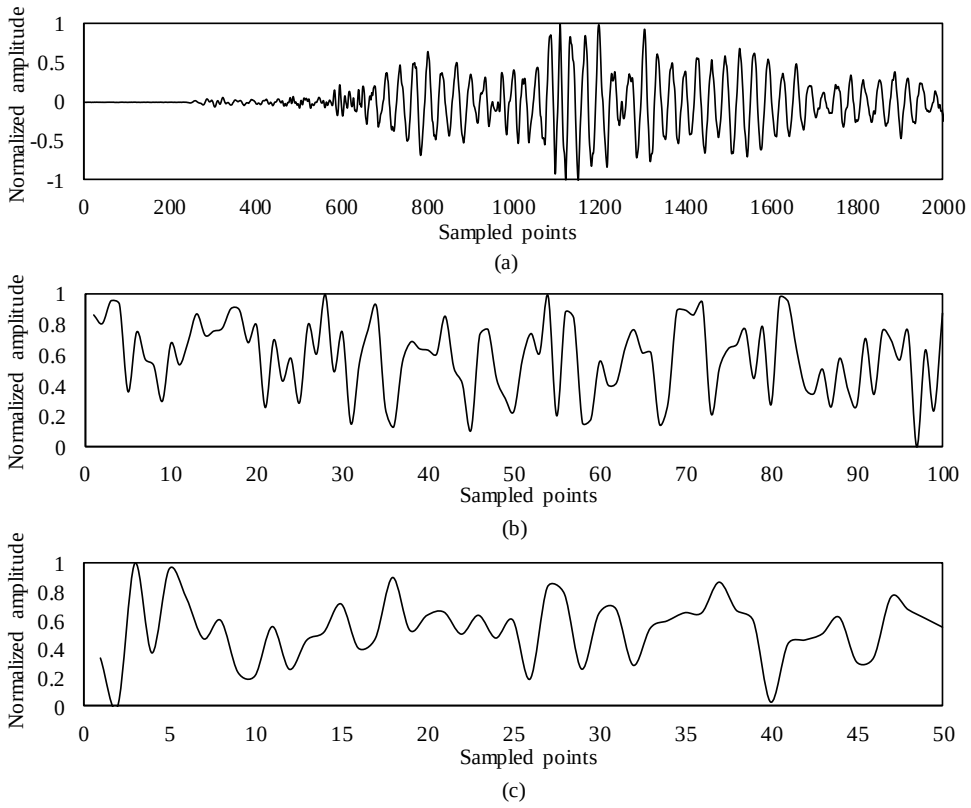

Figure 4.16. Patterns of the input waveform and extracted features: (a) input waveform; (b) the first compressed feature set; (c) the second compressed feature set

The data used for the training of this network contained 2,700 waveform-based AE signals randomly selected from all 4,050 data. The remaining 1,350 signals were utilized for testing. Figure 4.17a shows the source localization results given by the stacked autoencoder. The network can correctly localize 1,320 AE signals to their corresponding zone. The overall accuracy is 97.8%. To be more specific, the number of the AE data that were correctly localized in the corresponding zones is respectively 266 in zone 1, 264 in zone 2, 264 in zone 3, 258 in zone 4, 264 in zone 5. The precision, recall, and F1 for each zone are shown in Figure 4.17b. From zone 1 to 5. Precisions of the five class are respectively 98.5%, 98.5%, 96.7%, 97.3%, 96.4%. Recalls of the five class are respectively 98.5%, 97.8%, 97.8%, 95.6%, 97.8%. F1 of the five class are respectively 98.5%, 98.1%, 97.2%, 96.4%, 97.1%.

The computing time for the training process on an intel i-7 four-core CPU was 352.89 seconds. The computing time for testing was 0.04 seconds.

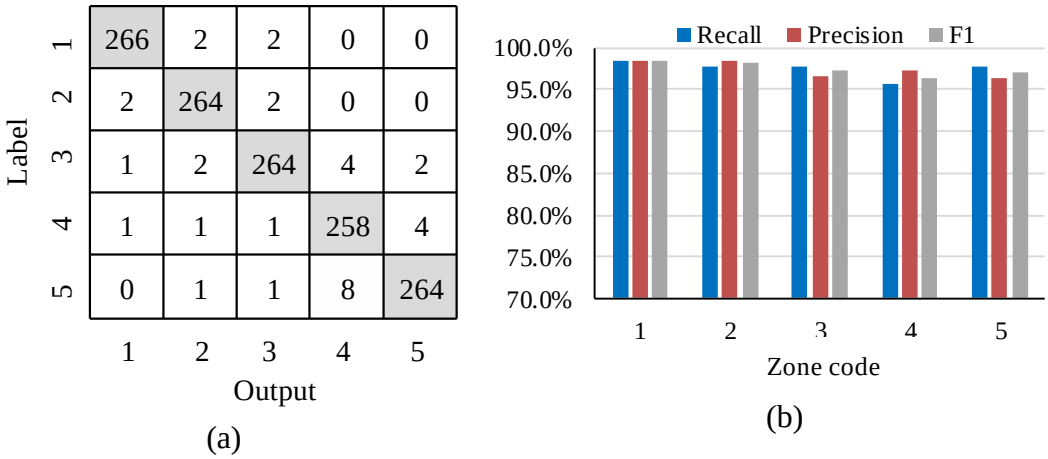

Figure 4.17. Performance of classification using SAE: (a) confusion matrix; (b) evaluation of each zone

4.7 Discussion

The accuracies and computing times of the localization approaches using three different machine learning algorithms are provided in Table 4.4. The approach using stacked autoencoders gives the highest accuracy (97.8%), which is much higher than the accuracy obtained by ANN (80.0%), and the accuracy given by random forest is acceptable (91.5%). This is because, deep learning algorithm such as stacked autoencoders automatically extracts the features that are most sensitive to the labels, however, the features input to ANN, and random forest are extracted manually from the AE signals and there may be several useful features that are not extracted as input. The training time of stacked autoencoders (352.89 seconds) is significantly more than ANN (7.96 seconds) and random forest (2.97 seconds), while the time for the trained machine learning models to run the testing processes don't show a wide variety. A testing time for stacked autoencoders, ANN, and the random forest is respectively 0.04 seconds, 0.02 seconds, and 0.01 seconds.

Table 4.4 Accuracies and computing times of three algorithms

Machine learning algorithm	Accuracy	Training time (s)	Testing time (s)
ANN	80.0%	7.96	0.02
Random forest (75% cumulative importance)	91.5%	2.97	0.01
Stacked autoencoders	97.8%	352.89	0.04

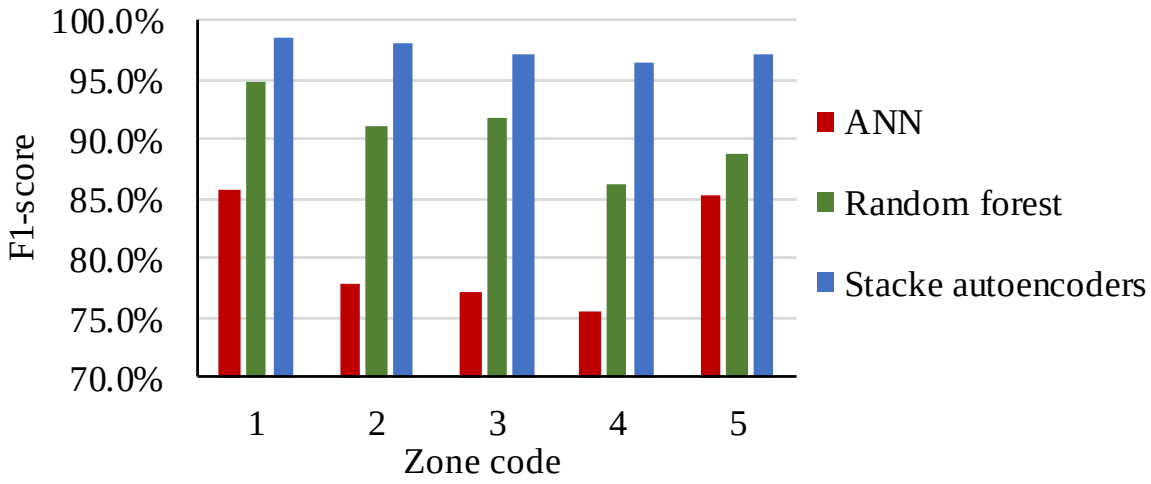

Figure 4.18 Comparison of F1-scores

The F1-scores obtained by three different algorithms are shown in Figure 4.18. It can be observed that the F1 scores of five zones obtained by random forest and stacked autoencoders are relatively stable while the F1-scores obtained by ANN show a big variety in different zones. Moreover, the F1-scores of stacked autoencoders are generally the highest of the three. This means the stacked autoencoder has the best performance for localization in each zone.

To summarize, the source localization approach using stacked autoencoders has the best accuracy but the largest training time, while the testing times do not differ much by using models being trained. If there is no minimum requirement for training time, the source localization approach using stacked autoencoders is the most desirable. The

approach using random forest is slightly worse than using stacked autoencoders but much better than using ANN. The approach using random forest is supposed to be an acceptable choice in the case that waveforms are not available and only AE parametric features can be provided.

4.8 Conclusions

This paper considered three machine learning approaches to localize simulated SCC AE sources on a 304 stainless steel specimen, which has a similar length and thickness with the realistic DCSS canister. ANN, random forest, and stacked autoencoders were used. This study aims to detect and localize AE sources with only one sensor attached opposite the source. To collect a sufficient number of AE data for training and testing, AE sources were simulated on the specimen by conducting Hsu-Nielsen pencil lead break tests. The main conclusions are as follows:

The performance of three machine learning approaches was compared. The stacked autoencoders have the best performance (97.8% accuracy versus 91.5% and 80.0%). Although the training time required for stacked autoencoders is more than the other two (352.89 seconds versus 0.02 seconds and 0.01second), their computing time required for testing is similar.

Feature selection can be achieved by running a random forest. The random forest model indicated that the AE parametric features "peak frequency", "rise time", "initial frequency", "amplitude", "duration", "PCNTS" and "counts" made up 75% of the cumulative importance for all 15 features. Using them as the input for random forest leads to increasing accuracy and decreasing computational time.

The F1-scores indicated that the performance of stacked autoencoders in various zones is the best among the three. Moreover, good performance in terms of stability in various zones was observed in stacked autoencoders while ANN resulted in more variability.

4.9 Acknowledgment

This paper was partially supported by Electric Power Research Institute (EPRI) under project number 1-108781.

4.10 References

[1] Y. Xie, J. Zhang,2015. Chloride-induced stress corrosion cracking of used nuclear fuel welded stainless steel canisters: A review, Journal of Nuclear Materials 466 85-93.

[2] J.W. Hill, Acoustic Emission Detection in 304H Stainless Steel due to Intergranular Stress Corrosion Cracking, University of South Carolina, 2018.

[3] H. Yeom, T. Dabney, N. Pocquette, K. Ross, F.E. Pfefferkorn, K. Sridharan,2020. Cold spray deposition of 304L stainless steel to mitigate chloride-induced stress corrosion cracking in canisters for used nuclear fuel storage, Journal of Nuclear Materials 538 152254.

[4] X. Wu,2020. On residual stress analysis and microstructural evolution for stainless steel type 304 spent nuclear fuel canisters weld joint: Numerical and experimental studies, Journal of Nuclear Materials 534 152131.

[5] X. Li,2002. A brief review: acoustic emission method for tool wear monitoring during turning, International Journal of Machine Tools and Manufacture 42 157-165.

[6] K. Ono,2011. Application of acoustic emission for structure diagnosis, Diagnostyka 3-18.

[7] R. Anay, V. Soltangharaei, L. Assi, T. DeVol, P. Ziehl,2018. Identification of damage mechanisms in cement paste based on acoustic emission, Construction and Building Materials 164 286-296.

[8] V. Soltangharaei, R. Anay, N.W. Hayes, L. Assi, Y. Le Pape, Z.J. Ma, P. Ziehl,2018. Damage mechanism evaluation of large-scale concrete structures affected by alkali-silica reaction using acoustic emission, Applied Sciences 8 2148.

[9] D. Li, K.S.C. Kuang, C.G. Koh,2018. Rail crack monitoring based on Tsallis synchrosqueezed wavelet entropy of acoustic emission signals: A field study, Structural Health Monitoring 17 1410-1424.

[10] L. Ai, B. Greer, J. Hill, V. Soltangharaei, R.A.P. Ziehl, Finite element modeling of acoustic emission in dry cask storage systems generated by cosine bell sources, AIP Publishing LLC, 2019, 130001.

[11] L. Ai, V. Soltangharaei, R. Anay, M.J. van Tooren, P. Ziehl, Data-driven source localization of impact on aircraft control surfaces, IEEE, 2020, 1-10.

[12] V. Soltangharaei, R. Anay, L. Ai, E.R. Giannini, J. Zhu, P. Ziehl,2020. Temporal evaluation of ASR cracking in concrete specimens using acoustic emission, Journal of Materials in Civil Engineering 32 04020285.

[13] D. Li, Y. Wang, W.-J. Yan, W.-X. Ren,2020. Acoustic emission wave classification for rail crack monitoring based on synchrosqueezed wavelet

transform and multi-branch convolutional neural network, Structural Health Monitoring 1475921720922797.

[14] R. Anay, A. Lane, D.V. Jáuregui, B.D. Weldon, V. Soltangharaei, P. Ziehl,2020. On-Site Acoustic-Emission Monitoring for a Prestressed Concrete BT-54 AASHTO Girder Bridge, Journal of Performance of Constructed Facilities 34 04020034.

[15] S. Wang, Y. Liu, H. Zhou, Y. Zhang, Z. Wu, Q. Yang,2019. Experimental study on failure process of arch dam based on acoustic emission technique, Engineering Failure Analysis 97 128-144.

[16] T. Nozawa, K. Ozawa, Y. Asakura, A. Kohyama, H. Tanigawa,2014. Evaluation of damage accumulation behavior and strength anisotropy of NITE SiC/SiC composites by acoustic emission, digital image correlation and electrical resistivity monitoring, Journal of nuclear materials 455 549-553.

[17] P. Véronique, S. Eric, G. François, K. Jean, R. François, C. Michel,2015. In situ high temperature oxidation analysis of Zircaloy-4 using acoustic emission coupled with thermogravimetry, Journal of Nuclear Materials 461 365-375.

[18] S.H. Baek, H.-S. Shim, J.G. Kim, D.H. Hur,2018. Visualization and acoustic emission monitoring of nucleate boiling on rough and smooth fuel cladding surfaces at atmospheric pressure, Nuclear Engineering and Design 330 429-436.

[19] V. Soltangharaei, J. Hill, L. Ai, R. Anay, B. Greer, M. Bayat, P. Ziehl,2020. Acoustic emission technique to identify stress corrosion cracking damage, Structural Engineering and Mechanics 75 723-736.

[20] I.A. Basheer, M. Hajmeer,2000. Artificial neural networks: fundamentals, computing, design, and application, Journal of microbiological methods 43 3-31.

[21] V. Soltangharaei, R. Anay, D. Begrajka, M. Bijman, M.K. ElBatanouny, P. Ziehl, M.J. Van Tooren, A minimally invasive impact event detection system for aircraft movables, 2019, 1268.

[22] Y. Bengio, P. Simard, P. Frasconi,1994. Learning long-term dependencies with gradient descent is difficult, IEEE transactions on neural networks 5 157-166.

[23] L. Breiman,2001. Random forests, Machine learning 45 5-32.

[24] M. Cerrada, G. Zurita, D. Cabrera, R.-V. Sánchez, M. Artés, C. Li,2016. Fault diagnosis in spur gears based on genetic algorithm and random forest, Mechanical Systems and Signal Processing 70 87-103.

[25] R.K. Patel, V. Giri,2016. Feature selection and classification of mechanical fault of an induction motor using random forest classifier, Perspectives in Science 8 334-337.

[26] Y. Bengio, P. Lamblin, D. Popovici, H. Larochelle, Greedy layer-wise training of deep networks, 2007, 153-160.

[27] I. Arel, D.C. Rose, T.P. Karnowski,2010. Deep machine learning-a new frontier in artificial intelligence research [research frontier], IEEE computational intelligence magazine 5 13-18.

[28] P. Karvelis, G. Georgoulas, V. Kappatos, C. Stylios,2021. Deep machine learning for structural health monitoring on ship hulls using acoustic emission method, Ships and Offshore Structures 16 440-448.

[29] H. Wadley, R. Mehrabian,1984. Acoustic emission for materials processing: a review, Materials Science and Engineering 65 245-263.

[30] C.U. Grosse, M. Ohtsu, Acoustic emission testing, Springer Science & Business Media, 2008.

[31] C.B. Scruby,1987. An introduction to acoustic emission, Journal of Physics E: Scientific Instruments 20 946.

[32] T. Boczar, M. Lorenc,2004. Determining the repeatability of acoustic emission generated by the Hsu-Nielsen calibrating source, Molecular and quantum Acoustics 25 177-192.

[33] A. Laksimi, S. Benmedakhene, L. Bounouas, Monitoring acoustic emission during tensile loading of thermoplastic composites materials, 1999.

[34] S.M. Ali, K. Hui, L. Hee, M.S. Leong, A.M. Abdelrhman, M.A. Al-Obaidi,2019. Observations of changes in acoustic emission parameters for varying corrosion defect in reciprocating compressor valves, Ain Shams Engineering Journal 10 253-265.

[35] T. Jayalakshmi, A. Santhakumaran,2011. Statistical normalization and back propagation for classification, International Journal of Computer Theory and Engineering 3 1793-8201.

[36] M.H. Hassoun, Fundamentals of artificial neural networks, MIT press, 1995.

[37] R. Sun, Y. Chen, A. Dubey, P. Pugliese,2021. Hybrid electric buses fuel consumption prediction based on real-world driving data, Transportation Research Part D: Transport and Environment 91 102637.

[38] L.L. Rogers, F.U. Dowla,1994. Optimization of groundwater remediation using artificial neural networks with parallel solute transport modeling, Water Resources Research 30 457-481.

[39] A. Liaw, M. Wiener,2002. Classification and regression by randomForest, R news 2 18-22.

[40] J.R. Quinlan, C4. 5: programs for machine learning, Elsevier, 2014.

[41] S. Sathyadevan, R.R. Nair, in, Computational intelligence in data mining-volume 1, Springer, 2015, pp. 549-562.

[42] L. Rutkowski, M. Jaworski, L. Pietruczuk, P. Duda,2014. The CART decision tree for mining data streams, Information Sciences 266 1-15.

[43] R. Genuer, J.-M. Poggi, C. Tuleau-Malot,2010. Variable selection using random forests, Pattern recognition letters 31 2225-2236.

[44] B.H. Menze, B.M. Kelm, R. Masuch, U. Himmelreich, P. Bachert, W. Petrich, F.A. Hamprecht,2009. A comparison of random forest and its Gini importance with standard chemometric methods for the feature selection and classification of spectral data, BMC bioinformatics 10 1-16.

[45] A. Ng,2011. Sparse autoencoder, CS294A Lecture notes 72 1-19.

[46] S. Tao, T. Zhang, J. Yang, X. Wang, W. Lu, Bearing fault diagnosis method based on stacked autoencoder and softmax regression, IEEE, 2015, 6331-6335.

[47] F. Guo, Y. Qian, Y. Wu, Z. Leng, H. Yu,2021. Automatic railroad track components inspection using real‐time instance segmentation, Computer‐Aided Civil and Infrastructure Engineering 36 362-377.

[48] M. Buckland, F. Gey,1994. The relationship between recall and precision, Journal of the American society for information science 45 12-19.

[49] L. Zhong, L. Hu, H. Zhou,2019. Deep learning based multi-temporal crop classification, Remote sensing of environment 221 430-443.

Chapter 5

Evaluation of ASR in Concrete Using Acoustic Emission and Deep Learning[1]

[1] Li Ai, Vafa Soltangharaei, and Paul Ziehl. (2021) Evaluation of ASR in Concrete Using Acoustic Emission and Deep Learning. *Nuclear Engineering and Design*, 380, 1110.

5.1 Abstract

Alkali-silica reaction (ASR) is one of the main damages causes in concrete structures such as nuclear power plants which may endanger their serviceability and integrity. Acoustic emission (AE) is a passive nondestructive method for structural health monitoring. It is very sensitive and has the capability of monitoring structures continuously. This method may be an alternative for early damage detection in concrete nuclear structures affected by ASR. The innovation of this paper lies in the implementation of deep learning algorithms to evaluate the ASR progress. ASR was monitored by AE in a concrete specimen, which was cast with reactive coarse aggregates and reinforced by steel rebars. The AE signals recorded during the experiment were filtered and divided into two classes. Two deep learning algorithms of convolutional neural network (CNN) and stacked autoencoder were employed to classify the AE signals into the corresponding classes. The model based on CNN resulted in a classifier with higher accuracy than the model based on the autoencoder network.

Keywords: Acoustic emission; Alkali silica reaction; Continuous wavelet transform Convolutional neural network; Stacked autoencoder

5.2 Introduction

Concrete is one of the important infrastructure materials which is wildly applied in civil engineering structures. However, the brittle mechanical property of concrete makes it vulnerable to cracking. ASR is one of the main sources of cracking in concrete structures. ASR is a chemical reaction between silica in reactive aggregate and alkaline ions in cement. The product of this reaction is a hygroscopic gel, which absorbs humidity and expands [1]. The gel exerts pressure on the aggregate and cement matrix and causes

cracking. The common structures, which are exposed to ASR are bridges [2-5], concrete dams [6; 7], nuclear power plants, and nuclear waste containments [8-11]. Because of the safety and radioprotection functions of concrete structures in nuclear power plant, the effects of ASR to current and long-term operations must be thoroughly addressed.

Many approaches were applied to monitor ASR damage and evaluate its effect on structures. The conventional approaches include regular-base visual inspection, coring and petrographic analysis, demountable mechanical strain gauge (DEMEC gauge), relative humidity or moisture content measurement, and crack indexing. These approaches have several disadvantages. For example, visual inspection is usually not effective for the early detection of ASR damage. Generally, due to in-plane constraints of structures, the surface cracks appear in a late stage of ASR process, and the visual inspection of large-scale structures is time-consuming and prone to human error [12]. Coring and petrographic analyses are destructive methods that are generally not suitable for sensitive structures such as nuclear power plants. Furthermore, it is difficult to evaluate the condition of entire structure with only a few cores or samples.

AE can be an alternative for the temporal evaluation of ASR damage in concrete structures used in nuclear facilities. This method is sensitive and has a continuous monitoring capability [13-19]. Recently, there have been several investigations conducted where AE was applied for the detection of damage and the quantification of the defects caused by ASR [1; 15; 20-24]. Farnam et al. [21] utilized peak frequency and frequency centroid to characterize signal signatures that emanate from cracks in aggregates and cement paste. High-frequency signals were observed in the earlier stage of ASR, while the low-frequency signals appeared later in the ASR process. X-ray images helped the

authors to verify their hypothesis. Lokajíček et al. [22] utilized both ultrasonic pulse velocity and AE to monitor the damage caused by ASR. Four specimens with different aggregate reactivities were used. The selection of the appropriate features was generally based on experience and very challenging especially for complex data sets. Therefore, an automatic approach is required to extract features directly from raw data and find potential patterns in the complex data sets. This goal can be fulfilled by using deep learning methods.

Deep learning is one of the artificial intelligent techniques that simulates information processing in the human brain [25; 26]. The advantage of deep learning is using raw data instead of extracted features as an input set. Therefore, there is no need for feature extraction and feature selection, which can be challenging for complex data sets [27]. CNN is one of the state-of-art deep learning algorithms [28-31], which develops rapidly, and is widely studied in image recognition and target detection. Redmon et al. [28] proposed Yolov3 as an improved architecture of Yolo network. This improved architecture has a higher accuracy, and training speed is acceptable. Ren et al. [29] proposed a faster R-CNN (Region-based CNN). This new target detection model proposes a Region Proposal Network (RPN) based on a Fast R-CNN, which significantly increase the efficiency of target detection. In addition to design a deeper architecture of CNN, using a hybrid method is another strategy to improve the performance of CNN [32; 33]. Niu et al. [32] presented a hybrid model based on CNN and Support Vector Machine (SVM) to recognize the handwriting digits. In the hybrid model, the convolutional layers extract features, and the SVM works as a recognizer. The results indicated that this fusion could obtain better accuracy than a single model. Kim et al. [33] proposed a hybrid model

for the prediction of residential energy consumption. The hybrid model consisted of CNN and a long short-term memory network (LSTM). The convolutional layers could extract features from complex variables that affected energy consumption. The LSTM layers were designed to model the temporal information of irregular trends in time series components. Compared with the previous work, a better performance was observed by using the proposed hybrid model.

In recent years, deep learning has been applied in AE [34-37]. Ebrahimkhanlou et al. [34] worked on a deep learning framework based on a stacked autoencoder network to locate AE events on the metal structures. Li et al. [35] utilized a convolutional neural network for AE wave classification to obtain a more accurate and comprehensive rail crack monitoring in the field with complex cracking conditions, high-operational noise, and large data. Shevchik et al. [36] proposed an on-site quality monitoring system for additive manufacturing by utilizing AE and a spectral convolutional neural network. Ai et al. [37] developed a passive nondestructive health monitoring system to locate impacts on an aircraft component based on AE and deep learning. An autoencoder algorithm was trained by the data and utilized as a part of the health monitoring system.

The main focus of this paper is to relate AE data collected during ASR process and attribute them to ASR expansion strains. CNN and autoencoder networks were used to develop data-driven models and relate raw data to classes, which were corresponding to strain ranges. Using this method, sensitive structures such as nuclear power plants or waste containments can be continuously monitored for ASR cracking without interrupting the structural serviceability and destructing the structures. Furthermore, ASR process phases can be determined using a developed data-driven model. The authors are

currently not aware of any published similar works that implement a deep learning algorithm to relate AE data to ASR expansion strains.

5.3 Test setup and experimental procedure

A concrete block specimen with the dimensions of the 305 mm × 305 mm × 1120 mm was prepared for ASR testing. The specimen was cast with reactive coarse aggregates and reinforced by steel rebars. The geometric of the specimen is shown in Figure 5.1a. The details of the reinforcements are presented in Figure 5.1b. The specimen had four longitudinal US #7 steel rebars and transversal US #6 steel rebars with 150 mm spacing. All rebars were T-headed to compensate for the short development length.

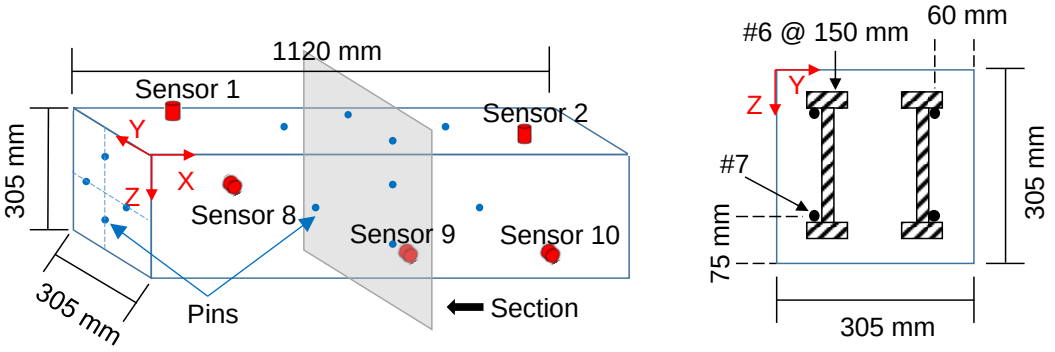

(a) Concrete specimen

(b) Reinforcement detail

Figure 5.1 Structural details of specimen

Ten AE sensors were attached to the surfaces of the specimen using grey double/bubble epoxy. The sensor layout is presented in Fig. 1a [15]. Three sensors (sensor 8-10) were attached to the front longitudinal side surface. Three sensors (sensor 5-7) were attached on the back longitudinal side surface. Two sensors (sensor 1-2) were attached on the top, while sensor 3-4 were attached to the bottom surface. The sensors were PKWDI with an operating frequency of 200-850 kHz. AE signals were acquired by

a 24-channel Micro-II Express data acquisition system manufactured by MISTRAS Group, Inc. (Princeton Junction, NJ, USA). The sampling rate was set to 5 MHz.

A chamber with the dimensions of 243 cm (width) × 243 cm (length) × 122 cm (height) was designed and built to accelerate the ASR process by providing high temperature and humidity. The temperature inside the chamber was kept at 37 ± 3 ^{o}C. The humidity was kept around 95% ± 5%. The specimen was placed on a steel carrier with wheels, which was designed and fabricated as the support of the specimen. DEMEC gauges were used for the expansion measurement by measuring the distance between pins (Fig. 1a) along three dimensions. The expansion was measured regularly every month, and the maintenance of AE sensors was conducted at the same time to ensure the bonding status between sensors and specimen. More details about the test setup and procedures can be found in [15].

5.4 Analysis procedure

In this paper, two methods based on deep learning were proposed to evaluate ASR in concrete. One is based on continuous wavelet transforms (CWT) and CNN. The other one is based on a stacked autoencoder network. The AE signals are divided into two subsets according to the temporal evolution of signal features. Each subset of data can be attributed to an ASR expansion range. The data-driven models are developed using CNNs and stacked autoencoders to attribute the AE signals to the corresponding subsets.

5.4.1 Continuous wavelets transform

CWT is a joint time-frequency analysis method that captures the time-frequency characteristics in non-stationary signals such as AE signals [38]. CWT has a good performance in signal processing in terms of both time and frequency [39]. The

continuous wavelet coefficients can be expressed by a scalogram image. The 2D scalogram images are the input for CNN models. In this paper, the Morse wavelet is selected as the mother wavelet function to conduct CWT. The Fourier transform of Morse wavelet is presented in Eq (5.1):

$$\Psi_{p,\gamma}(x) = U(x)\alpha_{p,\gamma}x^{\frac{p^2}{\gamma}}e^{-x^{\gamma}} \tag{5.1}$$

where $U(x)$refers to the unit step, $\alpha_{p,\gamma}$ refers to the normalizing constant, p^2 refers to the time-bandwidth product. γ is the parameter that characterizes the symmetry of the Morse wavelet [40]. In this paper, p^2 and γ was defined as 60 and 3.

5.4.2 Convolutional neural network

CNN is a deep neural network with convolutional filters [41]. CNN is generally composed of three main parts: an input layer, feature extraction layers, and a fully connected layer. The core part of the feature extraction layers mainly includes convolutional layers and pooling layers. The architecture of a typical CNN with two convolutional layers and two pooling layers is shown in Figure 5.2.

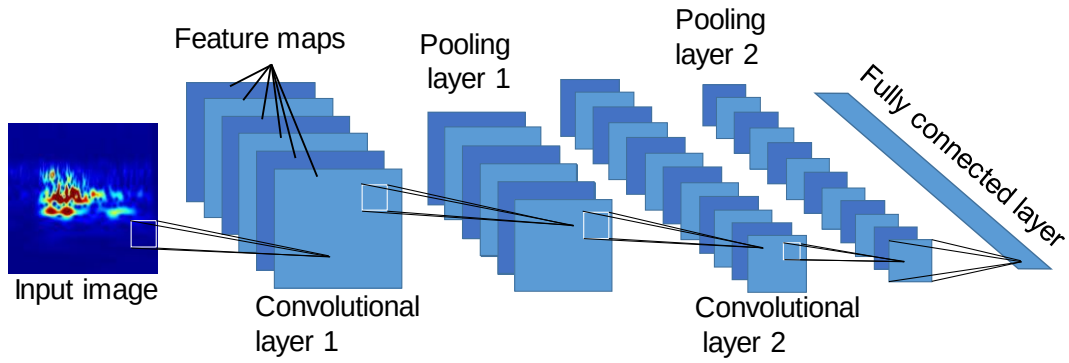

Figure 5.2 Architecture of a typical CNN

In the convolutional layer, multiple convolutional kernels are employed to filter the input and generate feature maps. The pooling layer is used for the down-sampling of

feature maps obtained from the previous convolutional layer [42]. If the image feature maps are directly used for classification without any processing, a great computational complexity will be generated, and the model is prone to overfitting. Therefore, a further reduction in the dimensionality of feature maps is required, which is the reason to construct the pooling layer after each convolutional layer. The fully connected layer is employed at the end of the CNN model. It converts the feature maps, resulting from the previous pooling layer to one feature vector.

GoogLeNet is an architecture of CNN that developed based on the LeNet model [43]. The number of layers is extended up to 22. The GoogLeNet model is pre-trained by more than a million images from a subset of ImageNet database [44]. GoogLeNet has been reported to have a good performance for the identification of acoustic emission signals in the scenarios such as the monitoring of wear in sliding bearing system [45; 46] and the monitoring of stay cable in a bridge [47]. Therefore, GoogLeNet was selected in this paper as a preliminary study of applying CNN to evaluate concrete ASR expansion.

In this paper, the input data is 2D wavelet images. Before input datasets, the data is labeled and normalized. The wavelet coefficients are scaled between 0 to 1.

5.4.3 Stacked autoencoder

The stacked autoencoder is also employed to classify the data, and the results are compared to CNN. The stacked autoencoder neural network is a deep neural network composed of multiple autoencoders [48]. An autoencoder is a neural network usually with three layers. The number of neurons in the input and output layers is the same. The algorithm condenses the input data according to the dimension of the hidden layer and reconstructs the output of condensed data to the output layer [49]. An objective function

is designed to minimize the error in input data and output data. The compression process of input data can be considered as the feature extraction process. In stacked multiple autoencoders, more than one autoencoder is utilized to condense the data. In other words, the data is condensed several times by multiple autoencoders. A SoftMax layer is connected to the last autoencoder to classify final compressed features. In this paper, a stacked autoencoder with two autoencoders is employed. The input data is the Fast Fourier Transforms (FFT) magnitude of the AE waveforms. In other words, the input data set includes a matrix with rows representing the number of signals and columns representing FFT magnitudes of signals. The first and second autoencoder has a size of 100 and 50 neurons, respectively. Figure 5.3 illustrates the structure of the stacked autoencoder network used in this paper.

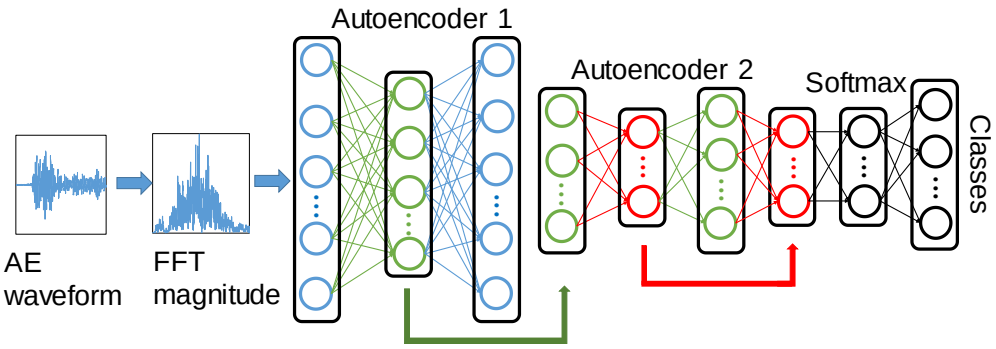

Figure 5.3 A stacked autoencoder composed of two autoencoders

5.5 Results and discussion

5.5.1 Analysis of features and class definition

The AE data acquired from the sensors during ASR have been utilized for analysis. Some sensors collected a large amount of extraneous data due to faulty connections and environmental noise. Therefore, the first step before analyzing the AE data is filtering. The noises from faulty connections have specific signal features such as

small counts, average frequency, and peak frequency. Initially, the noises related to the faulty connections were removed by deleting the data with an average frequency lower than 60 kHz. Some faulty data remained from the first stage. Therefore, another filter was applied to the contaminated channel by removing the signals with a peak frequency of less than 80 kHz. The filtering procedure mentioned above removed a large amount of faulty data. Then, a procedure was developed to further filter the data based on AE event definition. An AE event refers to a set of hits acquired by different sensors in a specific time interval, which is defined based on a stress wave velocity and specimen dimensions. Only the events which include at least four hits were considered valid data and kept, and the rest of the data was considered as noise and was therefore deleted.

Several AE features were extracted from the AE signals after filtering. Those features can be divided into non-frequency-based features and frequency-based features. The non-frequency-based features in this paper are counts, counts to peak, amplitude, rise time, duration, and signal strength. The non-frequency-based features are presented for a typical AE waveform, as shown in Figure 5.4a.

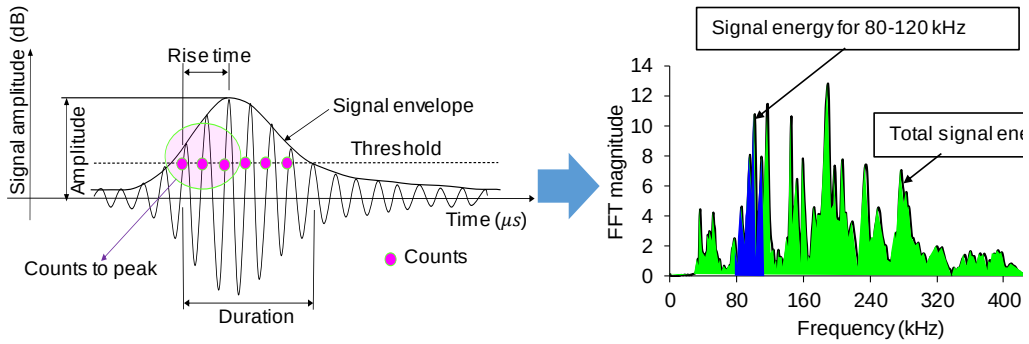

(a) Non-frequency-based feature extraction

(b) Frequency-based feature extraction for 80-120 kHz

Figure 5.4 AE features

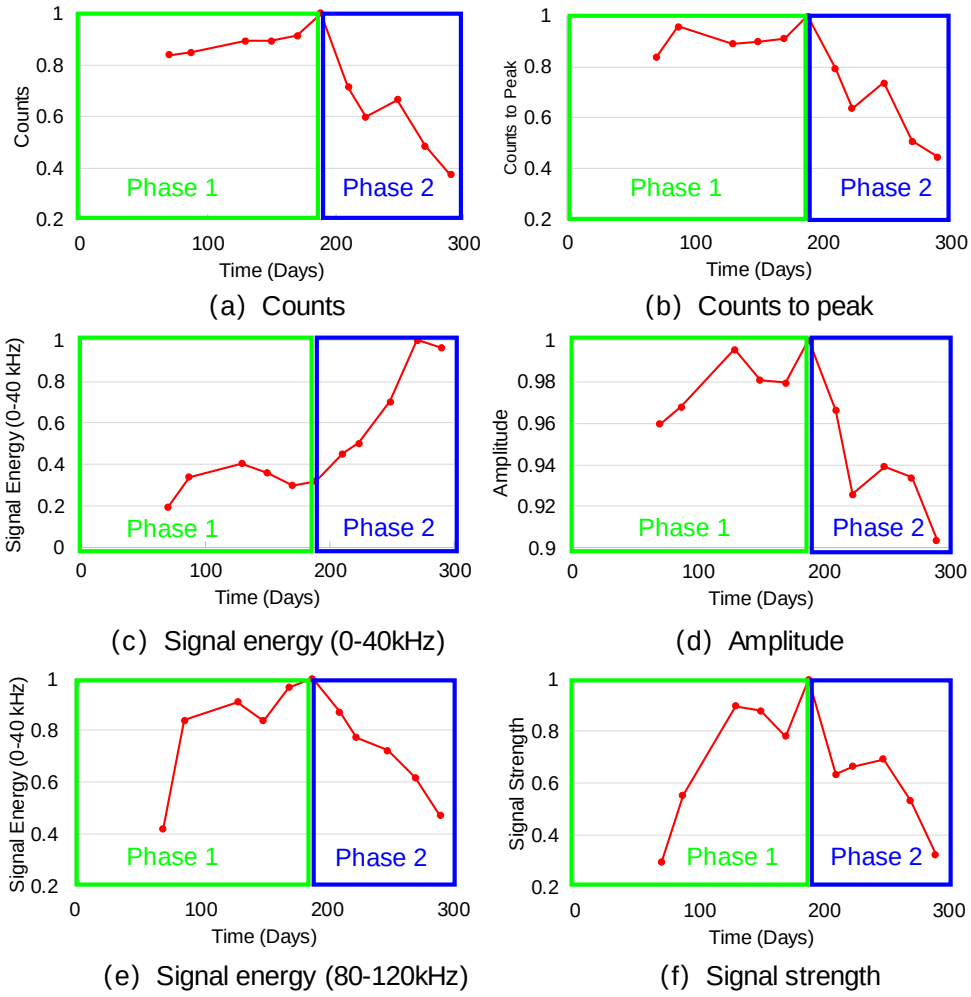

Figure 5.5 Temporal evolution of AE features during ASR process

To extract the frequency-based features, the AE signals were transferred to the frequency domain using FFT. The frequency domain of each signal was divided by ten equal intervals with a bandwidth of 40 kHz. The energies corresponding to each frequency band were derived by calculating the area under the FFT spectrum in that frequency band (Figure 5.4b). The energies in the frequency bands were normalized to the total energy of the signal, which was calculated by the area under the entire FFT spectrum (Figure 5.4b). These normalized energies for different frequency bands are

referred to as frequency-based features in this paper. Figure 5.4b shows the extraction of frequency-based features in the range of 80 -120 kHz.

The average temporal evolution of some features such as counts, counts to peak, amplitude, signal strength, signal energy for 0-40 kHz, and signal energy for 80-120 kHz are illustrated in Figure 5.5. All the features were normalized to 0-1. The features shown in Figure 5.5 indicate the change in the temporal evolution at almost the same time, around 190 to 200 days. The possible reason for the trends shown in Figure 5.4 is the dominant crack mechanisms in different ASR stages are vary. Petrographic analysis was conducted on the specimens at the end of the ASR experiment to investigate the crack mechanism inside the concrete specimen. Cross-section slices were sawn from approximately one-half of the length of the specimen. In total, fourteen 38-mm-thick cross-section slices were sawn from the specimen, with the cross-sections oriented parallel to the Y-Z plane. Each slice was further cut into quarter sections and polished for stereo-optical microscopy examinations and a manual point count procedure (MPCP). The Point count results were totaled for each slice, including the four quarter sections. The results are shown in Figure 5.6 as the weighted normalized cracking score. The details of the petrographic analysis can be found in [15].

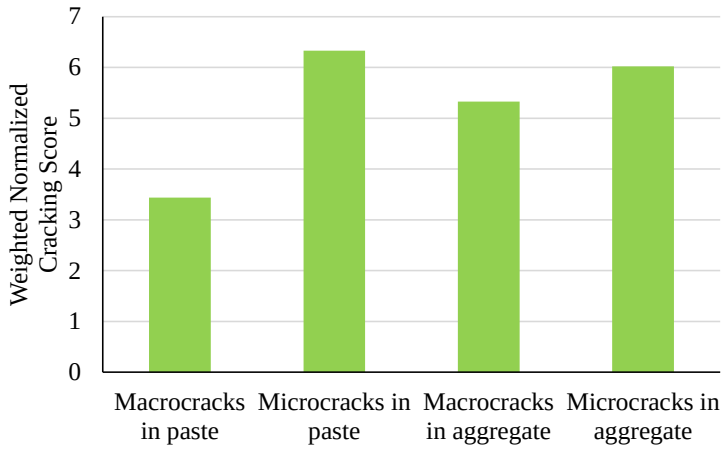

Figure 5.6 Average of weighted normalized cracking score for reactive specimens

The petrographic results indicate that microcrack and macrocrack formations are the primary damage mechanisms in the specimen. Previous research has reported that in the later stage of the ASR process, macrocrack formations and extension of the existing crack exceeded microcrack formation [15]. The energy release rate of crack propagation is changing with the size of the crack. The relationship between crack size and energy-releasing is presented in Figure 5.8. According to Griffith's crack theory, the energy-releasing reaches a peak when the crack length exceeds the critical length a_c. The energy release rate keeps decreasing with the continuous propagation of crack [50]. Therefore, in this paper, the microcrack formation in the early stage of ASR (before 190) could release more energy than the macrocrack formation in the later stage (after 190 days). And this could explain the decreasing of features such as counts, counts to peak, amplitude, and signal strength after day 190. Previous literature also indicates that AE signals with low-frequency have been attributed to crack extension, whereas AE signals with high-frequency are attributed to the initiation of small-scale cracks [51; 52]. That may be the reason for observing the decreasing of signal energy for 80-120 kHz and increasing of signal energy for 0-40 kHz after day 190.

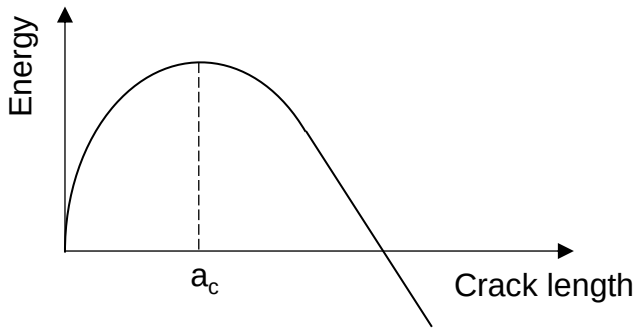

Figure 5.7 Relationship between energy and crack length

The signal amplitudes and the cumulative signal strength (CSS) for the concrete specimen are presented in Figure 5.6a. The jumps in the cumulative signal strength curve are representative of a new crack initiation event or a crack extension along an existing crack. The major jump occurs around 200 days, which coincides with the time related to change in the AE features shown in Figure 5.6. The crack width was monthly measured for the surface cracks. The maximum crack widths were not necessarily attributed to the same crack and same location during the ASR process. The maximum crack widths in terms of time are illustrated in Figure 5.6. A curve was also fitted to the crack width data, as seen in the figure. The first visual crack was observed at 146 days. The crack width grow rate increase slowly from day 146 to day 190 and then expands rapidly from day 190 through day 300. Microscopic photos of cracks at 146 and 269 days are also presented in Figure 5. 8.

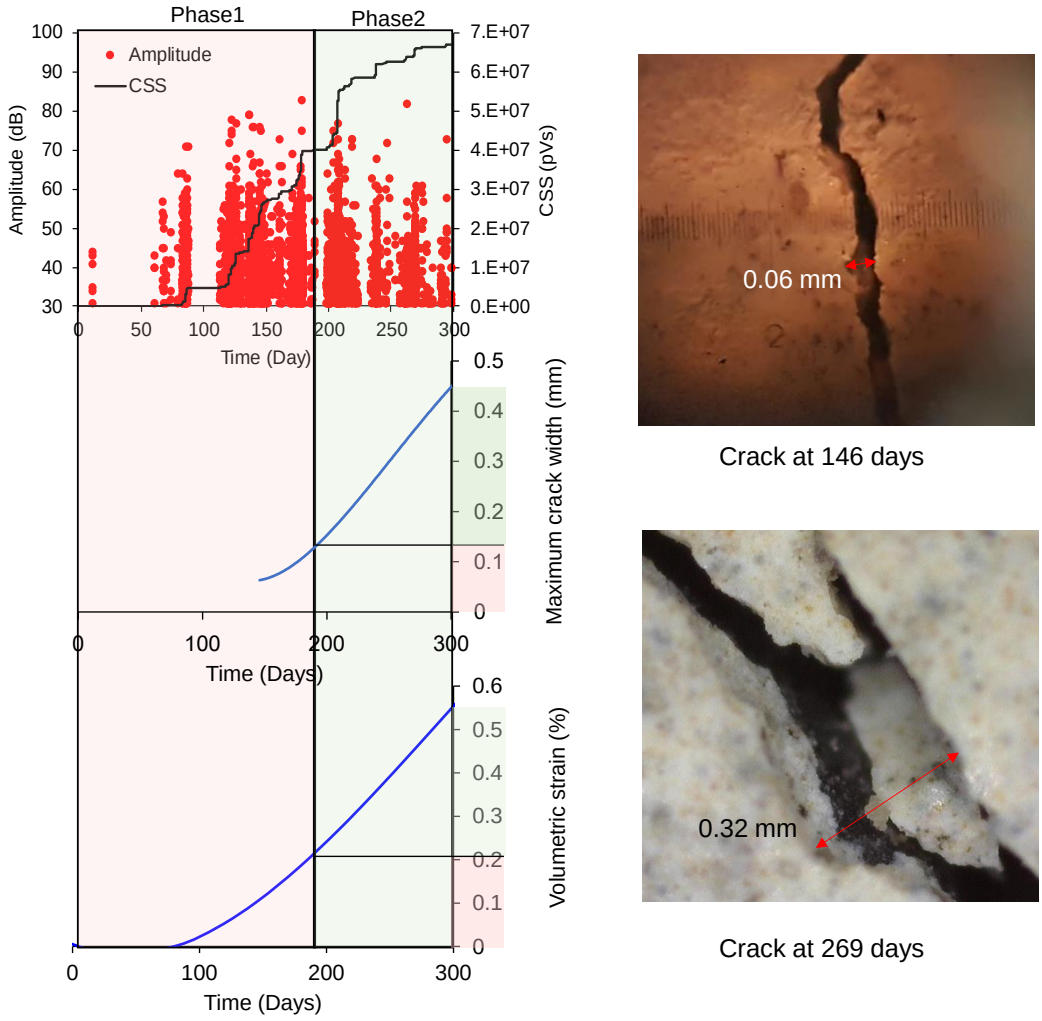

Figure 5.8 AE amplitudes, CSS and volumetric strain presentations with phases

In addition to the crack width, expansion strains were measured monthly on the specimen surfaces. The strain measurements were conducted along different dimensions on the specimen surfaces during ASR. The volumetric strain is defined as the accumulation of average strains along the X, Y, and Z axes. Results of the volumetric strain range are presented in Figure 5.8.

In this paper, the entire ASR process was divided into two phases, considering the AE features, crack widths and CSS trends. The first phase is between 1-190 days, (microcrack initiation phase). The first visible crack was observed in this phase. The

strain changed from 0.00% to 0.21% in phase 1. The days between 190 to 300 were defined as phase 2 (macrocrack extension phase), the strain changed from 0.21% to 0.55%. This paper aims to automatically classify AE signals recorded during the ASR process according to the assigned phases (phase 1 and phase 2) by using the proposed deep learning models.

5.5.2 Waveforms and CWT images

There are 1668 and 1402 AE signals in classes 1 and 2, respectively. The input set for the stacked autoencoder was FFT spectra of AE signals. The other data set was prepared by conducting CWT on the data. The coefficients of CWTs were saved as 2D contour images, and the images were utilized as an input data set for CNN. Both deep learning models (autoencoder and CNNs) classify the AE signals into the attributed classes. A time-domain waveform and its FFT spectrum are randomly selected for each class and presented in Figure 5.9. Moreover, the CWT images of the signals are presented in Figure 5.10. The amplitudes of AE waveforms were normalized to a range of -1 to 1. The frequency-domain waveforms were normalized by the maximum magnitudes, and the wavelet coefficients were scaled between 0 to 1.

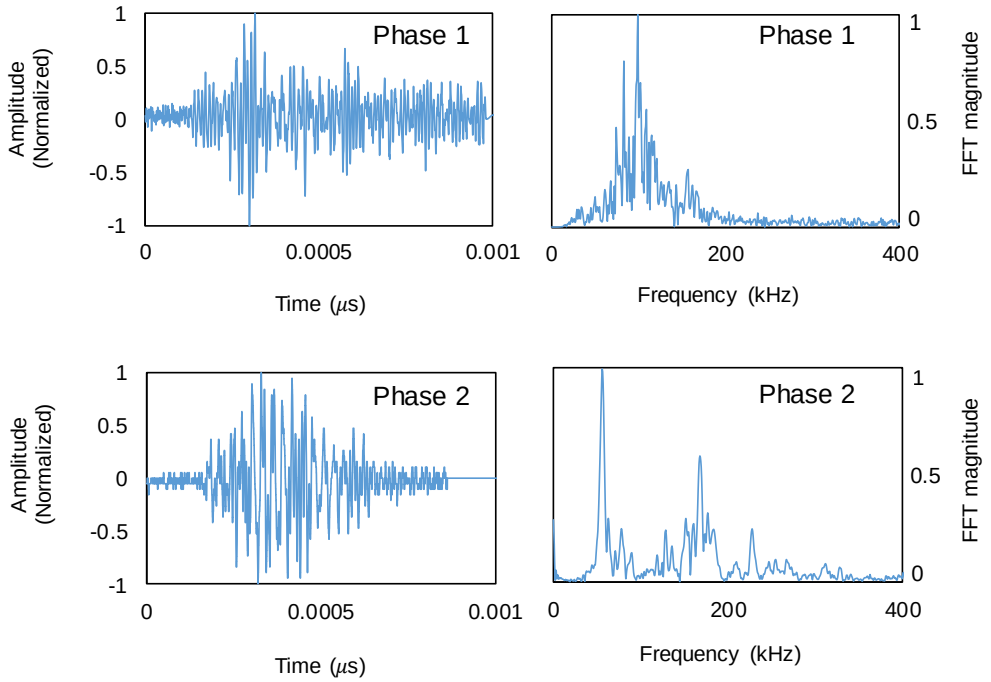

Figure 5.9 Waveforms of AE signals in Phases 1 and 2

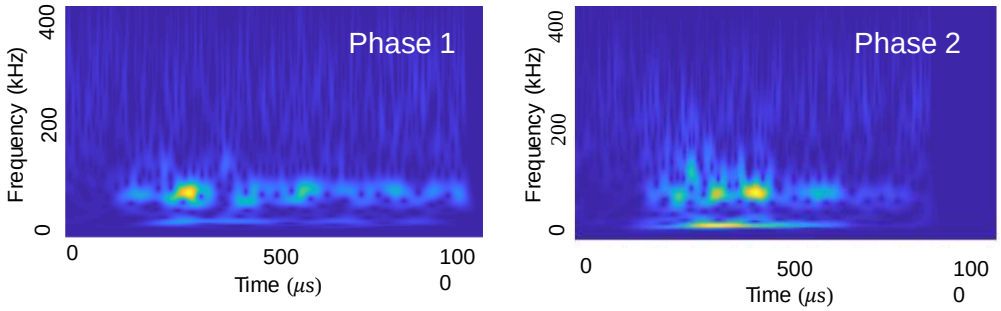

(a) Phase 1 (b) Phase 2

Figure 5.10 CWT image of AE signals in classes 1 and 2

5.5.3 *Evaluation of ASR data using CNN*

From all CWT contour images, 70% of images were randomly selected for a training set of CNN, and 30% of images were randomly selected for a validation set. The designated phases (phase 1 or 2) of the AE signals were utilized as data labels. The classification result of validation dataset is presented in the confusion matrix (Figure

5.11a). Among the CWT images in phase 1, 74.6% of images were correctly classified as phase 1, while 25.4% of images were classified as phase 2. Among the images in phase 2, 80.2% of them were correctly classified, while 19.8% of images were misclassified as phase 1. In total, 707 images were correctly classified to the corresponding phases, which was 76.7% of all images in the validation data set. In other words, the accuracy of the CNN classifier is 76.7% (Figure 5.11a). Most of the error occurred around day 190 which is the separation day of phases 1 and 2. It was challenging for the deep learning model to precisely classified the signals around day 190 because the ASR phases was manually divided, the AE signals in the boundaries of phases 1 and 2 has very similar characteristics. This problem in classification task could be solved by considering the overlap area [53]. Implementing overlap area would be the subject of future work. Some errors might subject to the condition of different AE sensors in the experiment. Although all the sensors utilized in this paper are type PKWDI, the sensitivity of the sensors may vary due to the time of use. The vary of sensors sensitivity can reflect on the AE signals, which may have some impact on the performance of the deep learning model. Another factor that might cause the error could be the bonding of sensors. The AE sensors were bonded to the concrete specimen using grey double/bubble epoxy. The bonding between the specimen and sensor tends to loose after a period of time due to the high humidity and high temperature environment. The insecure bonding of sensor could also reflect on the AE signals and influence the performance of deep learning model. To minimize the error cause by the AE bonding status, the maintenance of AE sensors was conducted monthly to ensure the bonding status between sensors and specimen.

Precision and recall are employed as parameters to evaluate the classification performance in each phase. Generally, precision can be calculated by Eq. (5.2):

$$Precision = \frac{TP}{TP+FP} \tag{5.2}$$

where, TP, is the true positive, which refers to the number of samples correctly classified to the attributed class. FP is the false positive, which refers to the number of samples that do not belong to the class and are misclassified into the class. The precisions of CNN model using all AE data for classes 1 and 2 are 85.5% and 66.8%, respectively (Figure 5.11a).

The recall parameter can be calculated as follows:

$$Recall = \frac{TP}{TP+FN} \tag{5.3}$$

where FN is the false negative, which is the number of samples that belong to a class but are misclassified as other classes. The recall parameter of the CNN model for classes 1 and 2 was calculated as 74.6% and 80.2% (Figure 5.11a).

The ~~p~~recision parameter has an inverse relationship with the recall parameter. Generally, a class with a high precision value has a low recall value and vice versa [54]. F1-score is a parameter to evaluate the efficiency of the classifier in each phase (class) by considering both recall and precision parameters. The F1-score is the harmonic mean of the precision and recall [55]. The values of the F1-score for phase 1 and phase 2 are 79.7% and 72.9%, respectively, and presented in Fig. 11b.

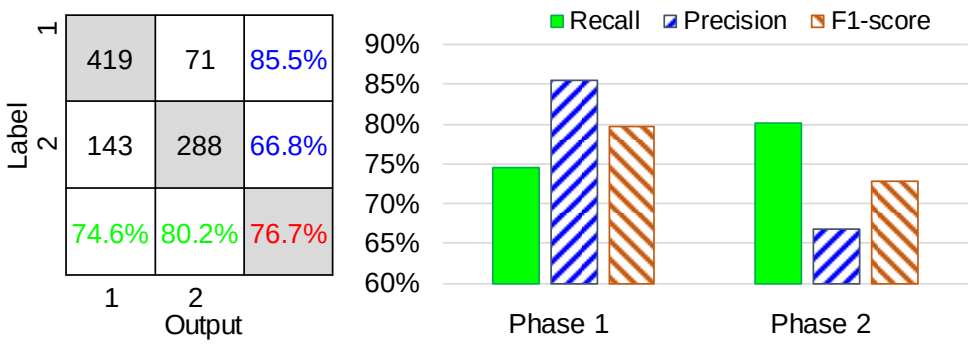

(a) Confusion matrix (b) Recall, precision, and F1-score

Figure 5.11 Performance of CNN using all AE signals

A CNN model was developed using the data from one sensor. The selected sensor (sensor 6) had the largest number of AE signals (421) among all sensors. AE signals were transferred to CWT images. Among all images, 70% of the data were randomly selected for the training set, and the rest (30%) were employed for the validation set. The result of the CNN model is presented in Fig. 12a. Among the images in phase 1, 85.5% of images were correctly classified as phase 1, and 14.5% of images were misclassified as phase 2. Among the images in phase 2, 86.0% of images in phase 2 were successfully classified, and 14.0% of images were erroneously assigned to phase 1. The total accuracy of the model is 85.7% (Figure 5.12a). The precisions of phases 1 and 2 are 90.2% and 79.6%, respectively (Figure 5.12a). The recall parameters for phases 1 and 2 are 85.5% and 86.0%, respectively (Figure 5.12a). The F1-score for phases 1 and 2 are 87.8% and 82.7%, respectively (Figure 5.12b).

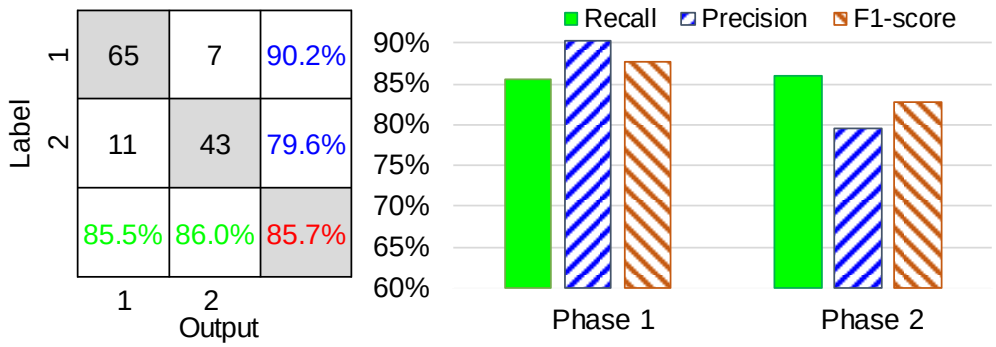

(a) Confusion matrix (b) Recall, precision, and F1-score

Figure 5.12 Performance of CNN model using data from a single sensor

5.5.4 Evaluation of ASR using stacked autoencoder

The FFT magnitudes of AE signals were employed as the input for the stacked autoencoder models. The ratios of training and validation data for the autoencoder models were consistent with the selected ratios for CNN models. The assigned classes (phases) for the AE signals were utilized as the data labels, similar to the CNN models. The results are presented in Fig. 11. The accuracy of classification using all signals is 72.6%. The precision parameters for phases 1 and 2 are 76.1% and 68.4%, respectively. The recall parameter for phases 1 and 2 are 74.6% and 70.1%, respectively (Figure 5.13a). The F1-score parameter for phases 1 and 2 are 75.4% and 69.2%, respectively (Figure 5.13b). The total accuracy of classification for the autoencoder model using signals from a single sensor is 80.2%. The precision values for phases 1 and 2 are 87.8% and 61.1%, respectively. The recall values of phases 1 and 2 are 84.9% and 66.7%, respectively (Figure 5.13c). The F1-score values for phases 1 and 2 are 86.3% and 66.4%, respectively (Figure 5.13d).

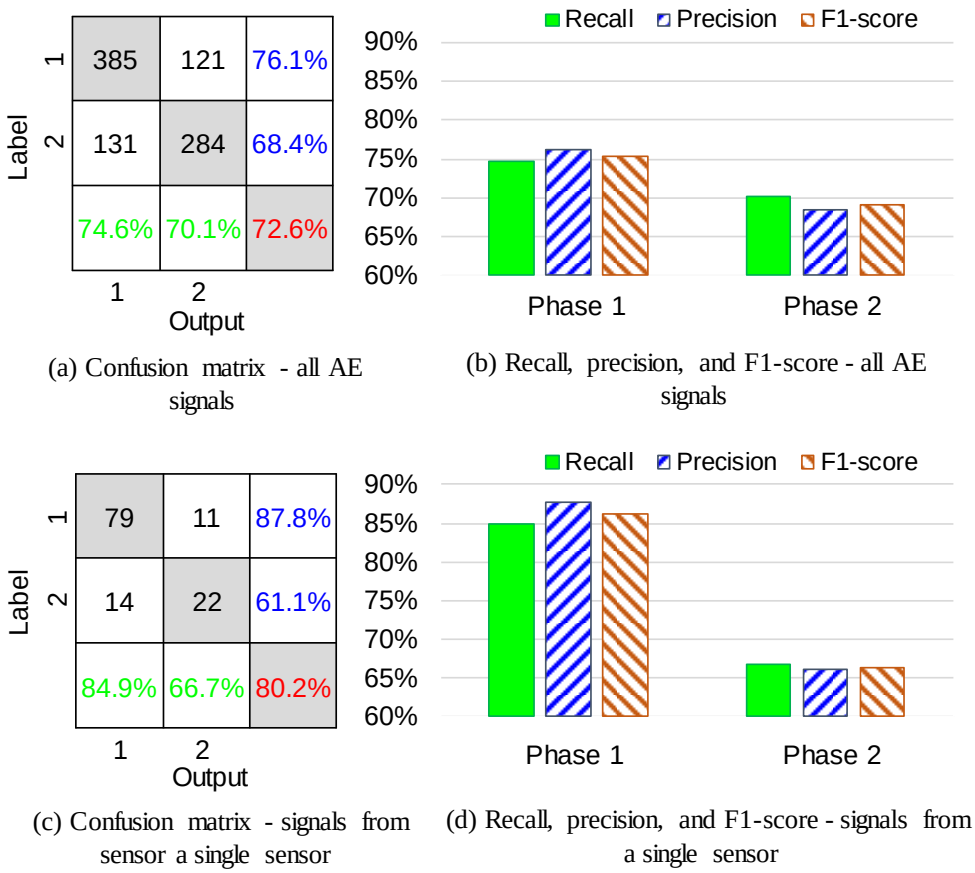

(a) Confusion matrix - all AE signals

(b) Recall, precision, and F1-score - all AE signals

(c) Confusion matrix - signals from sensor a single sensor

(d) Recall, precision, and F1-score - signals from a single sensor

Figure 5.13 Performance of stacked autoencoder

5.5.5 Comparison and discussion

Two shallow machine learning methods, Support Vector Machine (SVM) and K-Nearest Neighbor (KNN) were also utilized to correlate AE signals to ASR expansion, and the results were compared with the deep learning models. The input data of the machine learning models are the parametric features extracted from the AE waveforms. The names of the features and their description are presented in Table 5.1. According to the accuracies observed in CNN and stacked autoencoder, the model trained by signals from a single sensor indicated a higher accuracy than the models using all signals. Therefore, in this paper, the SVM and KNN models were trained and tested by the signal features from the single sensor.

Table 5.1 Descriptions of the input parametric features

Parametric features	Feature descriptions
Amplitude	The peak amplitude of AE waveform
Energy	The measure of the electrical energy measured for an AE signal
Count	The number of threshold crossings
Counts to peak (PCNTS)	The number of threshold crossings from the first threshold crossing to the peak
Rise time	The time interval between first threshold crossing and peak
Duration	The time between the first and last threshold crossing
Average frequency	Counts divided by Duration
Signal strength	A parameter to characterize the overall frequency content of an AE signal
Absolute energy	The absolute measure of the electrical energy measured for an AE signal
Peak frequency	Frequency of maximum signal contribution
Reverberation frequency	Frequency after the peak
Initial frequency	Frequency before the peak
Signal strength	Integral of the rectified voltage signal over the duration of the AE waveform

In this paper, the RBF was selected as the kernel function of SVM [56]. The "K" for the KNN model was set to 4 after conducting serval trial and error tests. The classification accuracy of the CNN models, the stacked autoencoder, SVM, and KNN are presented in Table 5.2. The CNN models have higher classification accuracies than the autoencoder model, and the deep learning methods have higher accuracies than the two shallow machine learning methods. The accuracy of the CNN model using the data from a single sensor is the highest among the evaluated methods (85.2%). Computing time is evaluated for the models. The average time required for training and the average time to classify a single signal in the test dataset are presented in Table 5.2. The training time for CNN process (using GPU-GTX-1080) are significantly more than the training times for the other models using intel i7-6700 CPU. However, the times for the trained models to classify a single AE signal are almost similar, as shown in Table 5.2. All the trained models can finish their task within 0.1 seconds. For the application envisioned, the model will be trained offline; therefore, the training time will not be a primary concern.

Table 5.2 Accuracies and computing times of all the models

Models	Accuracy	Training Time (s)	Testing time (s)	Platform
Stacked autoencoder (all signals)	72.6%	377.64	0.04	CPU i7-6700
Stacked autoencoder (signals from a single sensor)	80.2%	219.57	0.03	CPU i7-6700
CNN (all signals)	76.7%	1562.12	0.08	GPU GTX1080
CNN (signals from a single sensor)	85.2%	612.36	0.06	GPU GTX1080
SVM (features from a single sensor)	71.2%	2.51	0.01	CPU i7-6700
KNN (features from a single sensor)	69.2%	1.64	0.01	CPU i7-6700

The F1-scores parameters for the four proposed models are presented in Figure 5.14. F1-score values of the CNN model using data from the single sensor are generally the highest, and they are relatively consistent between the two classes (Figure 5.14). However, a notable difference of F1-scores in the two classes can be observed in the autoencoder models (Figure 5.14).

The CNN model using data from the single sensor has the highest accuracy and the most consistent performance among the two classes. Therefore, the CNN model is a better option to estimate the range of ASR volumetric strains from AE signals than the autoencoder models.

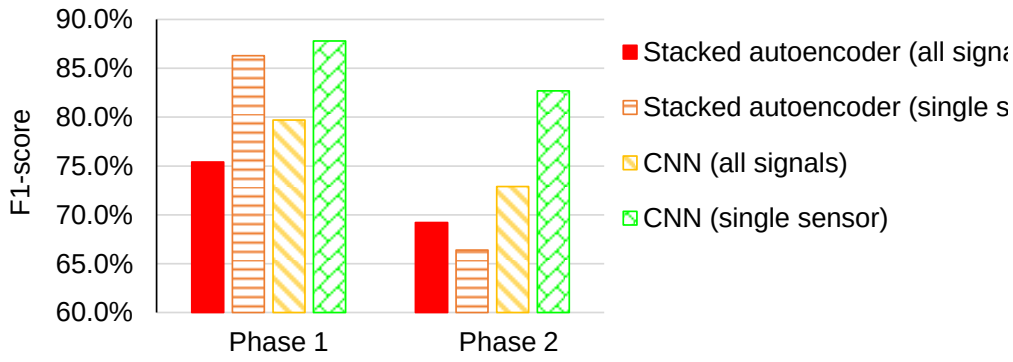

Fig 5.14 F1-score of phases 1 and phase 2

5.6 Summary and conclusions

The evaluation method based on deep learning is proposed to assess the condition of ASR progress in concrete structures. To verify the effectiveness of the proposed method, a concrete specimen with reactive coarse and reinforcements was cast and placed in a chamber for 300 days to accelerate the ASR by providing high temperature and humidity. AE sensors were affixed on the specimen surfaces to acquire stress waves emitted during the ASR due to cracking. The ASR expansion was measured using DEMEC gauge on a regular basis. A CNN and stacked autoencoder models were trained using the AE data for classification purposes and determining ASR volumetric strain ranges. The main conclusions of the paper are summarized as follows:

Both CNN and stacked autoencoder can classify the AE signals to their ASR phases with acceptable accuracy, while a higher accuracy was observed in the classification using the CNN than stacked autoencoder. In addition, using AE signals from a single sensor leads to a better performance of classification than using signals captured by all the sensors.

The F1-scores indicated that the classification result of CNN using signals from a single sensor has the best performance in both phases (classes). Moreover, good consistency of F1-scores between two phases was observed for the CNN models.

Considering computing time, global accuracy, and classifier performance in two phases, the CNN model using the data from a single sensor is the most efficient model among the evaluated models to monitor the temporal evolution of the concrete specimen affected by ASR.

Having access to ASR data for real concrete structures is one of the practical issues for training a supervised learning method. Future research could focus on either the novel AE data augmentation method or utilizing numerical model to generate enough number of training data.

5.7 Acknowledgments

This research was partially supported by the U.S Department of Energy-Nuclear Energy University Program (NEUP) under the contract DE-NE0008544 and the U.S. Department of Energy Office of Science, Office of Basic Energy Sciences and Office of Biological and Environmental Research under Award Number DE-SC-00012530.

5.8 References

[1] V. Soltangharaei, R. Anay, N.W. Hayes, L. Assi, Y. Le Pape, Z.J. Ma, P. Ziehl,2018. Damage mechanism evaluation of large-scale concrete structures affected by alkali-silica reaction using acoustic emission, Applied Sciences 8 2148.

[2] F. Bach, T.S. Thorsen, M. Nielsen,1993. Load-carrying capacity of structural members subjected to alkali-silica reactions, Construction and Building Materials 7 109-115.

[3] J. Bakker, Control of ASR related risks in the Netherlands, 2008, 16-20.

[4] L. Clark, Critical review of the structural implications of the alkali silica reaction in concrete, Bridges Design, Structures Group, Transportation andRoad Research Laboratory, 1989.

[5] J.W. Schmidt, S.G. Hansen, R.A. Barbosa, A. Henriksen,2014. Novel shear capacity testing of ASR damaged full scale concrete bridge, Engineering Structures 79 365-374.

[6] A. Campos, C.M. Lopez, A. Blanco, A. Aguado,2018. Effects of an internal sulfate attack and an alkali-aggregate reaction in a concrete dam, Construction and Building Materials 166 668-683.

[7] G. Plusquellec, M.R. Geiker, J. Lindgård, K. De Weerdt,2018. Determining the free alkali metal content in concrete–Case study of an ASR-affected dam, Cement and Concrete Research 105 111-125.

[8] V.E. Saouma, M.A. Hariri-Ardebili,2014. A proposed aging management program for alkali silica reactions in a nuclear power plant, Nuclear Engineering and Design 277 248-264.

[9] V. Soltangharaei, R. Anay, L. Assi, P. Ziehl, F. Matta, Damage identification in cement paste amended with carbon nanotubes, AIP Publishing LLC, 2018, 030006.

[10] T. Takakura, S. Mitsuki, K. Takiguchi, I. Nishiguchi, T. Ishikawa, N. Matsumoto, Y. Masuda,2005. Investigation on the expansion value of turbine generator foundation affected by alkali-silica reaction.

[11] J. Tcherner, T.S. Aziz,2009. Effects of AAR on seismic assessment of nuclear power plants for life extensions.

[12] F. Rajabipour, E. Giannini, C. Dunant, J.H. Ideker, M.D. Thomas,2015. Alkali–silica reaction: current understanding of the reaction mechanisms and the knowledge gaps, Cement and Concrete Research 76 130-146.

[13] K. Ono,2011. Application of acoustic emission for structure diagnosis, Diagnostyka 3-18.

[14] R. Anay, V. Soltangharaei, L. Assi, T. DeVol, P. Ziehl,2018. Identification of damage mechanisms in cement paste based on acoustic emission, Construction and Building Materials 164 286-296.

[15] V. Soltangharaei, R. Anay, L. Ai, E.R. Giannini, J. Zhu, P. Ziehl,2020. Temporal Evaluation of ASR Cracking in Concrete Specimens Using Acoustic Emission, Journal of Materials in Civil Engineering 32 04020285.

[16] R. Anay, A. Lane, D.V. Jáuregui, B.D. Weldon, V. Soltangharaei, P. Ziehl,2020. On-Site Acoustic-Emission Monitoring for a Prestressed Concrete BT-54 AASHTO Girder Bridge, Journal of Performance of Constructed Facilities 34 04020034.

[17] D. Li, K.S.C. Kuang, C.G. Koh,2017. Fatigue crack sizing in rail steel using crack closure-induced acoustic emission waves, Measurement Science and Technology 28 065601.

[18] L. Assi, V. Soltangharaei, R. Anay, P. Ziehl, F. Matta,2018. Unsupervised and supervised pattern recognition of acoustic emission signals during early hydration of Portland cement paste, Cement and Concrete Research 103 216-225.

[19] V. Soltangharaei, J. Hill, L. Ai, R. Anay, B. Greer, M. Bayat, P. Ziehl,2020. Acoustic emission technique to identify stress corrosion cracking damage, Structural Engineering and Mechanics 75 723-736.

[20] M. Abdelrahman, M.K. ElBatanouny, P. Ziehl, J. Fasl, C.J. Larosche, J. Fraczek,2015. Classification of alkali–silica reaction damage using acoustic

emission: A proof-of-concept study, Construction and Building Materials 95 406-413.

[21] Y. Farnam, M.R. Geiker, D. Bentz, J. Weiss,2015. Acoustic emission waveform characterization of crack origin and mode in fractured and ASR damaged concrete, Cement and Concrete Composites 60 135-145.

[22] T. Lokajíček, R. Přikryl, Š. Šachlová, A. Kuchařová,2017. Acoustic emission monitoring of crack formation during alkali silica reactivity accelerated mortar bar test, Engineering Geology 220 175-182.

[23] F. Weise, K. Voland, S. Pirskawetz, D. Meinel, Innovative measurement techniques for characterising internal damage processes in concrete due to ASR, 2012, 20-25.

[24] L. Ai, V. Soltangharaei, M. Bayat, B. Greer, P. Ziehl,2021. Source localization on large-scale canisters for used nuclear fuel storage using optimal number of acoustic emission sensors, Nuclear Engineering and Design 375 111097.

[25] I. Goodfellow, Y. Bengio, A. Courville, Y. Bengio, Deep learning, MIT press Cambridge, 2016.

[26] R. Sun, Y. Chen, A. Dubey, P. Pugliese,2021. Hybrid electric buses fuel consumption prediction based on real-world driving data, Transportation Research Part D: Transport and Environment 91 102637.

[27] M. Sadoughi, A. Downey, G. Bunge, A. Ranawat, C. Hu, S. Laflamme,2018. A deep learning-based approach for fault diagnosis of roller element bearings.

[28] J. Redmon, A. Farhadi,2018. Yolov3: An incremental improvement, arXiv preprint arXiv:1804.02767.

[29] S. Ren, K. He, R. Girshick, J. Sun,2016. Faster R-CNN: towards real-time object detection with region proposal networks, IEEE transactions on pattern analysis and machine intelligence 39 1137-1149.

[30] A. Khan, A. Sohail, U. Zahoora, A.S. Qureshi,2020. A survey of the recent architectures of deep convolutional neural networks, Artificial Intelligence Review 53 5455-5516.

[31] F. Guo, Y. Qian, Y. Wu, Z. Leng, H. Yu,2021. Automatic railroad track components inspection using real‐time instance segmentation, Computer‐Aided Civil and Infrastructure Engineering 36 362-377.

[32] X.-X. Niu, C.Y. Suen,2012. A novel hybrid CNN–SVM classifier for recognizing handwritten digits, Pattern Recognition 45 1318-1325.

[33] T.-Y. Kim, S.-B. Cho,2019. Predicting residential energy consumption using CNN-LSTM neural networks, Energy 182 72-81.

[34] A. Ebrahimkhanlou, B. Dubuc, S. Salamone,2019. A generalizable deep learning framework for localizing and characterizing acoustic emission sources in riveted metallic panels, Mechanical Systems and Signal Processing 130 248-272.

[35] D. Li, Y. Wang, W.-J. Yan, W.-X. Ren,2020. Acoustic emission wave classification for rail crack monitoring based on synchrosqueezed wavelet transform and multi-branch convolutional neural network, Structural Health Monitoring 1475921720922797.

[36] S.A. Shevchik, C. Kenel, C. Leinenbach, K. Wasmer,2018. Acoustic emission for in situ quality monitoring in additive manufacturing using spectral convolutional neural networks, Additive Manufacturing 21 598-604.

[37] L. Ai, V. Soltangharaei, M. Bayat, M. van Tooren, P. Ziehl,2021. Detection of impact on aircraft composite structure using machine learning techniques, Measurement Science and Technology.

[38] L. Gou, H. Li, H. Zheng, H. Li, X. Pei,2020. Aeroengine Control System Sensor Fault Diagnosis Based on CWT and CNN, Mathematical Problems in Engineering 2020.

[39] D. Li, K.S.C. Kuang, C.G. Koh,2018. Rail crack monitoring based on Tsallis synchrosqueezed wavelet entropy of acoustic emission signals: A field study, Structural Health Monitoring 17 1410-1424.

[40] J.M. Lilly, S.C. Olhede,2008. Higher-order properties of analytic wavelets, IEEE Transactions on Signal Processing 57 146-160.

[41] A. Krizhevsky, I. Sutskever, G.E. Hinton, Imagenet classification with deep convolutional neural networks, 2012, 1097-1105.

[42] Y. Sun, H. Zhang, T. Zhao, Z. Zou, B. Shen, L. Yang,2020. A New Convolutional Neural Network With Random Forest Method for Hydrogen Sensor Fault Diagnosis, IEEE Access 8 85421-85430.

[43] C. Szegedy, W. Liu, Y. Jia, P. Sermanet, S. Reed, D. Anguelov, D. Erhan, V. Vanhoucke, A. Rabinovich, Going deeper with convolutions, 2015, 1-9.

[44] J. Deng, W. Dong, R. Socher, L.-J. Li, K. Li, L. Fei-Fei, Imagenet: A large-scale hierarchical image database, Ieee, 2009, 248-255.

[45] F. König, C. Sous, A.O. Chaib, G. Jacobs,2021. Machine learning based anomaly detection and classification of acoustic emission events for wear monitoring in sliding bearing systems, Tribology International 155 106811.

[46] F. König, G. Jacobs, A. Stratmann, D. Cornel, Fault detection for sliding bearings using acoustic emission signals and machine learning methods, IOP Publishing, 2021, 012013.

[47] H. Xin, L. Cheng, R. Diender, M. Veljkovic,2020. Fracture acoustic emission signals identification of stay cables in bridge engineering application using deep transfer learning and wavelet analysis, Advances in Bridge Engineering 1 1-16.

[48] Y. Bengio, P. Lamblin, D. Popovici, H. Larochelle, Greedy layer-wise training of deep networks, 2007, 153-160.

[49] A. Ng, S. Autoencoder,2011. CS294A Lecture notes, Dosegljivo: https://web. stanford. edu/class/cs294a/sparseAutoencoder_2011new. pdf.[Dostopano 20. 7. 2016].

[50] K. Sadananda, I. Adlakha, K.N. Solanki, A. Vasudevan,2020. Analysis of the Crack Initiation and Growth in Crystalline Materials Using Discrete Dislocations and the Modified Kitagawa–Takahashi Diagram, Crystals 10 358.

[51] E.N. Landis, S.P. Shah,1995. Frequency-dependent stress wave attenuation in cement-based materials, Journal of Engineering Mechanics 121 737-743.

[52] G. Lacidogna, G. Piana, A. Carpinteri,2017. Acoustic emission and modal frequency variation in concrete specimens under four-point bending, Applied Sciences 7 339.

[53] V. Soltangharaei, R. Anay, D. Begrajka, M. Bijman, M.K. ElBatanouny, P. Ziehl, M.J. Van Tooren, A minimally invasive impact event detection system for aircraft movables, 2019, 1268.

[54] M. Buckland, F. Gey,1994. The relationship between recall and precision, Journal of the American society for information science 45 12-19.

[55] L. Zhong, L. Hu, H. Zhou,2019. Deep learning based multi-temporal crop classification, Remote sensing of environment 221 430-443.

[56] B. Scholkopf, K.-K. Sung, C.J. Burges, F. Girosi, P. Niyogi, T. Poggio, V. Vapnik,1997. Comparing support vector machines with Gaussian kernels to radial basis function classifiers, IEEE transactions on Signal Processing 45 2758-2765.

Chapter 6

A Transfer Learning Approach for Acoustic Emission Localization on Stainless Steel Structure Using Numerical Simulation and Unsupervised Domain Adaptation[1]

[1] Li Ai, Paul Ziehl. A Transfer Learning Approach for Acoustic Emission Localization on Stainless Steel Structure Using Numerical Simulation and Unsupervised Domain Adaptation. To be submitted to a journal

6.1 Abstract

The detection and localization of damage in metallic structures using acoustic emission (AE) monitoring and artificial intelligence technology such as deep learning has been widely studied. However, a current challenge of this approach is the difficulty of obtaining sufficient labeled historical AE signals for the training process of deep learning models. This problem can be approached through the implementation of transfer learning. The innovation of this paper lies in the development of a transfer learning approach for AE source localization on the stainless-steel structures when no historical labeled AE signals are available for training. A finite element model is developed to generate numerical AE signals for the training. Unsupervised domain adaptation technology is utilized to reduce the distribution difference between the numerical and the realistic AE signals and derived the localization results of the unlabeled realistic AE signals. The results suggest that the proposed approach is able to localize the AE signals with high accuracy without using labeled training data

Keywords: Acoustic emission; finite element modeling; source localization; transfer learning; unsupervised domain adaptation

6.2 Introduction

Metallic material is one of the important construction materials for infrastructure components. Some metallic structures such as rails, bridges, and nuclear facilities are subject to structural damage due to environmental erosion [1-3], fatigue damage [4; 5], and other factors after long periods of use. Ensuring the integrity and safety operation of the metallic structures over their service life is a significant task. Traditional approaches included regular-base visual inspection has been applied to inspect and monitor damage

on metallic structures. However, the visual inspection of large-scale structures is usually time-consuming and prone to human error. To improve the reliability and efficiency of damage inspection, an automatic monitoring approach is thereby needed.

Acoustic emission (AE) is a structural health monitoring method that is extremely sensitive to damage propagation in materials [6-14]. The detection and localization of the cracks in metallic structures can be implemented by deploying an AE sensor array [15-17]. Pearson et al. [15] developed the Akaike information criteria Delta-t mapping technique to overcome the difficulty of applying traditional time-of-arrival techniques to locate AE events in complex metal structures. The results show that the Akaike information criteria Delta-t mapping technique is a feasible option for AE source localization. Sai et al. [16] proposed a novel AE localization method and a detection system for AE localization based on time reversal focusing imaging and fiber Bragg grating sensors network. Results indicating the method improved the AE detection and source localization with high precision. Yan et al. [17] proposed a new method to solve the multi-leakage source location problem of metal pressure vessels using AE sensors combined with a multi-signal classification (MUSIC) algorithm and wavelet packet analysis. AE sensors are deployed into a linear array to acquire signals from multiple leakage sources. The results suggested that the method can successfully locate two leak sources. Results from previous studies indicated that AE monitoring with multiple sensors has a good capability to detect and identify cracks in metallic specimens. However, there is a problem when applying AE monitoring in realistic complex metallic infrastructures. For some cases, the available area for sensor attachment is limited, it would be difficult to deploy sensor arrays to localize the damages. An intelligent and

automatic localization approach with only using a single AE sensor can be beneficial to the detection and localization of the damages in complex metallic infrastructures.

Adopting artificial intelligence techniques such as machine learning and deep learning can be an approach. Machine learning is a supervised intelligent data processing technique [18]. By learning the feature extracted from the data, machine learning can understand the pattern of data and make a decision [19]. Machine learning models such as artificial neural network, support vector machine (SVM), K-nearest neighbor (KNN), and random forest has been widely utilized for signal processing [20-25]. Deep learning methods are improved intelligent techniques which are based on machine learning. It can automatically learn features from complex data sets without feature extractions [26]. In recent years, machine learning and deep learning have been applied to AE localization using a single AE sensor [27-29]. Ebrahimkhanlou et al. [27] proposed a deep learning framework based on a stacked autoencoder network to locate AE events on the metallic structures. Ai et al. [28] studied the single sensor AE source localization on the stainless steel canister by leveraging an artificial neural network and random forest. Ai et al. [29] developed a passive health monitoring system to locate impacts on an aircraft component using one AE sensor, random forest, and stacked autoencoder network.

Previous studies have proven that using deep learning to localize AE signals is promising. However, a current challenge of using the supervised learning algorithms on AE source localization is the difficulty to have access to the labeled AE signals for existing structures. Transfer learning (TL) is a strategy to assist the supervised learning task when the available training data is limited [30]. TL has been utilized in the application of acoustic emission [31; 32]. Li et al. [31] utilized a multi-branch CNN

model for AE wave classification on rails. The weights of a pre-trained AlexNet are adopted except the last fully connected later to save time for training and to acquire a robust network using limited training AE data available. Chen et al. [32] proposed a transfer learning approach for AE–based rail condition evaluation. The weights of a CNN model trained by open-access audio data were utilized to train on the AE signals collected from the experiment. TL has a good performance in the aforementioned studies. However, those studies focused on the scenarios when the training AE signals are limited but still available. The authors are currently not aware of the publications of the studies that using deep learning algorithm to localize the AE signals on metallic structure with no labeled training AE signals available. Therefore, this paper investigates a novel TL approach for AE localization on stainless steel structures without labeled historical AE signals to fill the prementioned gap. A finite element model is developed to generate numerical AE signals for the training of deep learning algorithm. Unsupervised domain adaptation technology is utilized to decrease the difference between the generated numerical AE signals with realistic AE signals.

6.3 Theoretical background

6.3.1 Transfer learning and unsupervised domain adaptation

The basic principles of transfer learning (TL) and unsupervised domain adaptation are introduced in this section. Generally, a sufficient number of training data and the corresponding labels are required by a supervised learning model such as artificial neural network, and decision tree. However, in some cases, enough training data with labels are difficult to obtain. TL is a strategy to solve this problem. Assuming there are two datasets. The first dataset $\{X_s, Y_s\} = \{(x_{s1}, x_{s2}, \dots, x_{sm}), (y_{s1}, y_{s2}, \dots, y_{sm})\}$. Where

$(y_{s1}, y_{s2}, \ldots, y_{sm})$ is the label of $(x_{s1}, x_{s2}, \ldots, x_{sm})$, and it is known. The second dataset $\{X_t, Y_t\} = \{(x_{t1}, x_{t2}, \ldots, x_{tn}), (y_{t1}, y_{t2}, \ldots, y_{tn})\}$, while the labels $(y_{t1}, y_{t2}, \ldots, y_{tn})$ are unknown for this dataset. The concept of transfer learning is to execute the classification of $\{X_t, Y_t\}$ based on the acquired knowledge from the model with training on $\{X_s, Y_s\}$. The dataset $\{X_s, Y_s\}$ is named source domain (D_S) and the dataset $\{X_t, Y_t\}$ to be classified is called target domain (D_T). One of the issues of TL is, the performance of TL based on D_S and D_T is not good when the difference between the source domain and the target domain is significant. Unsupervised domain adaptation is a technique to learn the domain invariant features from the annotated source domain and the unannotated target domain and reduce the distribution difference [33].

6.3.2 Manifold embedded distribution alignment

As mentioned above, $D_S: \{X_s, Y_s\}$, and $D_T: \{X_t, Y_t\}$ has different data destruction which means they have different marginal probabilities $(P_s(x_s) \neq P_t(x_t))$. and different conditional probability $(Q_s(x_s|y_s) \neq Q_t(x_t|y_t))$. Manifold embedded distribution alignment (MEDA) is an unsupervised domain adaptation algorithm to reduce the distribution difference by utilizing manifold feature learning and dynamic distribution alignment [34]. Manifold feature learning is utilized to reduce the data drift between the source domain and target domain. Dynamic distribution alignment is employed to alignment the marginal and conditional distribution. The MEDA aims to articulate a cross-domain classifier f to predict the unknown Y_t.

6.3.3 Manifold feature learning

Manifold feature learning is an unsupervised domain adaptation method [35]. Manifold refers to the space with local Euclidean spatial properties, including curves and

surfaces of various dimensions. One of the characterizes of manifold space is that features in the manifold space usually have good geometric structures. The manifold learning leverage this characterize to avoid feature distortions by mapping high-dimensional data into a low-dimensional manifold space. In MEDA, the geodesic flow kernel (GFK) is employed to conduct the manifold feature transformation. More details about GFK can be found in [36]. The process of manifold feature learning in MEDA is presented in Fig 6.1.

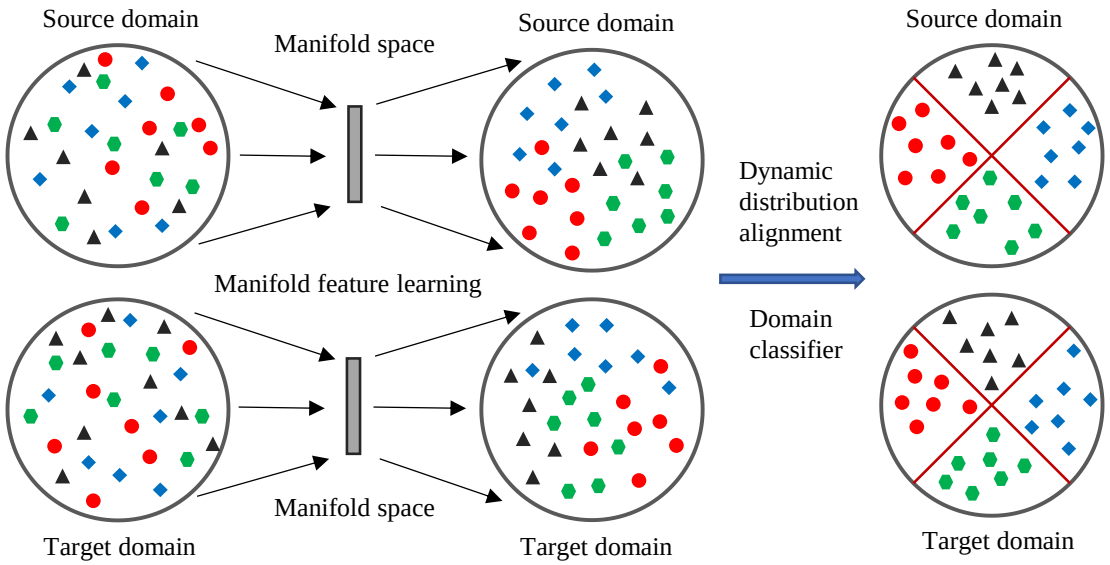

Figure 6.1 Procedures of MEDA

6.3.4 Dynamic distribution alignment

The importance of marginal distributions (P) and conditional distributions (Q) of the source domain and target domain tend to vary with the similarity of the two domains. For instance, marginal distribution is more significant when there are large differences between the source domain and target domain, while conditional distribution is more dominant when the two domains have high similarities. Therefore, the importance of P and Q needs to be quantitatively measured, rather than simply counting them with the

same weights. To accomplish this goal, the dynamic distribution alignment process is proposed in MEDA to dynamically evaluate the importance of these two distributions. The process of dynamic distribution alignment could be presented by Eq. (6.1):

$$\overline{D_f}(D_S, D_t) = (1-\omega)D_f(P_s, P_t) + \omega \sum_{t=1}^{T} D_f^{(t)}(Q_s, Q_t) \quad (6.1)$$

Where, $t \in \{1,2,3,\dots,T\}$ represents the classes of data, $\overline{D_f}(D_S, D_t)$ is the distribution after alignment. $D_f(P_s, P_t)$ refers to the marginal distribution alignment. $D_f^{(t)}(Q_s, Q_t)$ is the conditional distribution alignment for class t. $\omega \in [0,1]$ refers to the adaptive factor. If ω is close to 0, meaning the distribution difference between the source domain and target domain is large. Therefore, marginal distribution alignment is more important. If ω is close to 1, it means the difference between domains is small, and the conditional distribution alignment is more dominant. $\omega = 0.5$ mans the marginal and conditional distribution share equal importance. The optimizing of ω will be introduced in the following paragraph.

Maximum mean discrepancy (MMD) is utilized to explore the distribution distance between two domains [37]. The MMD distance between domain a and b could be obtained by Eq. (6.2):

$$MMD^2(a, b) = \|E_m[\theta(Z_s)] - E_c[\theta(Z_t)]\|_{H_k}^2 \quad (6.2)$$

Where, $MMD(a, b)$ is the distance between domain a and b, H_k refers to the reproducing kernel Hilbert space induced by feature map $\theta(\cdot)$, $E[\cdot]$ is the mean of the embedded samples. Z_s and Z_t are the features transformed to the reproducing kernel Hilbert space.

For the purpose of computing the MMD about f, the projected MMD [38] is adopted to calculate the marginal distribution alignment ($D_f(P_s, P_t)$) and conditional distribution alignment ($D_f^{(t)}(Q_s, Q_t)$) by the following equations:

$$D_f(P_s, P_t) = \|E_m[f(Z_s)] - E_c[f(Z_t)]\|_{H_k}^2 \tag{6.3}$$

$$D_f^{(t)}(Q_s, Q_t) = \left\| E_m\left[f(Z_s^{(t)})\right] - E_c\left[f(Z_t^{(t)})\right] \right\|_{H_k}^2 \tag{6.4}$$

By substituting Eq. (3) and (4) into Eq. (1), the final dynamic distribution alignment could be obtained by Eq. (6.5):

$$\overline{D_f}(D_S, D_t) = (1-\omega)\|E_m[f(Z_s)] - E_c[f(Z_t)]\|_{H_k}^2 + \omega \sum_{t=1}^{T} \left\| E_m\left[f(Z_s^{(t)})\right] - E_c\left[f(Z_t^{(t)})\right] \right\|_{H_k}^2 \tag{6.5}$$

After the manifold feature learning and dynamic distribution alignment are completed. A domain classifier can be derived by Eq. (6.6). The procedure of dynamic distribution alignment and classification is illustrated in Figure 6.1.

$$f = \arg\min \sum_{i=1}^{t} (y_i - f(Z_i))^2 + \alpha \|f\|_K^2 + \beta \overline{D_f}(D_S, D_t) + \gamma R_f(D_S, D_t) \tag{6.6}$$

Where, $R_f(\cdot)$ is a Laplacian regularization to utilize the similar geometric properties of the nearest point in the manifold. α, β and γ are the regularization parameters.

The label Y_t of the target domain could be obtained by the domain classifier. However, the confidence level of the obtained label may not be high because the adaptive factor ω might not be the optimized value. Therefore, an optimization process of ω is designed in MEDA. The main procedure can express by Eq. (6.7):

$$\omega = 1 - \frac{d_P}{d_P + \sum_{t=1}^{T} d_Q} \tag{6.7}$$

Where, d_P refers to the *A*-distance [39] of marginal distribution, d_Q refers to the *A*-distance of the conditional distribution of each class.

The adaptive factor ω will be calculated at every iteration of the dynamic distribution adaptation, and the predicted label Y_t will also be updated with the iterations. More details about dynamic distribution alignment could be found in [34].

6.3.5 Acoustic emission monitoring

Acoustic emission is a physical phenomenon, which is related to the stress wave generated by the rapid release of elastic energy when cracks or damages form in materials [40]. AE signals can be detected and collected by deploying AE sensors on the surface of an object. The method of recording and processing AE signals to diagnose the health status of an object is referred to as AE monitoring. Conventional approaches such as the time of arrival method have been widely utilized to localize the AE source by deploying sensor arrays. Usually, three or more sensors are needed. Several studies have focused on using one AE sensor to localize the AE source based on deep learning and deep learning algorithm. However, a current challenge of this approach is the difficulty of obtaining the labeled AE signals for the training process of machine learning and deep learning models. A TL approach was proposed in this paper to solve this problem. Details of the approach will be introduced in the following paragraph.

6.4 Materials and Experimental Setup

The experiment is aimed to collect the AE signals as the source domain for the TL AE source localization approach proposed in this paper. A specimen fabricated from 304 stainless steel is utilized in the experiment. The dimension of the specimen is 0.61 x 0.30 x 0.00635 meters. The plan view of the specimen is provided in Figure 6.2.

6.4.1 Experiment procedures

The Hsu-Nielsen pencil lead break (PLB) is one of the widely used artificial sources to generate AE signals by conducting pencil lead break on the object to which the AE sensor is attached [41]. In this paper, A Hsu-Nielsen PLB test was conducted to simulate the cracks on the steel plate. Four zones were set up on the specimen. The center of each zone is marked as red dots. The PLB was repeated 100 times on each of these points. A single AE sensor was attached to the corner of the specimen. 400 AE events were collected during the experiment. The location of the AE sensor and the four zones are shown in Figure 6.2.

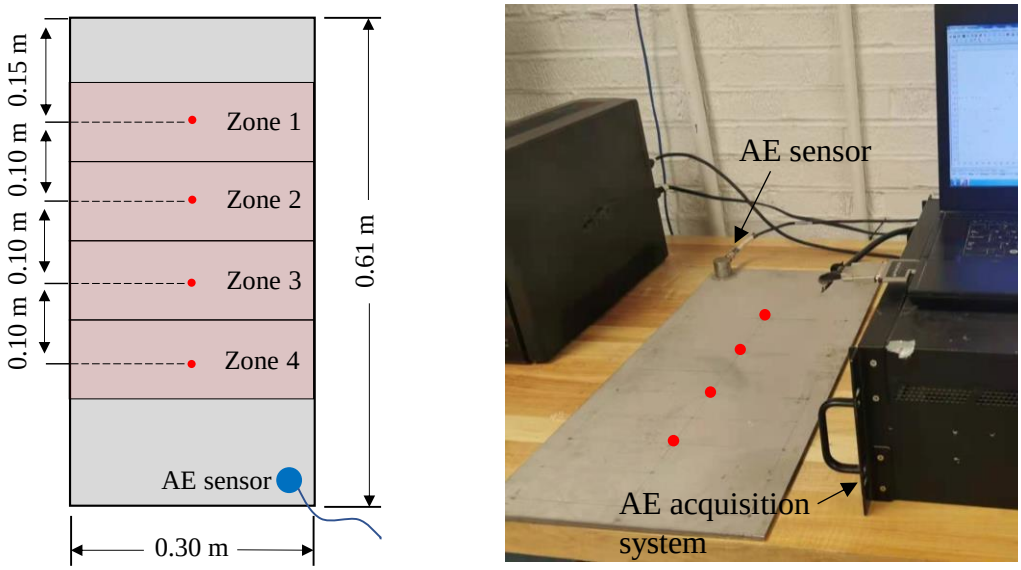

Figure 6.2 Experimental setup

6.4.2 Acoustic emission instrument setup

The hardware of the AE system was produced by the MISTRAS Group Inc., Princeton Junction, New Jersey. The AE sensor utilized in this experiment is wideband type WDI-AST. The sensors have an operating frequency range of 100-900 kHz. The AE sensors were attached to the specimen by using red double/bubble epoxy. AE signals

were acquired by a 16-channel DISP system. The details regarding the AE acquisition parameters are presented in Table 6.1. The pre-trigger time, which recovers AE waveforms before the threshold crossing, was defined as 256 μs. The sampling rate was 1MHz. The duration was set to 2,000 μs. The peak definition time (PDT), which refers to the time between the first threshold crossing to the peak amplitude, was defined as 200 μs, and the hit definition time (HDT) was set to 400 μs. This controls the stop point of recording and is usually twice the peak definition time. The hit lockout time (HLT), which prevents recording late-arriving signals and reflected hits, was set to 400 μs. The threshold was 32 dB. The low and high pass digital filters were set to 20 kHz, and 400 kHz, respectively.

Table 6.1 AE acquisition parameters

Setting	Value
Hit Definition Time	400 μs
Peak Definition Time	200 μs
Hit Lockout Time	200 μs
Sampling Rate	5000 kHz
Threshold	32dB
Pre-trigger Time	256 μs
Low Pass Digital Filter	20 kHz
High Pass Digital Filter	400 kHz

6.5 The proposed TL approach for AE source localization

In this paper, the AE source localization is considered a classification problem. The AE signals will be classified to their corresponding zone. A TL approach for AE source localization by leveraging numerical simulation and unsupervised domain adaptation is proposed. This approach aims to localize the AE events using one AE sensor while no labeled training data is available. A real-sized three-dimensional finite element model is developed to simulate the AE signals generating.

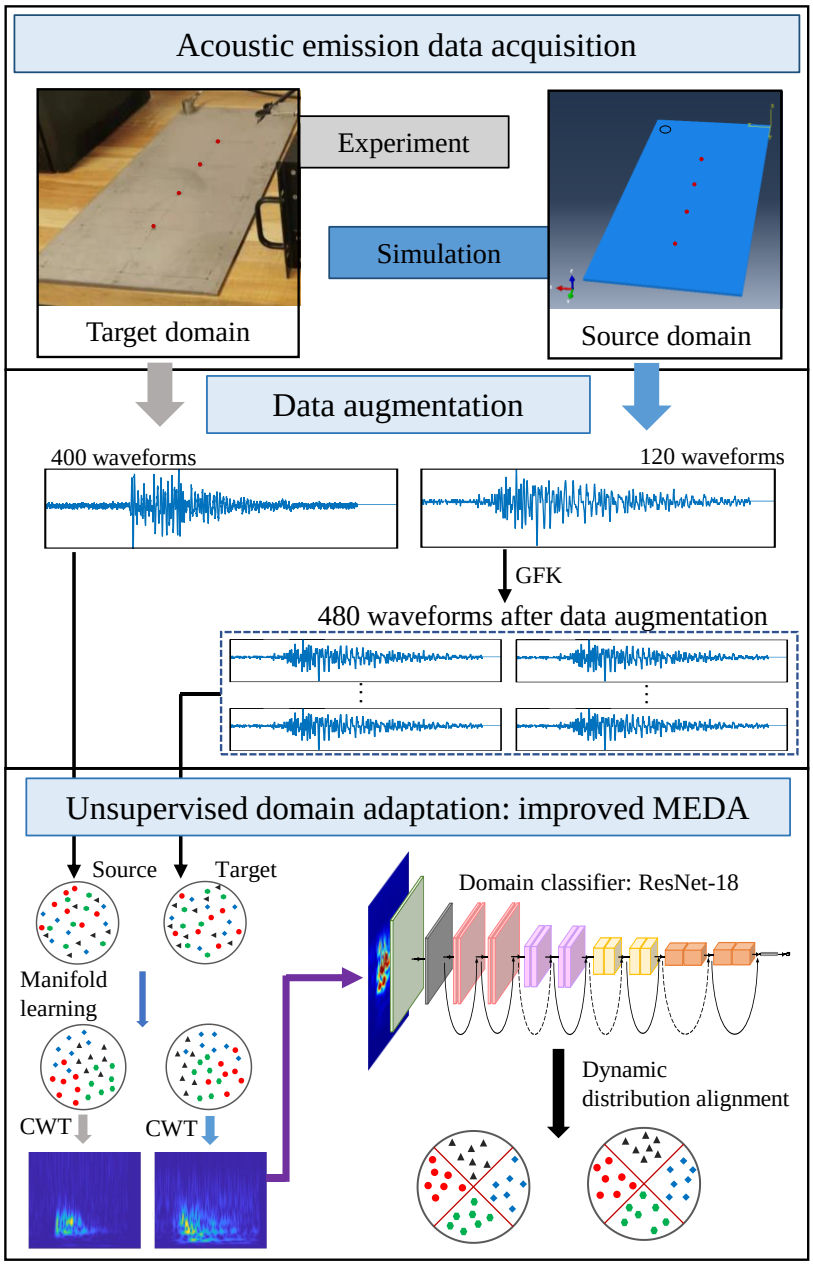

Figure 6.3 Schematic of the proposed TL AE source localization approach

The numerical AE signals obtained by the finite element model will be utilized for data augmentation to enable the large amount of data required for the following training process. The data after augmentation is utilized as the source domain. The AE signals collected during the experiment are employed as the target domain. An improved manifold embedded distribution alignment is utilized as the unsupervised domain

adaptation method to reduce the difference between the source, and the target domain and finally derived the source localization results. The workflow of the proposed approach is presented in Figure 6.3.

6.5.1 Acoustic emission waveform simulation

The finite element model to simulate AE signals emitted is presented in this section. The model was developed on commercial finite element platform ABAQUS and the solver is Explicit. By applying the excitation source and reducing the size of the mesh, the high-frequency dynamic response can be obtained [42-46]. The finite element model has the same dimensions as the steel plate in the experiment. The material property utilized in the model is steel with the young's modulus 193 GPa, the density is 8000 kg/m^3. The mesh size is 0.001 meters. The zonal definition and excitation points are kept the same with the experiment (Figure 6.4a and 6.4b).

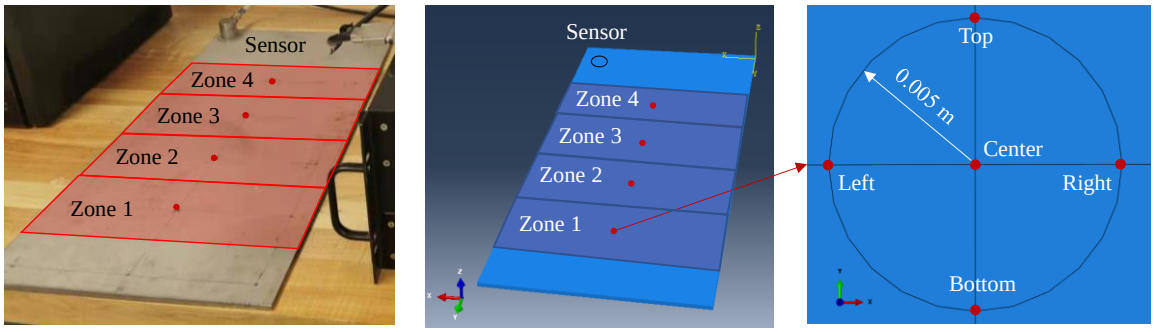

(a) (b) (c)

Figure 6.4 Finite element setup: (a) experimental specimen; (b) finite element model; (c) excitation locations in zone 1

During the experiment, when conducting PLB in one point, the locations to apply the excitations were not exactly in the same points due to human error, a slight position shift is inevitable. To simulate the position shift and also increase the diversity of numerical signals, five sub-points are designed in the model as shown in Fig. 5c. The

excitation sources will be applied in the five sub-points to generate the numerical signals in one zone.

In previous studies, the PLB has been simulated by several excitation functions such as the cosine bell function [46], exponential function [47], and Gaussian distribution function [48]. This paper selected the cosine bell function (Eq. (6.8)) and the exponential function (Eq. (6.9)) as the excitation source in the finite element model. The expressions of the excitation function are presented as follow:

$$F(t) = \begin{cases} \frac{1}{2} - \cos\left((\pi t)\frac{1}{2T}\right) & \text{for } t \le T \\ 1 & \text{for } t > T \end{cases} \tag{6.8}$$

$$F(t) = \begin{cases} \exp\left(-\left(\frac{1}{2}(t-T)\frac{5}{T}\right)^2\right) & \text{for } t \le T \\ 1 & \text{for } t > T \end{cases} \tag{6.9}$$

Where T refers to the period of the functions. In order to further increase the diversity of the numerical signals and simulate the randomness of the period of PLB applied in the experiment, three different periods: $T_1 = 1\ \mu s$, $T_2 = 1.25\ \mu s$, and $T_3 = 1.5\ \mu s$ are utilized for the excitation functions. All the six excitation sources implemented in the model are illustrated in Figure 6.5.

The modeled PLB starts a load of 0 N, ramps up to a certain value, after which it stays constant. The actual load of PLB breaks during the experiment is unknown. This paper assumes the magnitude of the load is 1 N. This assumption value is of low significance because this value will only affect the amplitude of the obtained numerical waveform which will be normalized to -1 and 1.

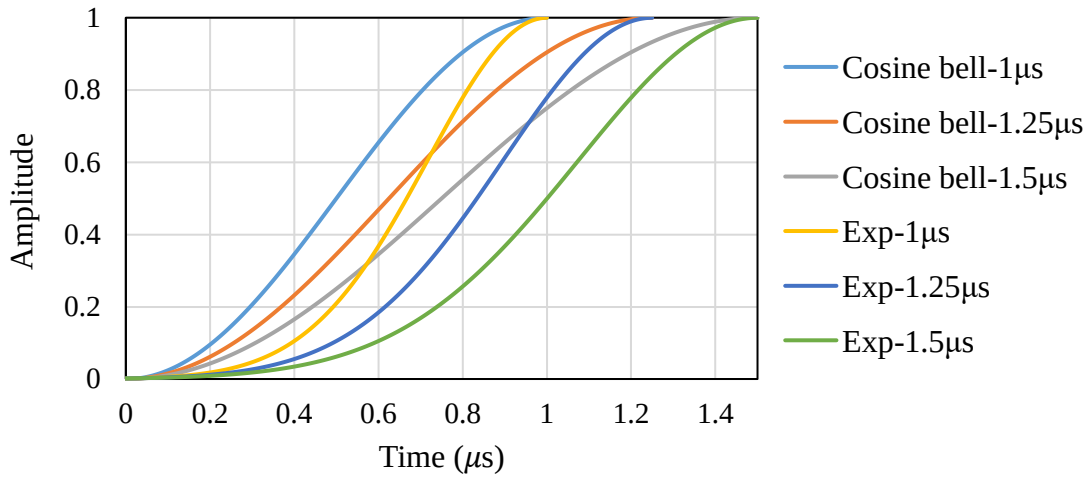

Figure 6.5 Excitation functions

When the stress wave passes through an AE sensor, the bottom surface of the AE sensor is excited by the stress wave and the wave is thereby captured. However, in the FE model, the dynamic response is obtained by extracting the displacement versus time in one node. This node has an infinity small geometry that cannot represent the whole bottom surface of the sensor. Therefore, a combination of multiple nodes would be a strategy to simulate the AE bottom surface. In this paper, a single line output was employed [47]. The out-of-plane displacements of the nodes in a single straight line are collected. A weight is assigned to each node to account for the circular geometry of the sensor. Assume the single line output is composed of n nodes. The combinational output of the n nodes can be calculated based on the following equations:

$$w_i = \frac{dy \cdot dx_i}{\sum_{i=1}^{n} dy \cdot dx_i} = \frac{dy \cdot \sqrt{\left(\frac{D}{2}\right)^2 - cy_i{}^2}}{\sum_{i=1}^{n} dy \cdot \sqrt{\left(\frac{D}{2}\right)^2 - cy_i{}^2}} \tag{6.10}$$

$$U_{sensor} = \sum_{i=1}^{n} w_i \cdot U_i \tag{6.11}$$

Where, w_i is referring to the weight that assigns to the $i\ th$ node from the left side in the x-direction. dy refers to the distance between two nodes, D is the diameter of the AE sensor, Cy_i refers to the distance from the $i\ th$ node to the center of the circle. U_{sensor} is the single line output of the sensor, U_i is nodal out of plane displacement of the $i\ th$ node. All the parameters in the equation are shown in the schematic bottom view of the sensor (Figure 6.6c).

The location of the sensor in the finite element model is the same as the experiment as shown in Figure 6.4a and 6.4b. The geometric dimensions of the WDI-AST sensor are shown in Figure 6.6a. The diameter of the bottom surface is 28.6 mm. The single line output defined in the FE model is presented in Figure 6.6b. Fifteen nodes can be observed on the line.

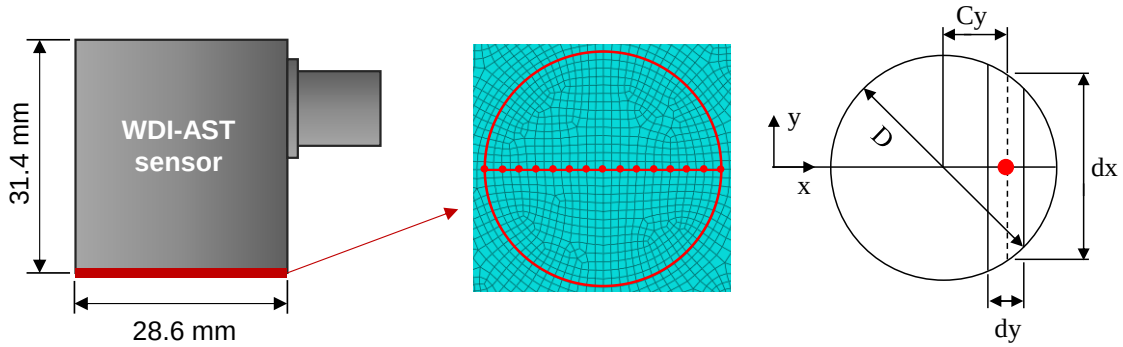

(a) (b) (c)

Figure 6.6 Numerical waveform output setting: (a) geometric dimension of WDI-AST sensor; (b) nodes definition for single line output in FE model; (c) parameters to calculate single line output

AE sensors convert the excitation on the bottom to the electrical signal through the piezoelectric material. Different type of AE sensors has various frequency sensitive range because their piezoelectric material properties are not the same. The stable sensitive frequency range of the WDI-AST sensor is from 100 to 900 kHz. To simulate

the frequency response of the WDI-AST sensor, a bandpass Butterworth filter with the frequency of 100-900 kHz is developed and used to be filtered the U_{sensor} obtained from the finite element model. The filtered waveforms are the final numerical AE waveforms.

In summary, four zones are defined in the finite element model, while each zone has five sub-points. The six excitation sources are implemented in each of the sub-point. In total, 120 numerical AE waveforms can be obtained after the simulation is completed.

6.5.2 Data augmentation of numerical waveforms

One problem of the simulations of acoustic emission is time-consuming since it requires a very small mesh size. In this paper, the average time for the finite element to generate one numerical signal is 26 minutes. 52 hours were spent to generate all the 120 numerical AE signals. It is difficult to produce sufficient data for the source domain based on finite element simulations alone. A data augmentation process is therefore designed to reduce the time to produce a sufficient amount of source domain data. As introduced in Section 2.2.1, GFK is an unsupervised domain adaptation method. It could decrease the difference between two datasets by mapping them into the same low-dimensional subspace and then reconstruct. A new dataset similar to the original one can thereby be obtained. Inspired by this, a data augmentation process is developed by inputting the 120 numerical AE waveforms and the 400 experimental AE waveforms into GFK. By changing the dimension of the low-dimensional subspace, the new datasets with slight differences can be derived. Four different subspaces with four different dimensions were employed to conduct the data augmentation. Finally, 480 waveforms were obtained. The computing time is 23.2 seconds. These waveforms are prepared as the source domain for the improved manifold embedded distribution alignment (introduced in Section 4.3). It

should be mentioned that the data augmentation is unsupervised. No information on labels is used during the process.

6.5.3 Improved manifold embedded distribution alignment

The original MEDA employs k-nearest neighbor (KNN) as the domain classifier in the dynamic distribution alignment process. The domain classifier can derive labels for the target domain, However, the data in source and target domain in this paper are high-dimensional time series with 2048 sample points, the machine learning model such as KNN does not perform very well when dealing with high-dimensional inputs without feature extraction. Previous research has reported that convolutional neural network (CNN) structures such as ResNet, and GoogLeNet work well on the identification of raw acoustic emission signals in the applications such as the monitoring of wear and bridge [49-51]. Therefore, an improved MEDA is developed by replacing the KNN classifier with the ResNet-18. This paper names the improved MEDA as MEDA-ResNet-18. The procedures of MEDA-ResNet-18. can be found in Figure 6.3.

ResNet-18 is a CNN structure with the idea of residuals [52]. Sometimes, the network's performance becomes less reliable when using a deeper structure due to gradient vanishing/explosion problems hindering network convergence. A residual block module was developed and applied in the ResNet-18 structure to overcome this problem by introducing skip connections that enable gradients to flow across several layers. The skip connections cause the outputs to learn a residual mapping.

In this paper, the last FC layer of ResNet-18 is modified to have the class number consistent with the number of zones on the steel plate. Figure 6.7 shows the main structure of the modified ResNet-18.

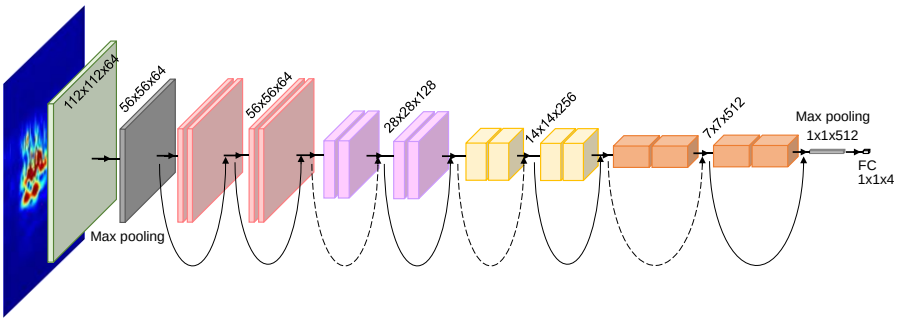

Figure 6.7 The main structure of the modified ResNet-18

The data in the source and target domain after manifold feature learning is converted to continuous wavelet transform (CWT) images and utilized as the input for the ResNet-18 model. The Morse wavelet is selected as the mother wavelet function to conduct CWT. The Fourier transform of Morse wavelet is presented in Eq. (6.12):

$$\Psi_{p,\gamma}(x) = U(x)\alpha_{p,\gamma}x^{\frac{p^2}{\gamma}}e^{-x^{\gamma}} \tag{6.12}$$

where $U(x)$ refers to the unit step, $\alpha_{p,\gamma}$ refers to the normalizing constant, p^2 refers to the time-bandwidth product. γ is the parameter that characterizes the symmetry of the Morse wavelet [53]. In this paper, p^2 and γ was defined as 60 and 3.

6.6 Results and Discussions

6.6.1 Numerical acoustic emission waveforms

The results of the finite element modeling are presented in Figure 6.8. This figure represents expected wave propagation, in terms of displacement, from the point where the excitation source is applied. The wave generated by excitations in four zones is captured by a sensor and converted to numerical AE waveforms according to the method introduced in Section 3.1.

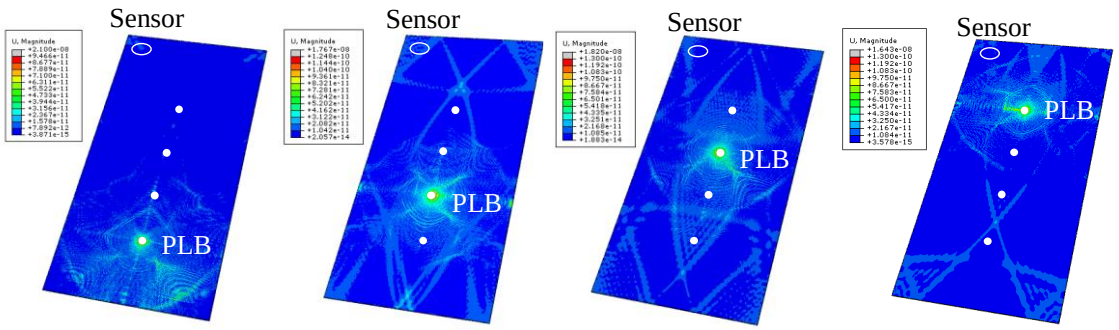

(a) (b) (c) (d)

Figure 6.8. Results of AE simulation: (a) wave propagated from zone 1; (b) wave propagated from zone 2; (c) wave propagated from zone 3; (d) wave propagated from zone 4

The comparison of the numerical AE waveform and the experimental AE waveform from zone 1 is presented in Figure 6.9a and 6.9b. The amplitudes of waveforms are normalized from -1 to 1. Fast Fourier transformations (FFT) analysis was conducted, and the frequency spectrums are shown in Fig. 10c and 10d. it can be noticed that the primary frequency of the experimental signal is in the range of 100-250 kHz (Figure 6.9c). In the numerical FFT magnitude (Figure 6.9d), the primary frequency also lies in 100-250 kHz which is aligned with the experimental signal frequency range. The alignment of the frequency component suggests that the numerical signal can simulate the experimental signal to some extent, however, some relatively obvious differences in the waveforms indicate that the simulation is not entirely consistent with the experiment. The unsupervised domain adaptation method proposed in this paper is utilized to decreases the difference between numerical and experimental AE signals.

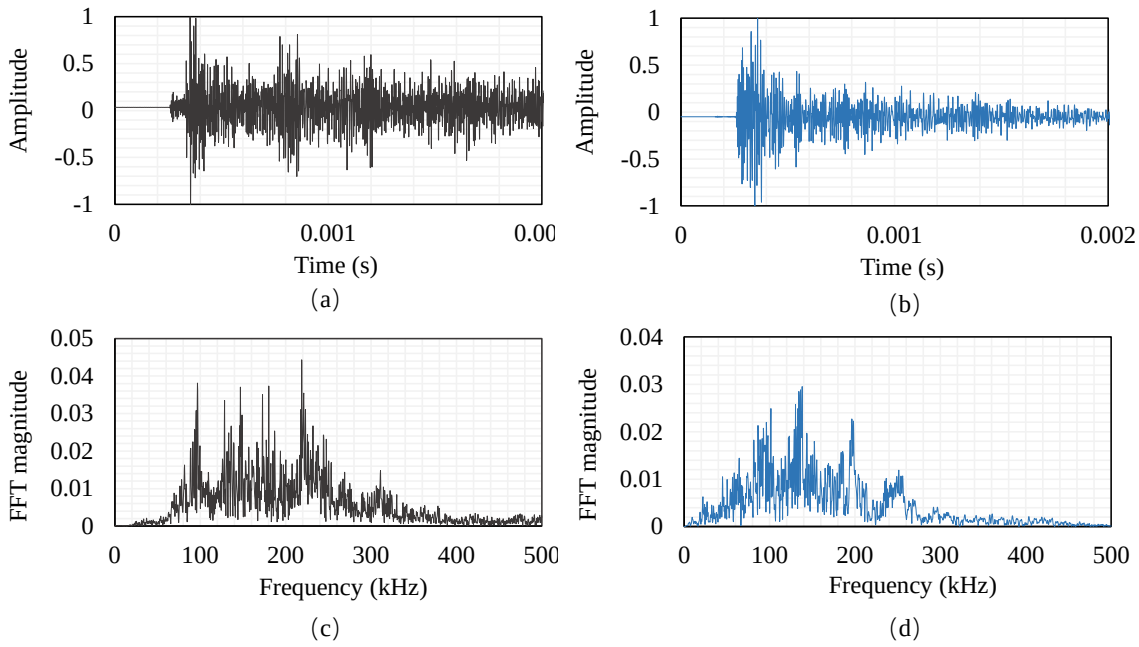

Figure 6.9 Experimental signals versus numerical signals: (a) experimental waveform; (b) numerical waveform; (c) experimental FFT spectrum; (d) numerical FFT spectrum

6.6.2 Unsupervised domain adaptation and transfer learning

The 480 numerical AE waveforms after data augmentation are utilized as the source domain, the 400 AE signals recorded by the experiment are used as the target domain. After manifold feature learning, the waveforms in the reconstructed source and target domain are transformed to CWT coefficients. Fig. 11a and 11c illustrate example CWT coefficients of signals from source and target domain. The wavelet coefficients are scaled between 0 to 1. The Y-axis of the CWT coefficient was then converted to a logarithmic coordinate to present the time-frequency component more clearly. The coefficients were saved as RGB images with the size of 224 × 224 × 3 pixels (Figure 6.10b and 6.10d). The RGB images are employed as the input of the ResNet-18 domain classifier.

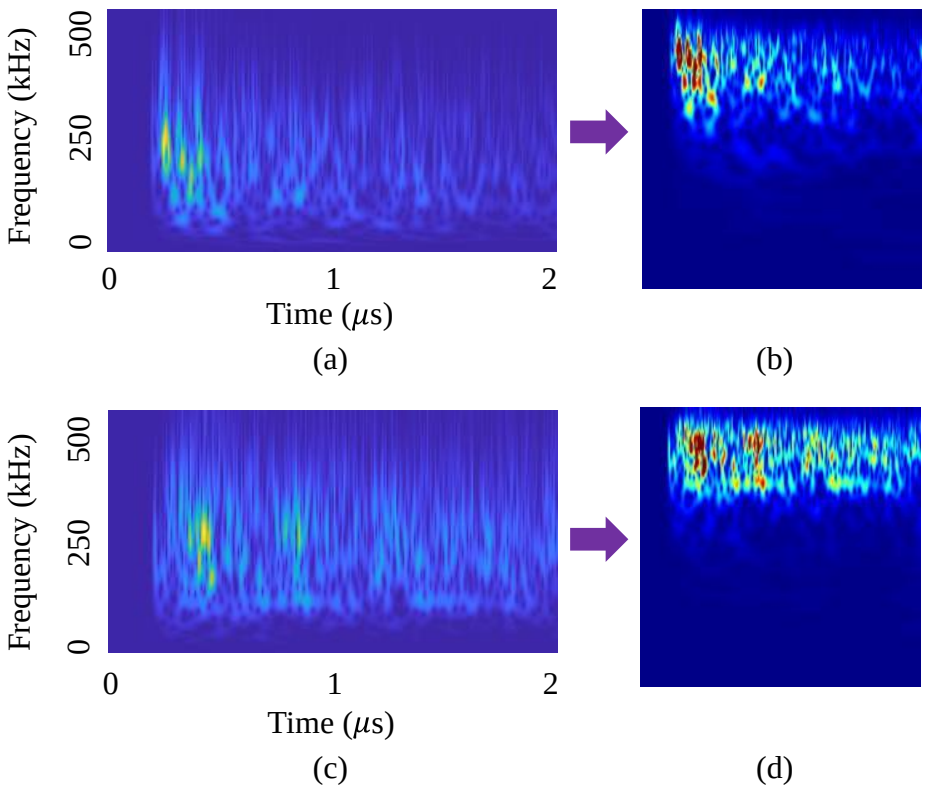

Figure 6.10. Continuous wavelets transform of source and target domain: (a) CWT coefficients of source domain; (b) RGB image of source domain; (c) CWT coefficients of the target domain; (d) RGB image of the target domain

The CWT images in the source domain are employed to train the CNN model in MEDA-ResNet-18. 90% of the CWT images in the source domain are randomly selected as a training dataset. A validation dataset is constructed by the remaining 10% of the CWT images. The computing of the CNN model is conducted on a workstation with a CPU-Intel i7-6700 3.40 GHz, 32 GB RAM, and an Nvidia GPU-GTX1080. For the ResNet-18 deployed in this paper, the gradient descent optimization was conducted using the Adaptive moment estimation (Adam) method [54]. The minibatch size was 32, the learning rate was 0.0001. Figure 6.11a and 6.11b presents the accuracy and loss curves of the training and validation datasets from iteration 1 to 30. Both training and validation datasets get 100% accuracy by the end of iteration 30, and the losses are close to 0. The

training and validation reach the convergence around iteration 5, and the curves are stable after converging.

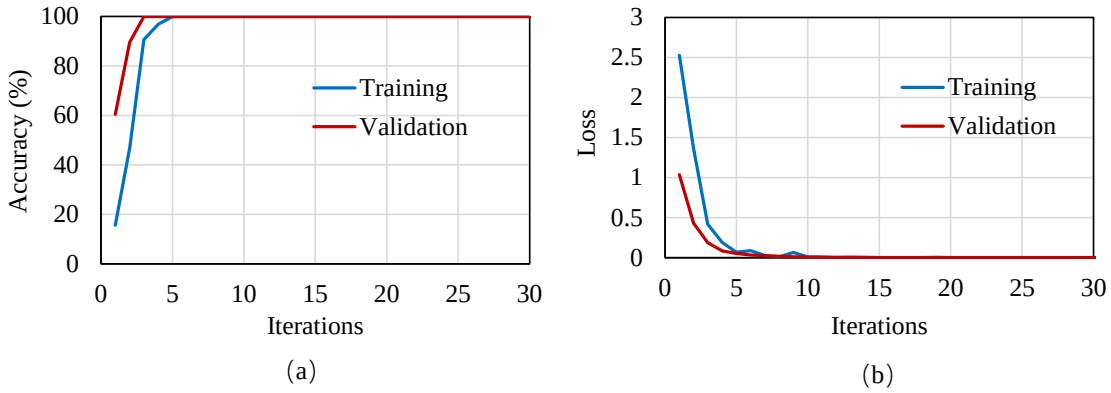

Figure 6.11 Training and validation curves: (a) accuracy curves; (b) loss curves

After the ResNet-18 model is trained by the source domain, the CWT images in the target domain are inputted into the trained model to derive the prediction label. As prementioned, the derived label may not be accurate. The optimized prediction label can be obtained by dynamic distribution alignment after several iterations are conducted. The optimized prediction label is the final output of the MEDA-ResNet-18. In addition to the iterations number, the dimension of the low-dimensional manifold space d utilized during the manifold feature learning is another factor that can influence the result of MEDA-ResNet-18. To acquire the appropriate iterations number and dimension of manifold space, a trial-and-error test is conducted. The results are presented in Figure 6.12.

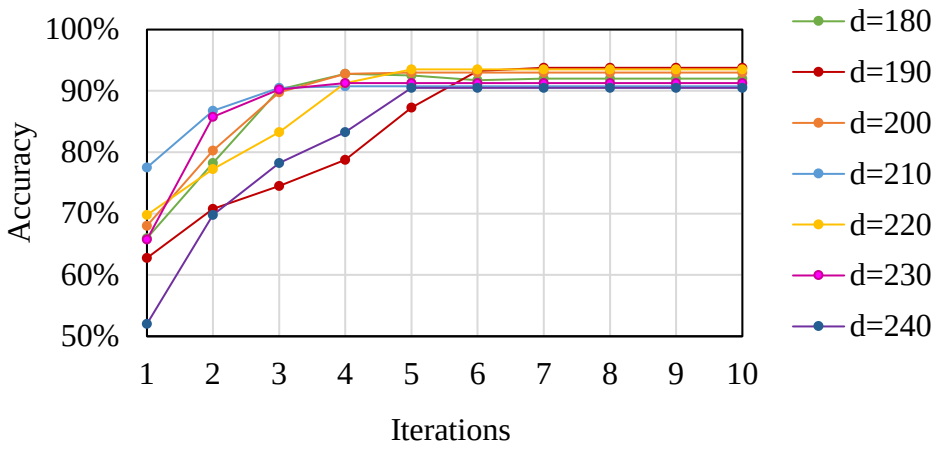

Figure 6.12 Iteration of dynamic distribution alignment in MEDA-ResNet-18

Seven manifold space dimensions (180, 190, 200, 210, 220, 230, and 240) are utilized in MEDA-ResNet-18. For all the dimensions, the accuracies of the predicted label increased to over 90% after iteration 6. The accuracies remain almost constant as the number of iterations increases to 10. It indicates that the iteration number should at least be 6. The highest accuracy (93.8%) can be observed when the manifold space dimension is 190. Therefore, 190 is selected as the optimum manifold space dimension for MEDA-ResNet-18.

6.6.3 Comparison and discussion

To evaluate the effectiveness of the proposed TL approach, six scenarios are designed, and their corresponding accuracies are compared. Scenario 1 is training and testing with 480 numerical waveforms in the source domain. Scenario 2 is training and testing with 400 experimental waveforms in the target domain. Scenario 3 is training on the source domain and testing on the target domain without unsupervised domain adaptation. Scenario 4 is training on the source domain and testing on the target domain with GFK manifold feature learning only, no dynamic distribution alignment is conducted. Scenario 5 is training on the source domain and testing on the target domain

with the original MEDA. Scenario 6 is training on the source domain and testing on the target domain with improved MEDA-ResNet-18.

The goal of scenarios 1 and 2 is to study the performance of AE source localization on the steel specimen if a sufficient number of well-labeled training data is available. ResNet-18 is employed in the two scenarios. The training, validation, and testing ratio are 80%, 10%, and 10%. The results of scenarios 1 and 2 are shown in the confusion matrixes in Figure 6.13. The accuracy is 100% for training and testing on the 480 numerical waveforms in the source domain. The accuracy is 97.5 % for the 400 numerical waveforms in the source domain. Results indicating that a good localization performance can be obtained if labeled training data can be provided.

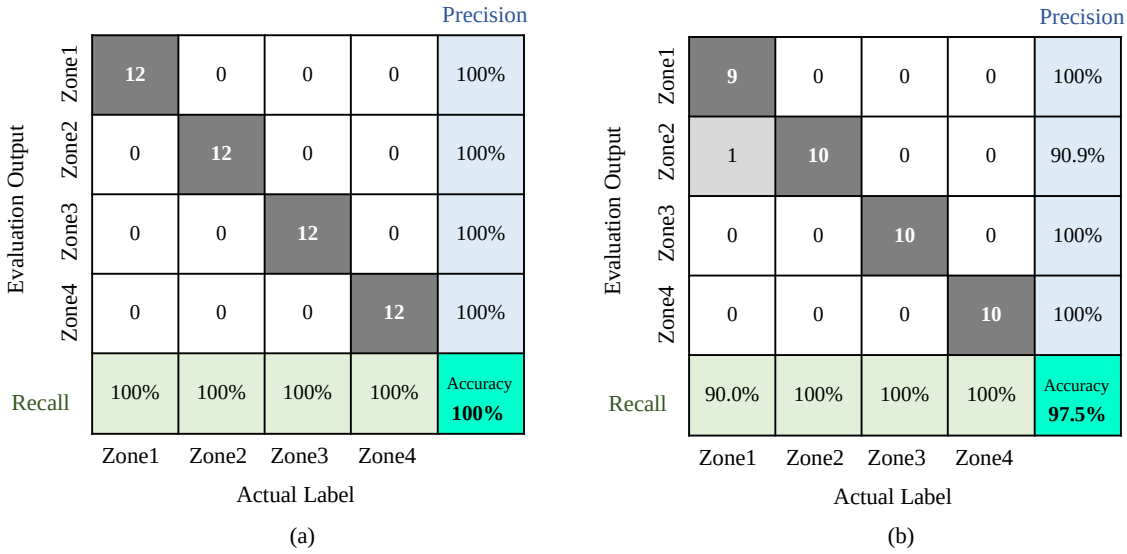

Figure 6.13 Source localization accuracy: (a) scenario 1; (b) scenario 2

The objective of scenarios 3 to 6 is to investigate the performance of TL when no labeled training AE waveforms are available. The results are presented in the confusion matrixes in Figure 6.14. The numbers of AE data that are correctly localized in their corresponding zones are shown in the main diagonal of the confusion matrix. When using

480 numerical AE waveforms as the source domain, and using 400 experimental AE waveforms as target domain, meanwhile no unsupervised domain adaptation method is applied (scenarios 3), a low prediction accuracy (43.0%) is observed (Figure 6.14a). When using GFK manifold feature learning as the unsupervised domain adaptation method, the prediction accuracy increases from 43.0% to 77.5% (Figure 6.14b). The accuracy further increases to 89.8% when the unsupervised domain adaptation method is changed to MEDA. Finally, the highest prediction accuracy (93.8%) can be acquired if the improved MEDA-ResNet-18 is utilized (Figure 6.14d). By observing the results of the four scenarios, it can be noticed that the prediction accuracy of the target domain significantly increases if unsupervised domain adaptation is implemented. Among the three unsupervised domain adaptation methods, the improved MEDA-ResNet-18 proposed in this paper has the best performance.

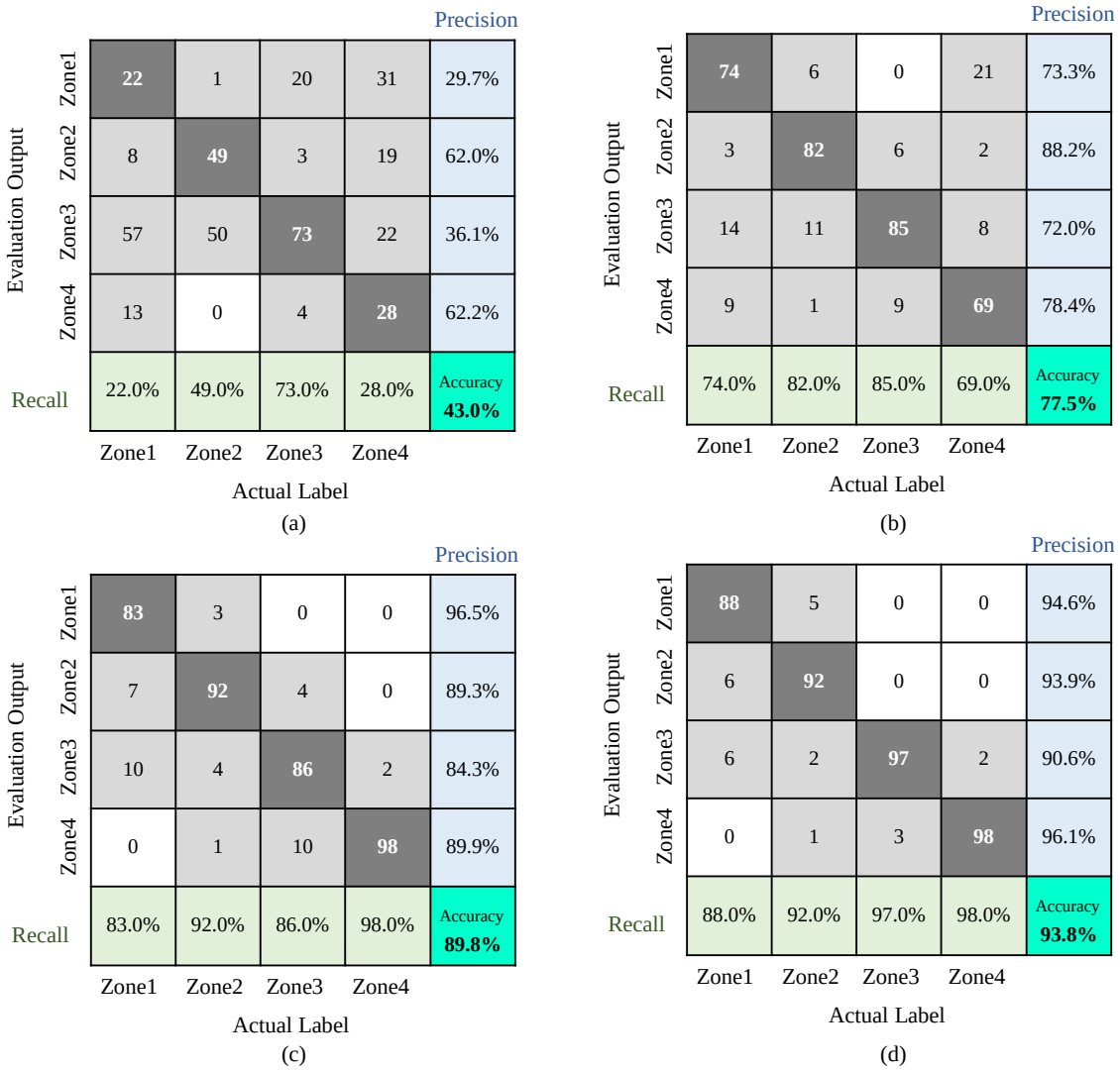

Figure 6.14. Source localization accuracy: (a) scenario 1- no unsupervised domain adaptation; (b) scenario 2- using GFK manifold feature learning; (c) scenario 3- using MEDA; (d) scenario 4- using MEDA-ResNet-18

In addition to accuracy, precision rate, and recall rate for each class are usually implemented as the metrics to evaluate the performance of classification in each class [55]. The value of precision rate and recall rate is obtained by the following equations:

$$Recall = \frac{TP}{TP+FN} \tag{6.13}$$

$$Precision = \frac{TP}{TP+FP} \tag{6.14}$$

Where TP refers to true positives, which means the number of samples that correctly classify into the corresponding class, FP refers to false positives, which is the number of samples that do not belong to the class but are classified into the class by error. FN refers to false negatives, the number of samples that belong to the class but are classified into the other classes by error.

Precision and recall influence each other. A class with high precision usually has a low recall and vice versa [55]. To comprehensively evaluate the efficiency of the classifier in each class, the F1-score can be employed. F1-score, also referred to as the balanced F score, is defined as the harmonic mean of precision and recall [56]. It can be provided by Eq. (6.15):

$$F1 = \frac{2\times Precision\times Recall}{Precision+Recall} = \frac{2TP}{2TP+FP+FN} \tag{6.15}$$

The comparison of the three metrics, precision rates, recall rate, and F1-score for the four zones of scenarios 3-6 are presented in Figure 6.15. The figure indicates that the three metrics of scenario 6 using improved MEDA-ResNet-18 are generally the highest, particularly much higher than scenario 3 using no unsupervised domain adaptation. It can be noticed that the three metrics obtained by scenario 6 are relatively stable while the other three scenarios show obvious variety in different zones. These observations of precision rates, recall rate, and F1-score suggest scenario 6 using the improved MEDA-ResNet-18 presents the best performance. This is aligned with the observation of accuracy.

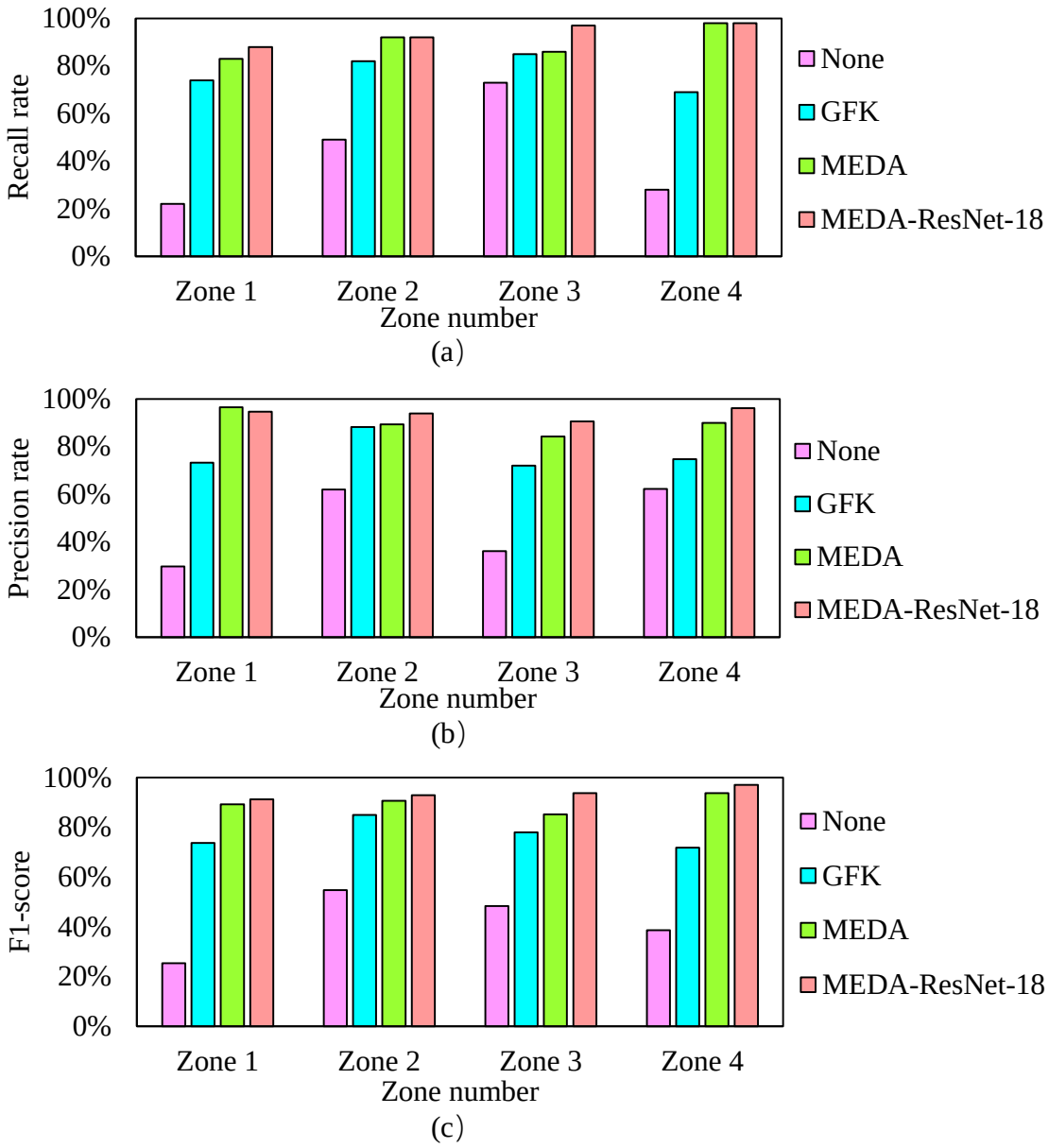

Figure 6.15 Comparison of classification performance in each zone: (a) recall rate; (b) precision rate; (c) F1-score

6.7 Conclusion and summary

This paper proposes a TL approach for the localization of acoustic emission without historical AE signals for training. A finite element model is developed to simulate the stress wave propagation and generate numerical AE signals. The distribution difference of the numerical and the realistic AE signals is reduced by an improved

MEDA-ResNet-18 unsupervised domain adaptation method, and the source localization results of the realistic AE signals are acquired. A 304 stainless steel plate was used as an experimental specimen to collect AE signals and validate the proposed approach. The main conclusions of the paper are summarized as follows:

The source localization approach using the ResNet-18 model is validated by respectively using the collected experimental AE signals and numerical signals. Results indicate that a good localization performance can be observed when the labeled training data is available.

The numerical signals generated by the finite element model are employed as the labeled source domain. The experimental AE signals are adopted as the unlabeled target domain. The TL source localization accuracies of the scenarios that using no unsupervised domain adaptation method (43.0%), using the GFK method (77.5%), using MEDA (89.8%), and using the improved MEDA-ResNet-18 (93.8%) are compared and discussed. The results suggest that using the unsupervised domain adaptation method can significantly increase the localization accuracy on the target domain. The best performance is obtained by the improved MEDA-ResNet-18 (93.8%). Recall rate, precision rate, and F1-score suggest that the improved MEDA-ResNet-18 has the optimum performance of localization for each individual zone.

The frequency content of the signal generated by the finite element model is similar to the values attributed to the experimental AE signal. However, the similarity between the waveforms of the numerical and experimental AE signal is not significant. Future work can be the improvement of the model by developing a surface output that is more realistic than the single line output adopted in this paper.

6.8 Acknowledgments

This research was partially supported by Electric Power Research Institute (EPRI) under project number 1-108781. The views and opinions of authors expressed herein do not necessarily state or reflect the opinions of the funding agencies.

6.9 References

[1] Y. Zhao, F. Zhou, J. Yao, S. Dong, N. Li,2015. Erosion–corrosion behavior and corrosion resistance of AISI 316 stainless steel in flow jet impingement, Wear 328 464-474.

[2] J. Bhandari, F. Khan, R. Abbassi, V. Garaniya, R. Ojeda,2015. Modelling of pitting corrosion in marine and offshore steel structures–A technical review, Journal of Loss Prevention in the Process Industries 37 39-62.

[3] M. Sun, Z. Song, X. Jiang, J. Pan, Y. Pang,2017. Learning pooling for convolutional neural network, Neurocomputing 224 96-104.

[4] D. Aggelis, E. Kordatos, T. Matikas,2011. Acoustic emission for fatigue damage characterization in metal plates, Mechanics Research Communications 38 106-110.

[5] D. Liao, S.P. Zhu, J.A. Correia, A.M. De Jesus, F. Berto,2020. Recent advances on notch effects in metal fatigue: A review, Fatigue & Fracture of Engineering Materials & Structures 43 637-659.

[6] D. Li, K.S.C. Kuang, C.G. Koh,2017. Fatigue crack sizing in rail steel using crack closure-induced acoustic emission waves, Measurement Science and Technology 28 065601.

[7] R. Anay, V. Soltangharaei, L. Assi, T. DeVol, P. Ziehl,2018. Identification of damage mechanisms in cement paste based on acoustic emission, Construction and Building Materials 164 286-296.

[8] L. Assi, V. Soltangharaei, R. Anay, P. Ziehl, F. Matta,2018. Unsupervised and supervised pattern recognition of acoustic emission signals during early hydration of Portland cement paste, Cement and Concrete Research 103 216-225.

[9] V. Soltangharaei, R. Anay, N.W. Hayes, L. Assi, Y. Le Pape, Z.J. Ma, P. Ziehl,2018. Damage mechanism evaluation of large-scale concrete structures affected by alkali-silica reaction using acoustic emission, Applied Sciences 8 2148.

[10] V. Soltangharaei, R. Anay, L. Ai, E.R. Giannini, J. Zhu, P. Ziehl,2020. Temporal Evaluation of ASR Cracking in Concrete Specimens Using Acoustic Emission, Journal of Materials in Civil Engineering 32 04020285.

[11] R. Anay, A. Lane, D.V. Jáuregui, B.D. Weldon, V. Soltangharaei, P. Ziehl,2020. On-Site Acoustic-Emission Monitoring for a Prestressed Concrete BT-54 AASHTO Girder Bridge, Journal of Performance of Constructed Facilities 34 04020034.

[12] L. Ai, V. Soltangharaei, P. Ziehl,2021. Evaluation of ASR in Concrete Using Acoustic Emission and Deep Learning, Nuclear Engineering and Design.

[13] E.D. Dzaye, G. De Schutter, D.G. Aggelis,2020. Monitoring early-age acoustic emission of cement paste and fly ash paste, Cement and Concrete Research 129 105964.

[14] D. Li, K.S.C. Kuang, C.G. Koh,2018. Rail crack monitoring based on Tsallis synchrosqueezed wavelet entropy of acoustic emission signals: A field study, Structural Health Monitoring 17 1410-1424.

[15] M.R. Pearson, M. Eaton, C. Featherston, R. Pullin, K. Holford,2017. Improved acoustic emission source location during fatigue and impact events in metallic and composite structures, Structural Health Monitoring 16 382-399.

[16] Y. Sai, M. Jiang, Q. Sui, S. Lu, L. Jia,2016. Multi-source acoustic emission localization technology research based on FBG sensing network and time reversal focusing imaging, Optik 127 493-498.

[17] Y. Yan, Y. Shen, X. Cui, Y. Hu,2018. Localization of multiple leak sources using acoustic emission sensors based on MUSIC algorithm and wavelet packet analysis, IEEE Sensors Journal 18 9812-9820.

[18] M.I. Jordan, T.M. Mitchell,2015. Machine learning: Trends, perspectives, and prospects, Science 349 255-260.

[19] I. Goodfellow, Y. Bengio, A. Courville,2016. Machine learning basics, Deep learning 1 98-164.

[20] V. Cherkassky, Y. Ma,2004. Practical selection of SVM parameters and noise estimation for SVM regression, Neural networks 17 113-126.

[21] I.W. Tsang, J.T. Kwok, P.-M. Cheung, N. Cristianini,2005. Core vector machines: Fast SVM training on very large data sets, Journal of Machine Learning Research 6.

[22] H. Zhang, A.C. Berg, M. Maire, J. Malik, SVM-KNN: Discriminative nearest neighbor classification for visual category recognition, IEEE, 2006, 2126-2136.

[23] M. Belgiu, L. Drăguţ,2016. Random forest in remote sensing: A review of applications and future directions, ISPRS journal of photogrammetry and remote sensing 114 24-31.

[24] R. Sun, Y. Chen, A. Dubey, P. Pugliese,2021. Hybrid electric buses fuel consumption prediction based on real-world driving data, Transportation Research Part D: Transport and Environment 91 102637.

[25] L. Ai, V. Soltangharaei, R. Anay, M.J. van Tooren, P. Ziehl, Data-Driven Source Localization of Impact on Aircraft Control Surfaces, IEEE, 2020, 1-10.

[26] I. Goodfellow, Y. Bengio, A. Courville, Y. Bengio, Deep learning, MIT press Cambridge, 2016.

[27] A. Ebrahimkhanlou, B. Dubuc, S. Salamone,2019. A generalizable deep learning framework for localizing and characterizing acoustic emission sources in riveted metallic panels, Mechanical Systems and Signal Processing 130 248-272.

[28] L. Ai, V. Soltangharaei, M. Bayat, B. Greer, P. Ziehl,2021. Source localization on large-scale canisters for used nuclear fuel storage using optimal number of acoustic emission sensors, Nuclear Engineering and Design 375 111097.

[29] L. Ai, V. Soltangharaei, M. Bayat, M. van Tooren, P. Ziehl,2021. Detection of impact on aircraft composite structure using machine learning techniques, Measurement Science and Technology.

[30] S.J. Pan, Q. Yang,2009. A survey on transfer learning, IEEE Transactions on knowledge and data engineering 22 1345-1359.

[31] D. Li, Y. Wang, W.-J. Yan, W.-X. Ren,2020. Acoustic emission wave classification for rail crack monitoring based on synchrosqueezed wavelet

transform and multi-branch convolutional neural network, Structural Health Monitoring 1475921720922797.

[32] S.-X. Chen, L. Zhou, Y.-Q. Ni, X.-Z. Liu,2020. An acoustic-homologous transfer learning approach for acoustic emission–based rail condition evaluation, Structural Health Monitoring 1475921720976941.

[33] M. Long, H. Zhu, J. Wang, M.I. Jordan,2016. Unsupervised domain adaptation with residual transfer networks, arXiv preprint arXiv:1602.04433.

[34] J. Wang, W. Feng, Y. Chen, H. Yu, M. Huang, P.S. Yu, Visual domain adaptation with manifold embedded distribution alignment, 2018, 402-410.

[35] Z. Zhang, J. Wang, H. Zha,2011. Adaptive manifold learning, IEEE transactions on pattern analysis and machine intelligence 34 253-265.

[36] B. Gong, Y. Shi, F. Sha, K. Grauman, Geodesic flow kernel for unsupervised domain adaptation, IEEE, 2012, 2066-2073.

[37] M. Arbel, A. Korba, A. Salim, A. Gretton,2019. Maximum mean discrepancy gradient flow, arXiv preprint arXiv:1906.04370.

[38] B. Quanz, J. Huan, Large margin transductive transfer learning, 2009, 1327-1336.

[39] S. Ben-David, J. Blitzer, K. Crammer, F. Pereira,2007. Analysis of representations for domain adaptation, Advances in neural information processing systems 19 137.

[40] C.U. Grosse, M. Ohtsu, Acoustic emission testing, Springer Science & Business Media, 2008.

[41] T. Boczar, M. Lorenc,2004. Determining the repeatability of acoustic emission generated by the Hsu-Nielsen calibrating source, Molecular and quantum Acoustics 25 177-192.

[42] B. Hosten, M. Castaings,2005. Finite elements methods for modeling the guided waves propagation in structures with weak interfaces, The Journal of the Acoustical Society of America 117 1108-1113.

[43] E.H. Saenger, N. Gold, S.A. Shapiro,2000. Modeling the propagation of elastic waves using a modified finite-difference grid, Wave motion 31 77-92.

[44] M.G. Sause, S. Richler,2015. Finite element modelling of cracks as acoustic emission sources, Journal of nondestructive evaluation 34 4.

[45] M.G. Sause, M.A. Hamstad, S. Horn,2012. Finite element modeling of conical acoustic emission sensors and corresponding experiments, Sensors and Actuators A: Physical 184 64-71.

[46] L. Ai, B. Greer, J. Hill, V. Soltangharaei, R.A.P. Ziehl, Finite element modeling of acoustic emission in dry cask storage systems generated by cosine bell sources, AIP Publishing LLC, 2019, 130001.

[47] N. van Rijn,2017. Investigating the Behaviour of Acoustic Emission Waves Near Cracks: Using the Finite Element Method.

[48] J.A. Cuadra, A Computational Modeling Approach of Fracture-Induced Acoustic Emission, Drexel University, 2015.

[49] H. Xin, L. Cheng, R. Diender, M. Veljkovic,2020. Fracture acoustic emission signals identification of stay cables in bridge engineering application using deep transfer learning and wavelet analysis, Advances in Bridge Engineering 1 1-16.

[50] F. König, G. Jacobs, A. Stratmann, D. Cornel, Fault detection for sliding bearings using acoustic emission signals and machine learning methods, IOP Publishing, 2021, 012013.

[51] F. König, C. Sous, A.O. Chaib, G. Jacobs,2021. Machine learning based anomaly detection and classification of acoustic emission events for wear monitoring in sliding bearing systems, Tribology International 155 106811.

[52] K. He, X. Zhang, S. Ren, J. Sun, Deep residual learning for image recognition, 2016, 770-778.

[53] J.M. Lilly, S.C. Olhede,2012. Generalized Morse wavelets as a superfamily of analytic wavelets, IEEE Transactions on Signal Processing 60 6036-6041.

[54] D.P. Kingma, J. Ba,2014. Adam: A method for stochastic optimization, arXiv preprint arXiv:1412.6980.

[55] M. Buckland, F. Gey,1994. The relationship between recall and precision, Journal of the American society for information science 45 12-19.

[56] H. Huang, H. Xu, X. Wang, W. Silamu,2015. Maximum F1-score discriminative training criterion for automatic mispronunciation detection, IEEE/ACM Transactions on Audio, Speech, and Language Processing 23 787-797.

Chapter 7

Summary and Conclusion

7.1 Summary

Steel and concrete are significant construction materials of infrastructures. The infrastructural components are subject to structural damage after long-term use. SCC and ASR are the primary mechanisms of damage in steel and concrete structures [1; 2]. The monitoring and evaluation of SCC and ASR damages in structures are needed to ensure the serviceability and integrity of infrastructures such as stainless steel spent fuel storage canisters and concrete components in bridges. The AE structural health monitoring could be used for the monitoring of SCC [3-6] and ASR [7-11]. However, there are several challenges and scientific gaps that exist in the path toward developing the AE monitoring approached for the SCC damage in the spent fuel storage canister and the ASR damage in concrete nuclear containment. Some of the gaps are addressed in this dissertation. One of the gaps in the AE monitoring of spent fuel storage canister is the lack of investigation about the feasibility of AE monitoring to detect the SCC damage in a large-scale stainless steel spent fuel storage canister. Furthermore, when applying AE monitoring in the realistic spent fuel storage canister. The canisters are huge and are stored in a concrete overpack. The available area for sensor attachment is limited. It is difficult to employ an AE sensor array around the cracking region to detect the location of a crack [12]. There is another gap for the AE monitoring of ASR in concrete components. The selection of the appropriate AE features for ASR analysis was generally based on experience and very challenging especially for complex data sets. Therefore, an automatic approach is required to extract features directly from raw AE data and find potential patterns in the complex data sets. Therefore, four different studies are defined to approach the primary goal.

In the first study, AE monitoring was conducted on a full-scale 304H stainless-steel plate specimen which was made of similar length and thickness to a realistic SCSS canister. The condition to induce SCC was provided by applying tensile stress at the notch on the plate surface which was exposed to the Potassium Tetrathionate solution. The waveforms and the frequency content of the AE signals acquired in the test were studied. Furthermore, a finite element (FE) model was developed to generate numerical AE signals for the purpose of the AE sensor selection for the field application. The AE signals obtained from the test and the FE model were compared and discussed.

The second study presents the approaches that can localize SCC sources by minimal AE sensor. To achieve this goal, three machine learning techniques (artificial neural network, random forest, stacked autoencoders) were adopted to improve the conventional source localization approach. In this paper, source localization is treated as a classification problem. The testing specimen was divided into multiple zones and located the AE signals to their corresponding zones. The AE signals were processed to create two datasets: a dataset consisting of AE parametric features and a dataset consisting of AE waveforms. Source localization approaches using artificial neural networks, random forest, and stacked autoencoders were trained and tested based on the datasets.

In the third study. The deep learning algorithms was employed to evaluate the ASR progress. ASR was monitored by AE in a concrete specimen, which was cast with reactive coarse aggregates and reinforced by steel rebars. The AE signals recorded during the experiment were filtered and divided into two classes. Two deep learning algorithms

of convolutional neural network (CNN) and stacked autoencoder were employed to classify the AE signals into the corresponding classes.

The fourth study proposed a transfer learning approach for AE source localization on the stainless-steel structures when no historical labeled AE signals are available for training. A finite element model is developed to generate numerical AE signals for the training. Unsupervised domain adaptation technology is utilized to reduce the distribution difference between the numerical and the realistic AE signals and derived the localization results of the unlabeled realistic AE signals.

7.2 Conclusion of each study

7.2.1 Structural Health Monitor of Stainless-Steel Structures for Spent Nuclear Fuel Storage Using Acoustic Emission

In this study, the full-scale steel plate which simulates the real-sized DCSS canister was studied for the AE monitoring of stress corrosion cracking (SCC). Four WDI sensors were attached near the cracks and seven R3I sensors were attached with varying distances from the cracks. The frequency analysis and source localization of SCC events was conducted. Furthermore, a FE model was developed to acquire numerical AE signals. The FE model was compared to the experimental signals. Pertinent conclusions and observations are as follows:

- The R3I sensors attached on the bolted plates away from the crack extension events were able to capture the events, and the decrease in amplitude across the contact surface was minimal. This indicates that attaching resonant AE sensors on the bottom support structures of the DCSS canister for the monitoring of SCC is feasible

- A frequency range of the cracking events captured close to the notch showed that genuine hits fell within a range of 100-300 kHz, whereas cracking events captured away from the crack extension events showed that genuine hits fell within a range of 30-100 kHz. This information is valuable for the selection of resonant AE sensors for field applications.
- The frequency content of waves generated by the FE model is similar to the values attributed to the experimental AE data both from the WDI and R3I sensors. The model may be useful for the selection of sensor types located far from crack extension events.

7.2.2 Source Localization on Large-Scale Canisters for Used Nuclear Fuel Storage Using Optimal Number of Acoustic Emission Sensors

This study considered three machine learning approaches to localize simulated SCC AE sources on a 304 stainless steel specimen, which has a similar length and thickness with the realistic DCSS canister. ANN, random forest, and stacked autoencoders were used. This study aims to detect and localize AE sources with only one sensor attached opposite the source. To collect a sufficient number of AE data for training and testing, AE sources were simulated on the specimen by conducting Hsu-Nielsen pencil lead break tests. The main conclusions are as follows:

- The performance of three machine learning approaches was compared. The stacked autoencoders have the best performance (97.8% accuracy versus 91.5% and 80.0%). Although the training time required for stacked autoencoders is more than the other two (352.89 seconds versus 0.02

seconds and 0.01second), their computing time required for testing is similar.

- Feature selection can be achieved by running a random forest. The random forest model indicated that the AE parametric features "peak frequency", "rise time", "initial frequency", "amplitude", "duration", "PCNTS" and "counts" made up 75% of the cumulative importance for all 15 features. Using them as the input for random forest leads to increasing accuracy and decreasing computational time.
- The F1-scores indicated that the performance of stacked autoencoders in various zones is the best among the three. Moreover, good performance in terms of stability in various zones was observed in stacked autoencoders while ANN resulted in more variability.

7.2.3 Evaluation of ASR in Concrete Using Acoustic Emission and Deep Learning

The evaluation method based on deep learning is proposed to assess the condition of ASR progress in concrete structures. To verify the effectiveness of the proposed method, a concrete specimen with reactive coarse and reinforcements was cast and placed in a chamber for 300 days to accelerate the ASR by providing high temperature and humidity. AE sensors were affixed on the specimen surfaces to acquire stress waves emitted during the ASR due to cracking. The ASR expansion was measured using DEMEC gauge on a regular basis. A CNN and stacked autoencoder models were trained using the AE data for classification purposes and determining ASR volumetric strain ranges. The main conclusions of the paper are summarized as follows:

- Both CNN and stacked autoencoder can classify the AE signals to their ASR phases with acceptable accuracy, while a higher accuracy was observed in the classification using the CNN than stacked autoencoder. In addition, using AE signals from a single sensor leads to a better performance of classification than using signals captured by all the sensors.
- The F1-scores indicated that the classification result of CNN using signals from a single sensor has the best performance in both phases (classes). Moreover, good consistency of F1-scores between two phases was observed for the CNN models.
- Considering computing time, global accuracy, and classifier performance in two phases, the CNN model using the data from a single sensor is the most efficient model among the evaluated models to monitor the temporal evolution of the concrete specimen affected by ASR.

7.2.4 A Transfer Learning Approach for Acoustic Emission Localization on Stainless Steel Structure Using Numerical Simulation and Unsupervised Domain Adaptation

This study proposes a TL approach for the localization of acoustic emission without historical AE signals for training. A finite element model is developed to simulate the stress wave propagation and generate numerical AE signals. The distribution difference of the numerical and the realistic AE signals is reduced by an improved MEDA-ResNet-18 unsupervised domain adaptation method, and the source localization results of the realistic AE signals are acquired. A 304 stainless steel plate was used as an

experimental specimen to collect AE signals and validate the proposed approach. The main conclusions of the paper are summarized as follows:

- The source localization approach using the ResNet-18 model is validated by respectively using the collected experimental AE signals and numerical signals. Results indicate that a good localization performance can be observed when the labeled training data is available.
- The numerical signals generated by the finite element model are employed as the labeled source domain. The experimental AE signals are adopted as the unlabeled target domain. The TL source localization accuracies of the scenarios that using no unsupervised domain adaptation method (43.0%), using the GFK method (77.5%), using MEDA (89.8%), and using the improved MEDA-ResNet-18 (93.8%) are compared and discussed. The results suggest that using the unsupervised domain adaptation method can significantly increase the localization accuracy on the target domain. The best performance is obtained by the improved MEDA-ResNet-18 (93.8%). Recall rate, precision rate, and F1-score suggest that the improved MEDA-ResNet-18 has the optimum performance of localization for each individual zone.
- The frequency content of the signal generated by the finite element model is similar to the values attributed to the experimental AE signal. However, the similarity between the waveforms of the numerical and experimental AE signal is not significant. Future work can be the improvement of the

model by developing a surface output that is more realistic than the single line output adopted in this paper.

The above conclusions are based on the initial research results. More research should be conducted regarding this subject.

7.3 Recommendation and future work

The primary goal of this dissertation is to develop an intelligent acoustic emission (AE) monitoring approach for structural health monitoring of infrastructures such as spent fuel storage canister and bridge concrete component without historical AE signals to train the artificial intelligent models. Some challenges were addressed in this dissertation; however, more research should be conducted before starting to implement the approach in the field.

In this dissertation, the single sensor source localization of SCC was investigated using simulated Hsu-Nielsen signals. The Hsu-Nielsen signals can simulate the CSS signals to some context. However, a long-term corrosion experiment could be conducted in the future to collect a sufficient number of SCC signals to investigate the single sensor localization approach using artificial intelligence algorithms.

The frequency content of the signal generated by the finite element model is similar to the values of the experimental AE signal. However, the similarity between the waveforms of the numerical and experimental AE signal is not significant. Future work can be the improvement of the model by utilizing a novel excitation source function. In addition, developing a surface output that is more realistic than the single line output in this dissertation could be the subject of future research.

The effectiveness of more unsupervised domain adaptation method can be investigated for the proposed transfer learning localization approach in the future. And the application of the transfer learning localization approach in other materials such as concrete and composite could also be the focus of future work.

7.4 References

[1] J.W. Hill, Acoustic Emission Detection in 304H Stainless Steel due to Intergranular Stress Corrosion Cracking, University of South Carolina, 2018.

[2] V. Soltangharaei, R. Anay, L. Ai, E.R. Giannini, J. Zhu, P. Ziehl,2020. Temporal evaluation of ASR cracking in concrete specimens using acoustic emission, Journal of Materials in Civil Engineering 32 04020285.

[3] D. Li, W. Yang, W. Zhang,2017. Cluster analysis of stress corrosion mechanisms for steel wires used in bridge cables through acoustic emission particle swarm optimization, Ultrasonics 77 22-31.

[4] D. Li, M. Tan, S. Zhang, J. Ou,2018. Stress corrosion damage evolution analysis and mechanism identification for prestressed steel strands using acoustic emission technique, Structural Control and Health Monitoring 25 e2189.

[5] Z. Zhang, X. Wu, J. Tan,2019. In-situ monitoring of stress corrosion cracking of 304 stainless steel in high-temperature water by analyzing acoustic emission waveform, Corrosion Science 146 90-98.

[6] V. Soltangharaei, J. Hill, L. Ai, R. Anay, B. Greer, M. Bayat, P. Ziehl,2020. Acoustic emission technique to identify stress corrosion cracking damage, Structural Engineering and Mechanics 75 723-736.

[7] M. Abdelrahman, M.K. ElBatanouny, P. Ziehl, J. Fasl, C.J. Larosche, J. Fraczek,2015. Classification of alkali–silica reaction damage using acoustic emission: A proof-of-concept study, Construction and Building Materials 95 406-413.

[8] Y. Farnam, M.R. Geiker, D. Bentz, J. Weiss,2015. Acoustic emission waveform characterization of crack origin and mode in fractured and ASR damaged concrete, Cement and Concrete Composites 60 135-145.

[9] T. Lokajíček, R. Přikryl, Š. Šachlová, A. Kuchařová,2017. Acoustic emission monitoring of crack formation during alkali silica reactivity accelerated mortar bar test, Engineering Geology 220 175-182.

[10] F. Weise, K. Voland, S. Pirskawetz, D. Meinel, Innovative measurement techniques for characterising internal damage processes in concrete due to ASR, 2012, 20-25.

[11] V. Soltangharaei, R. Anay, N.W. Hayes, L. Assi, Y. Le Pape, Z.J. Ma, P. Ziehl,2018. Damage mechanism evaluation of large-scale concrete structures affected by alkali-silica reaction using acoustic emission, Applied Sciences 8 2148.

[12] L. Ai, V. Soltangharaei, M. Bayat, B. Greer, P. Ziehl,2021. Source localization on large-scale canisters for used nuclear fuel storage using optimal number of acoustic emission sensors, Nuclear Engineering and Design 375 111097.

Appendix A

Copyright Permission

The paper entitled “Source Localization on Large-Scale Canisters for Used Nuclear Fuel Storage Using Optimal Number of Acoustic Emission Sensors”:

Please note that, as the author of this Elsevier article, you retain the right to include it in a thesis or dissertation, provided it is not published commercially. Permission is not required, but please ensure that you reference the journal as the original source.

The paper entitled “Evaluation of ASR in Concrete Using Acoustic Emission and Deep Learning”:

Please note that, as the author of this Elsevier article, you retain the right to include it in a thesis or dissertation, provided it is not published commercially. Permission is not required, but please ensure that you reference the journal as the original source.